Nature and Strength of Intrinsic Cation-Anion Interactions of 1-Alkyl-3-Methylimidazolium Hexafluorophosphate Clusters

H. A. Roy and M. T. Rodgers*

Department of Chemistry, Wayne State University, Detroit, MI, 48202, USA

ABSTRACT:

Imidazolium-based cations and the hexafluorophosphate anion are among the most commonly used ionic liquids (ILs). Yet, the nature and strength of the intrinsic cation-anion interactions, and how they influence the macroscopic properties of these ILs are still not well understood. Threshold collision-induced dissociation is utilized to determine the bond dissociation energies (BDEs) of the 2:1 clusters of 1-alkyl-3-methylimidazolium cations and the hexafluorophosphate anion, $[2C_nmim{:}PF_6]^+$. The cation, $[C_nmim]^+$, is varied across the series, 1-ethyl-3-methylimidazolium $[C_2mim]^+$, 1-butyl-3-methylimidazolium $[C_4mim]^+$, 1-hexyl-3-methylimidazolium $[C_6mim]^+$, 1-octyl-3-methylimidazolium $[C_8mim]^+$, to examine the structural and energetic effects of the size of the 1-alkyl substituent of the cation on the binding to $[PF_6]^-$. Complementary electronic structure methods are employed for the $[C_nmim]^+$ cations, $(C_nmim{:}PF_6)$ ion pairs, and $[2C_nmim{:}PF_6]^+$ clusters to elucidate details of the cation-anion interactions and their impact on structure and energetics. Multiple levels of theory are benchmarked with the measured BDEs including B3LYP, B3LYP-GD3BJ, and M06-2X each with the 6-311+G(d,p) basis set for geometry optimizations and frequency analyses and the 6-311+G(2d,2p) basis set for energetic determinations. The modest structural variation among the $[C_nmim]^+$ cations produces only minor structural changes and variation in the measured BDEs of the $[2C_nmim{:}PF_6]^+$ clusters. Present results are compared to those previously reported for the analogous 1-alkyl-3-methylimidazolium tetrafluoroborate IL clusters to compare the effects of these anions on the nature and strength of the intrinsic binding interactions.

Corresponding author: M. T. Rodgers, mrodgers@chem.wayne.edu, Tel. (313) 577-2431

INTRODUCTION

Ionic liquids (ILs) are low temperature melting salts with melting points near or below 100°C. There is a wide diversity of cations and anions available that facilitate the formation of a diverse set of ionic liquids, yet the impacts of the specific cations and anions chosen on the macroscopic properties of ILs are still not well understood. The cations examined in this study are 1-alkyl-3-methylimidazolium cations, designated as $[C_nmim]^+$, where n = 2, 4, 6 and 8 and indicates the number of carbon atoms in the 1-alkyl substituent. A common anion present in ILs is hexafluorophosphate $[PF_6]^-$, the anion of focus in this work. The structures of the $[C_nmim]^+$ cations and $[PF_6]^-$ anion are shown in **Figure 1**.

Applications of ILs are diverse spanning energy storage,[1-3] electrochemistry,[4,5] separations,[6-10] and space propulsion,[11-13] among others. Understanding the intrinsic reactivity of ILs for use as propellants in electric space propulsion provides the motivation for this work. Electrospray ionization is an ionization technique originally developed by Yamashita and Fenn[14] where ion generation is facilitated by the application of a high voltage to a solution and the formation of a Taylor cone. Electrospray propulsion uses ion thrusters where the ion generation is similar to electrospray ionization, and the force produced by sample and ion ejection is used to propel spacecraft. IL thrusters can be operated in a single polarity[15] or bipolar mode.[16] Ionic liquids are advantagous as electrospray propellants due to their facile ion formation resulting from their inherently charged nature, low vapor pressures which reduces fuel loss, simplistic propulsion mechanism, and highly efficient nature of electric propulsion. Imidazolium-based IL propellants have been tested for use in outer space with the recent testing of 1-ethyl-3-methylimidazolium bis(trifluoromethylsulfonyl)imide on the ESA's LISA Pathfinder mission.[15,16]

Previous fundamental studies have investigated the structure of ILs and their clusters in both the condensed and gas phases using a variety of techniques. Computational chemistry and spectroscopy measurements have probed the structures of C_nmim-BF_4 and C_nmim-PF_6 ILs where n = 2–4.[17-31] In particular, B3LYP/6-311+G(2d,p) calculations were able to reproduce the Raman

and infrared spectra for the ($C_n$mim:PF_6) ion pairs with high fidelity for n = 2–4.[25] The gas-phase structrues suggest the presence of hydrogen bonding in the ion pairs calcuated at both the HF and B3LYP levels using the 6-311+G(2d,p) basis set. Noncovalent interactions/hydrogen bonding interactions are indicated between the C1′, C2, and C1″ hydrogen atoms of the $[C_n mim]^+$ cation and three of the F atoms of the $[PF_6]^-$ anion. Also reported are C2′ hydrogen F atom distances suggesting noncovalent interactions with the 1-alkyl substituent and the $[PF_6]^-$ anion. Kamalakannan et al. report ($C_n$mim:PF_6) ion pair structures and ion pairing energies for n = 2, 4, 6, and 8 in a theoretical study of ionic liquids binding to Au(111) surfaces.[30] Thomas et al. investigated the impact of dispersion correction in the incorporation of hydrophobic and hydrophilic ILs into zeolitic imidazolate framework-8 (ZIF-8) nanostructures using DFT approaches and IR spectroscopy. The structure of C_4mim-BF_4, C_4mim-PF_6, and other ILs were investigated in these ZIF-8 frameworks.[31] Hunt et al. characterized hydrogen bonding in a review article for a variety of IL systems and reported favorable cation-anion binding interactions to imidazolium cations. Using C_4mim-Cl as a prototypical imidazolium-based IL, they characterized cation-anion binding as front butyl, front methyl, alkyl methyl, side methyl, back, side butyl, and alkyl methyl binding.[32] X-ray crystallography has also been used to characterize $C_n$mim-PF_6 crystal structures.[33-36] Not suprisingly, the reported packing in the crystal structures differs from the predicted gas-phase structures. Fuller et al. show the molecular structure of the (C_2mim:PF_6) ion pair in the crystal and the packing observed.[33] In the crystal structures the $[PF_6]^-$ anion binds to multiple binding sites around the $[C_n mim]^+$ cations, including front, front alkyl, front methyl, back, front alkyl, and front methyl binding. These findings appear consistent with other reported crystal structures.[33-36]

Energy-resolved collision-induced dissociation (ER-CID) experiments have been performed to elucidate the gas-phase energetics and dissociation mechanisms of aprotic and protic ionic liquids for applications in space propulsion[37-39] and to elucidate relative affinities of various cations and anions that comprise common ILs.[40-45] MS utilizing variable energy CID is an ideal approach for revealing energetic trends. Bini et al. exmined the competitive dissociation

of mixed clusters and reported an intrinsic "interaction" scale for 11 different cations to $[Br]^-$ including the four 1-alkyl-3-methyimidazolium cations of interest here and found that the binding affinities follow the order: $[C_2mim]^+ > [C_4mim]^+ > [C_6mim]^+ > [C_8mim]^+$.[40] Bini et al. also reported an intrinsic "interaction" scale for a variety of anions and found that $[BF_4]^-$ binds more strongly than $[PF_6]^-$ to the imidazolium cations.[40] Gozzo et al. reported observing the $[5C_4mim{:}4PF_6]^+$ cluster as a magic number and a relative order of intrinsic binding to $[C_4mim]^+$ following $[CF_3CO_2]^- > [BF_4]^- > [PF_6]^- > [InCl_4]^- > [BPh_4]^-$.[41] Fernandes et al.[45,46] also used the variable-energy CID behavior approach to examine the intrinsic binding of the $[C_nmim]^+$ cations in $[2C_nmim{:}X]^+$ clusters where $[X]^-$ = $[Cl]^-$, $[BF_4]^-$, and bis(trifluoromethyl)sulfonylimide $[Tf_2N]^-$. Based on the relative center-of-mass collision energies at 50% dissociation ($E_{cm,1/2}$), the relative order of binding follows the order: $[C_8mim]^+ < [C_6mim]^+ < [C_4mim]^+ < [C_2mim]^+$ for both $[Cl]^-$ and $[Tf_2N]^-$; the same order excluding the $[C_6mim]^+$ cation, which was not included in that work, was also found for $[BF_4]^-$. Fernandes et al. also reported theoretical ($C_4mim{:}X$) ion paring energies, $[2C_4mim{:}X]^+$ BDEs, and $[C_4mim{:}2X]^-$ BDEs for X = $[Cl]^-$, $[BF_4]^-$, $[PF_6]^-$, trifluoromethanesulfonate $[Tf]^-$, and $[Tf_2N]^-$. They found a strong correlation between the anionic radius and the predicted interaction energies and measured $E_{cm,1/2}$ in these clusters.[46] Using Cooks' kinetic method, Vitorino et al.[42] also confirmed the relative order of binding of the $[C_nmim]^+$ cations to $[Tf_2N]^-$ as $[C_6mim]^+ < [C_4mim]^+ < [C_2mim]^+$ consistent with that observed by Bini et al.[40] These works suggest that the overall relative order of binding of the $[C_nmim]^+$ cations to $[PF_6]^-$ follows the order: $[C_8mim]^+ < [C_6mim]^+ < [C_4mim]^+ < [C_2mim]^+$. However, because the competitive experiments did not comprehensively examine other mixed clusters, and the energy-resolved experiments did not incorporate internal energy and unimolecular dissociation rates into the comparisons of the experimental data, there is still some uncertainty in this conclusion. Further, none of these other works have provided absolute binding affinities or BDEs of the IL clusters under investigation.

Ion mobility experiments[47-49] have been used to probe IL clusters to elucidate dissociation dynamics, magic number clusters, and ion evaporation mechanisms. Ku and Fernández de la

Mora investigated the charge state distributions of a variety of imidazolium-based ILs in acetonitrile and attributed the smallest ions being formed by the ion evaporation mechanism and the larger IL clusters to be associated with Dole's charged residue mechanism.[49] This study was extended by Hogan and Fernández de la Mora to study ion evaporation kinetics of the $[C_2mim]^+$ based ILs from ionic liquid-acetonitrile nanodrops where solvation energies are inferred from radius and charge state data.[43] Follow-up studies of neutral evaporation kinetics of IL clusters by Hogan and Fernández de la Mora reported magic number clusters for the $C_5A_4^+$ clusters for three of the four ILs studied.[44]

In previous work, we examined the interactions of the $[C_nmim]^+$ cations with $[BF_4]^-$.[43,44] These studies determined absolute BDEs of the $[2C_nmim:BF_4]^+$ clusters where n = 2, 4, 6 and 8, and found that the variation in the BDEs was smaller than the uncertainties in the determinations, that is the BDEs are equal to within experimental error. Experiments to examine the competitive dissociation of mixed $[C_{n-2}mim:BF_4:C_nmim]^+$ clusters were essential and pursued to definitively establish the relative order of intrinsic binding. The competitive dissociation experiments also provided absolute BDEs for $[C_nmim]^+$ binding to $(C_{n-2}mim:BF_4)$ as well as $[C_{n-2}mim]^+$ binding to $(C_nmim:BF_4)$ to be determined. From these absolute BDE determinations, relative $(C_nmim:BF_4)$ and $(C_{n-2}mim:BF_4)$ ion pairing energies (IPEs) were also determined. Consistent with the findings of Bini et al. for $[Br]^-$ the relative order of binding to $[BF_4]^-$ follows the order $[C_2mim]^+ > [C_4mim]^+ > [C_6mim]^+ > [C_8mim]^+$, i.e., the strength of binding is inversely correlated, albeit rather weakly with the size of the cation.

In the present work, we expand our threshold collision-induced dissociation (TCID) studies to include the interactions of the $[C_nmim]^+$ cations with $[PF_6]^-$. The nature and strength of the intrinsic binding interactions in $[2C_nmim:PF_6]^+$ clusters is studied using guided ion beam tandem mass spectrometry (GIBMS) and computational approaches. Density functional theory (DFT) methods provide theoretical insight into the structures accessed in the experiments and provide theoretical estimates for the measured BDEs. The theoretical models employed in this work include B3LYP,[50,51] B3LYP-GD3BJ,[52] and M06-2X.[53] Comparisons between the theoretical

predictions and experimental measurements are used to evaluate the performance of the theoretical methods for describing the structures and energetics of binding in these IL clusters. Present results for the $[2C_nmim:PF_6]^+$ clusters are compared with those for the $[2C_nmim:BF_4]^+$ clusters to additionally examine the influence of the anion on the nature and the strength of binding.

EXPERIMENTAL AND COMPUTATIONAL METHODS

Sample Preparation. Materials were purchased from commercial vendors and used as received. 1-Ethyl-3-methylimidazolium hexafluorophosphate, C_2mim-PF_6, and 1-octyl-3-methylimidazolium bis(trifluoromethylsulfonyl)imide, C_8mim-TFSI, were purchased from Alfa Aesar (Haverhill, MA). 1-Butyl-3-methylimidazolium hexafluorophosphate, C_4mim-PF_6, and HPLC grade methanol were purchased from Fisher Scientific (Walthan, MA). 1-Hexyl-3-methylimidazolium bis(trifluoromethylsulfonyl)imide, C_6mim-TFSI, and HPLC grade water were purchased from Sigma Aldrich (St. Louis, MO). Solutions of the desired ILs were prepared via dilution of a pure IL or a mixture of two ILs, one containing the desired cation, and the other the anion. Stock solutions of the ILs were diluted to ~0.5 mM in 50/50 methanol/water for introduction to the GIBMS. Stock solutions of the C_2mim-PF_6 and C_4mim-PF_6 ILs were simply diluted to the working concentration to produce the $[2C_2mim:PF_6]^+$ and $[2C_4mim:PF_6]^+$ clusters, whereas 1:1 mixtures of the C_2mim-PF_6 and C_6mim-TFSI ILs and separately the C_4mim-PF_6 and C_8mim-TFSI ILs were diluted to the working concentration to generate the $[2C_6mim:PF_6]^+$ and $[2C_8mim:PF_6]^+$ clusters, respectively.

Experimental Procedures. All TCID experiments were performed on a custom-built GIBMS that has been described in detail previously.[54] A syringe pump operated at a flow rate of 1 μL/min was used to deliver the working solution of the IL to a custom-built electrospray ionization (ESI) source.[55,56] A 35 ga stainless steel ESI emitter was held at ~2 kV to facilitate Taylor cone formation and ion generation. Ions were sampled through a 0.012” entrance limiting orifice and interfaced to the first stage of the mass spectrometer through a heated capillary maintained at ~100°C. Ions were trapped radially in an rf ion funnel using an ~25 V_{pp}, 530 kHz

potential applied 180° out of phase to adjacent ring electrodes. An ~25 V_{DC} gradient was applied across the ion funnel to gently guide the ions into the mass spectrometer. Ions were thermalized in a hexapole ion guide operated at 1.6 MHz and 100 V_{pp} spanning a differentially pumped chamber where the ions underwent a sufficient number of collisions (> 10^4) to produce a room temperature internal energy distribution. Ions were extracted and focused from cylindrical to a ribbon-shaped geometry, the ideal beam shape for momentum analysis in a magnetic sector mass analyzer. The ions were accelerated and mass selected using a magnetic sector mass analyzer, reshaped from a ribbon to cylindrical geometry, and slowed to a nominal kinetic energy using an exponential retarder. An octopole ion guide that passes through a collision cell containing xenon, the neutral collision gas, traps ions radially using an rf frequency of 4.44 MHz and ~300 V_{pp} applied to alternate rods. The collision energy is determined by the difference between the DC offset applied to the octopole rods and the energy zero determined via a retarding analysis. Remaining precursor ions and the resulting product ions are extracted from the octopole using a series of DC lenses and focused into a quadrupole mass analyzer (Extrel, 880 kHz Tri-filter with ¾" rods) where mass analysis occurs. Ions were detected using a Daly detector and standard pulse counting electronics.

Theoretical Calculations. A combination of molecular mechanics procedures and quantum mechanics calculations were performed. Theoretical calculations were performed to provide insight into the structures and energetics of the ($C_n$mim:PF_6) ion pairs and $[2C_n\text{mim:}PF_6]^+$ clusters, whereas results for the $[C_n\text{mim}]^+$ were taken from our earlier work.[43,44] Candidate structure sampling was performed via a simulated annealing procedure[57] using HyperChem with the Amber 3 force field.[58] A single run of the simulated annealing procedure includes 300 cycles of heating (0.3 ps), molecular dynamics sampling (0.2 ps), and cooling (0.3 ps) at a step size of 0.5 fs. In each annealing cycle, the starting temperature of 0 K was ramped to the simulation temperature of 1000 K for sampling and then cooled back down to 0 K, the final temperature. The cation(s) and anion of the IL clusters were constrained to the coordinate origin to prevent ion dissociation during the timeframe of the simulation. The restraining force applied

(0.01 kcal $mol^{-1} \cdot Å^{-2}$) was empirically derived, and kept as small as possible while still providing reasonable sampling of conformational space. The energy provided during the simulated annealing process was sufficient to enable sampling of various 1-alkyl substituent conformations, enantiomeric structures, and various modes of binding between the cation(s) and anion. Candidate structures were sorted by their molecular mechanics energies where a combination of low-energy structures and higher-energy structures were sampled. Low-energy structures were sampled because they are most relevant to the optimal ion pairing interactions and the experiments performed here. Higher-energy alternative binding structures were examined to provide insight into additional binding interactions that may occur in larger clusters and the condensed phase. Multiple runs of the simulated annealing procedure were performed with a total of 40–150 candidate structures for each ($C_n$mim:PF_6) ion pair and $[2C_n\text{mim}:PF_6]^+$ cluster submitted for further refinement using quantum mechanics methods at the B3LYP/6-311+G(2d,2p) level of theory. The B3LYP structures were also optimized using the B3LYP-GD3BJ and M06-2X functionals to examine functional bias. Comparisons of the resulting ($C_n$mim:PF_6) and $[2C_n\text{mim}:PF_6]^+$ structures were performed for n = 2, 4, 6, and 8. Due to the random nature of the simulated annealing procedures, there is no guarantee that all important low-energy conformations will be identified without resorting to exhaustive measures. Therefore in cases where parallel stable conformations for each value of n were not found from the simulated annealing derived approach, additional structures were manually constructed and directly subjected to the quantum mechanical calculations to limit the number of cycles of simulated annealing needed to achieve consistency among results for all of the ($C_n$mim:PF_6) ion pairs and $[2C_n\text{mim}:PF_6]^+$ clusters.

Quantum mechanical calculations were performed using the Gaussian 09 software package.[59] Geometry optimizations and frequency analyses were performed using the B3LYP, B3LYP-GD3BJ, and M06-2X density functionals with the 6-311+G(d,p) basis set. Single point energy calculations were performed using a larger 6-311+G(2d,2p) basis set to describe the energetics more accurately. To facilitate smooth convergence and elimination of negative

frequencies, the opt=tight and integral=ultrafine keywords were used for all M06-2X calculations. The calculated B3LYP/6-311+G(d,p) frequencies are scaled by a factor of 0.9887[60] to account for anharmonicities not described by the harmonic vibrational analysis and approximations made in the electronic structure calculations. The B3LYP-GD3BJ and M06-2X calculated frequencies were left unscaled, as the unscaled frequencies show excellent agreement with the scaled B3LYP values.[43] Zero-point energy corrections (ZPE) were calculated and included for all structures and for all levels of theory examined here. Basis set superposition errors (BSSE)[61,62] were also computed and corrected for in the BDEs determined.

The isotropic molecular polarizabilities of the ($C_n$mim:PF_6) ion pairs were calculated at the PBE1PBE/6-311+G(2d,2p) level of theory for use in the thermochemical analysis of the experimental data. This level of theory was used because it has been shown to calculate accurate polarizabilities of polyatomic neutral molecules and ions.[63] However, polarizabilities can be extracted directly from the geometry optimizations and thus the B3LYP/6-311+G(d,p) polarizabilites of the ($C_n$mim:PF_6) ion pairs as well as values for all stable conformers of the $[C_n\text{mim}]^+$ cations, ($C_n$mim:PF_6) ion pairs, and $[2C_n\text{mim}:PF_6]^+$ clusters are also available for comparisons.

Electrostatic potential (ESP) maps were computed for the B3LYP and M06-2X optimized geometries of the ground conformers for the ($C_n$mim:PF_6) ion pairs and the $[2C_n\text{mim}:PF_6]^+$ clusters. The ESP maps are used to reveal favorable interaction sites and determine the impact of the cation-anion interactions on electric potential in the ion pairs and clusters. All ESP maps were generated using the B3LYP or M06-2X functional and the 6-311+G(2d,2p) basis set, and are displayed at an isosurface of 0.01 a.u. of the total SCF electron density. The Mülliken charges are labeled on the hydrogen atoms of the cations and the fluorine atoms of the anion to quantify changes in electron density. The color scale is indicated on the ESP maps and chosen such that the most electronegative regions appear red, whereas the most electropositive regions appear blue, and regions of intermediate potential appear yellow or green.

Noncovalent interactions (NCIs) are revealed and plotted using NCIPLOT[64,65] and visualized using Visual Molecular Dynamics (VMD) software.[66] The NCIPLOT procedure looks for peaks appearing in the reduced gradient at low densities corresponding to favorable and unfavorable interactions. The sign of the product of the second density Hessian eigenvalue and the density distinguishes between attractive and repulsive interactions, while the magnitude describes the strength of interaction. Strong interactions such as hydrogen-bonding interactions are plotted as blue surfaces, weak interactions such as dispersion occurring from London-type forces are plotted as green surfaces, and strong repulsive forces such as steric interactions are plotted as red surfaces.

Thermochemical Analysis. Precursor and product ion intensities are monitored as a function of the laboratory collision energy and pressure of the neutral collision gas, Xe. Ion intensities are converted to energy-dependent CID cross sections using Beer's law, $I = I_0 e^{-\sigma_{tot}\rho l}$, where I is the measured intensity of the precursor ion, I_0 is the measured total ion intensity (i.e., the sum of the precursor and product ion intensities), σ_{tot} is the total CID cross section, ρ is the Xe collision gas density, and l is the effective interaction path length. The absolute zero and ion kinetic energy distributions of the precursor $[2C_nmim{:}PF_6]^+$ clusters are determined by a retarding energy analysis as described previously.[67] The resulting precursor kinetic energy distribution is nearly Gaussian with a full width at half maximum (fwhm) of 0.3–0.4 eV for these experiments. Collision energies in the laboratory frame (E_{lab}) are converted to energies in the center of mass frame (E_{cm}) using the formula $E_{cm} = mE_{lab}/(m+M)$, where M and m are the masses of the $[2C_nmim{:}PF_6]^+$ cluster ion and neutral Xe reactants, respectively. Pressure-dependent studies were performed because the effects of multiple collisions can impact the shape of CID cross sections, and in particular, shift the apparent thresholds to lower collision energies.[68] Cross sections were measured at three nominal pressures of ~0.20, 0.10, and 0.05 mTorr, and pressure extrapolated to zero pressure, corresponding to rigorously single-collision conditions.

The procedures employed for fitting the pressure-extrapolated CID cross sections have been discussed in detail previously.[54,69,70] Thresholds for the CID cross sections are modeled using an empirical threshold law of the form shown in eq 1,

$$\sigma(E) = \sigma_0 \sum_i g_i (E + E_i - E_0)^n / E \quad (1)$$

where σ_0 is an energy-independent scaling factor, E is the relative translational energy of the $[2C_nmim:PF_6]^+$ IL cluster and Xe reactants, E_0 is the threshold for the reaction of the ground electronic and ro-vibrational state, and n is an adjustable parameter associated with the efficiency of kinetic-to-internal energy transfer in the $[2C_nmim:PF_6]^+$-Xe collisions.[71] The Beyer-Swinehart algorithm[72] is used to calculate the density of the ro-vibrational states. The relative populations g_i are calculated for a Maxwell-Boltzmann distribution at 298 K of the $[2C_nmim:PF_6]^+$ cluster, as thermalization to room temperature is assured given the gentle sampling into the rf ion funnel and thermalization of the ions in the hexapole ion guide.[55,56] Lifetime effects are included during modeling using Rice-Ramsperger-Kassel-Marcus (RRKM) theory to account for $[2C_nmim:PF_6]^+$ clusters that do not dissociate on the time scale of the experiments (~10^{-4} s). The use of RRKM theory requires the ro-vibrational frequencies that describe the energized molecules and the transition states (TSs) leading to dissociation. A loose phase space limit (PSL) TS model is used as this model has been shown to be the most accurate for describing noncovalently bound complexes.[73-78] In particular, excellent results were obtained using the PSL TS model for the analogous IL clusters involving $[BF_4]^-$.[43,44] The model is convoluted with the kinetic and interal energy distributions of the $[2C_nmim:PF_6]^+$ and Xe reactants and the values of σ_0, E_0 or E_0(PSL), and n are optimized via nonlinear least-squares regression.

To provide estimates for the errors in the experimental threshold determinations, variations among multiple data sets, scaling of the vibrational frequencies, the time assumed available for dissociation, and errors in the absolute energy scale are included. The predicted vibrational frequencies are scaled up and down by 10% to provide estimates for the uncertainties in the computed frequencies. To provide estimates for uncertainties associated with RRKM lifetime effects, the time assumed available for dissociation was increased and decreased by a

factor of 2. Errors in the absolute energy scale are ±0.05 eV in the laboratory frame as limited by the voltage output by the octopole dc power supply, corresponding to ~0.02 eV in the center-of-mass frame for the $[2C_nmim:PF_6]^+$ + Xe CID reactions investigated in this work.[67] Uncertainties in the magnitudes fo the CID cross sections have previously been estimated as ~±20 %, whereas uncertainties in the relative cross section magnitudes are much smaller, ~±5 %.[67]

RESULTS

Cross Sections for Collision-Induced Dissociation. Energy-dependent CID cross sections were measured for the $[2C_nmim:PF_6]^+$ clusters with Xe, where n = 2, 4, 6, and 8. The energy-dependent cross sections for the CID of the $[2C_2mim:PF_6]^+$ cluster at a Xe pressure of ~0.2 mTorr is shown in **Figure 2**. Parallel fragmentation behavior is observed for all four $[2C_nmim:PF_6]^+$ clusters as can be seen in **Figure S1** of the **Supporting Information**. The dominant fragmentation pathway involves loss of an intact neutral ($C_2mim:PF_6$) ion pair and detection of the $[C_2mim]^+$cation as shown in the generalized **reaction 2**.

$$[2C_nmim:PF_6]^+ + Xe \rightarrow [C_nmim]^+ + (C_nmim:PF_6) + Xe \quad (2)$$

Sequential fragmentation of the $[C_nmim]^+$ cations is observed at collision energies greater than ~5-6 eV (cm). For all four $[2C_nmim:PF_6]^+$ clusters, the major sequential pathway observed involves neutral loss of the 1-alkyl substituent and detection of the 1-methylimidazolium cation, $[C_4H_7N_2]^+$, as seen in **Figure 2** for the $[2C_2mim:PF_6]^+$ cluster. Additional sequential fragments involving cleavages along the 1-alkyl substituent are also observed for the larger cations (see **Figure S1**). All CID pathways observed for the $[2C_nmim:PF_6]^+$ clusters are summarized in **Table S1**. The fragmentation pathways of the $[C_nmim]^+$ cations are not of primary interest here and thus will not be discussed further.

Theoretical Results. Stable structures, energetics, and properties of the $[PF_6]^-$ anion, ($C_nmim:PF_6$) ion pairs and $[2C_nmim:PF_6]^+$ clusters were calculated as described in the **Theoretical Calculations** section. The structures and stabilities of the $[C_nmim]^+$ cations are

taken from our initial work.[42] The geometric parameters of $[PF_6]^-$ are summarized in **Table S2** and compared to previously published results for $[BF_4]^-$.[43,44] Geometric parameters of the ground conformers of the $[C_nmim]^+$ cations are taken from previous work and summarized in **Table S3**.[43,44] Geometric parameters of the ground conformers of the ($C_nmim:PF_6$) ion pairs and $[2C_nmim:PF_6]^+$ clusters are summarized in **Tables S4** and **S5**. The nomenclature used to differentiate the stable conformations of the $[C_nmim]^+$ cations, ($C_nmim:PF_6$) ion pairs, and $[2C_nmim:PF_6]^+$ clusters was adopted from our previous study.[43] This nomenclature was designed to describe the nature of the cation-anion binding interactions, and the conformations and relative orientations of the cations to facilitate recognition of structural elements. The nomenclature is described briefly in the main text and additional details are provided in **Figure S2.** The following discussion focuses primarily on the B3LYP and M06-2X results as B3LYP-GD3BJ findings are highly parallel to one or the other of the former theoretical methods.

$[C_nmim]^+$ Cations. The B3LYP and M06-2X ground conformers of the $[C_nmim]^+$ cations with plots of the noncovalent interactions superimposed on these structures are shown in **Figure 3**. The $[C_nmim]^+$ cations are denoted by the dihedral angles that describe the 1-alkyl substituent enclosed in square brackets and a + superscript to indicate that these conformers are cations, $[a1...an]^+$. The B3LYP ground conformers of the $[C_nmim]^+$ cations are predicted to be $[g^-t_{n-2}]^+$ and $[g_+t_{n-2}]^+$, where the ∠C2N1C1′C2′ torsion is gauche and the remaining torsions along the 1-alkyl substituent adopt anti-staggered geometries, minimizing steric strain along the alkyl chain. No stabilizing noncovalent interactions between the alkyl chain and the π-cloud of the imidazolium ring are present in the NCI maps of the B3LYP structures. In contrast, the optimized M06-2X cation structures favor $[g^-g_+t_{n-3}]^+$ and $[g_+g^-t_{n-3}]^+$ conformations. These M06-2X conformations are dispersion stabilized via the NCIs between the C2′H and C3′H atoms of the 1-alkyl substituent and the π-cloud of the imidazolium ring as visualized by the green regions of the NCI surfaces of the $[C_nmim]^+$, cations. Details regarding the geometric parameters of the B3LYP, B3LYP-GD3BJ, and M06-2X geometry-optimized structures of the ground conformers of the $[C_nmim]^+$ cations are summarized in **Table S3**. ESP maps were reported for the $[C_nmim]^+$

cations, finding the most favorable binding interaction sites with the hydrogens of the imidazolium ring.[43] The Mülliken charges for the imidazolium hydrogen atoms were conserved with variation of the 1-alkyl substituent with the C2 hydrogen atoms exhibiting the greatest Mülliken charges suggesting this as the most favorable interaction site for the $[C_n mim]^+$ cations.

$[PF_6]^-$ Anion. Geometric parameters of the B3LYP, B3LYP-GD3BJ, and M06-2X geometry optimized structures of the $[PF_6]^-$ anion are summarized in **Table S2**. Noncovalent interactions are revealed using NCI plots superimposed on the B3LYP and M06-2X optimized structures of the $[PF_6]^-$ anion in **Figure 3**. Only a single conformer was found for $[PF_6]^-$ exhibiting an ideal octahedral geometry with P–F bond lengths of 1.646 Å. The P–F bond lengths in the M06-2X structure are slightly shorter than those computed by B3LYP and B3LYP-GD3BJ. The lone pairs of electrons on the F atoms of the anion provide favorable sites for donation of electron density to the $[C_n mim]^+$ cations.

($C_n$mim:PF_6) Ion Pairs. The B3LYP and M06-2X ground conformers of the ($C_n$mim:PF_6) ion pairs with plots of the noncovalent interactions superimposed on these structures are shown in **Figure 4**. In all of the ground conformers, regardless of the theory employed, binding occurs via noncovalent interactions between the C1′, C2, and C1″ hydrogen atoms of the $[C_n mim]^+$ cation and two of the F atoms of the $[PF_6]^-$ anion. Additional stabilization is garnered through an anion-π interaction between a third F atom and the π-cloud of the imidazolium ring. As for the bare cations, the 1-alkyl substituent takes on an anti-staggered geometry in the B3LYP structures. These noncovalent interactions are easily seen in the NCI plots of **Figure 4** as the cation-anion interaction polarizes the electron density toward the interaction surfaces. Here again, the NCI surfaces of the B3LYP structures are less extensive than those determined using the highly parameterized M06-2X functional. The cation-anion distance does not vary appreciably with the cation across the ($C_n$mim:PF_6) ion pair series, but does depend on the theoretical model employed with B3LYP finding a larger separation than B3LYP-GD3BJ and M06-2X, consistent with the smaller relative sizes of the NCI surfaces found for B3LYP.

The intrinsic binding interactions of the ground conformers of the ($C_n$mim:PF_6) ion pairs are generally conserved across the cation series and the various levels of theory examined among the low-energy conformers found. However, other less favorable modes of binding were also found among the stable conformers. Therefore, the ($C_n$mim:PF_6) ion pairs are denoted by the mode of binding and the dihedral angles that describe the conformation of the 1-alkyl substituent enclosed in parentheses and with no charge to indicate that these systems are neutral ion pairs, (**b1BS**;a1...an). See **Figure S2** for the various binding site designations, which provide details of the location and orientation of the binding interactions.

The B3LYP and M06-2X ground conformers of the ($C_n$mim:PF_6) ion pairs all exhibit front-side binding (**F**), but several favorable orientations as described by the **b1** dihedral angle are found including $\mathbf{g}_+$, $\mathbf{g}_-$, and **c**. The 1-alkyl substituents adopt anti-staggered orientations in which the 1-alkyl substituent partially wraps around the anion to achieve additional stabilization. The B3LYP ground conformers are described as ($\mathbf{g}_+$**F**;g_-), ($\mathbf{g}_+$**F**;g_-t_2), (**g**_**F**;g_-t_4), and (**g**_**F**;g_-t_6), whereas the M06-2X ground conformers are described as (**g**_**F**;g_-), (**g**_**F**;g_-t_2), (**g**_**F**;g_-t_4), and (**g**_**F**;g_-t_6) for n = 2, 4, 6, and 8, respectively. Notably, B3LYP finds a larger number of very low-energy conformers for the ion pairs involving the smaller cations. The analogous (**g**_**F**;g_-) and (**g**_**F**;g_-t_2) conformers of the (C_2mim:PF_6) and (C_4mim:PF_6) ion pairs lie only 0.6 and 1.0 kJ/mol above the computed ground conformers (B3LYP), respectively. Geometric parameters of the B3LYP, B3LYP-GD3BJ, and M06-2X geometry-optimized structures of the ground conformers of the ($C_n$mim:PF_6) ion pairs are summarized in **Table S4**. Additional structural and energetic information for the ground and other stable low-energy conformations of the ($C_n$mim:PF_6) ion pairs computed can be found in **Figures S3-S6**. ESP maps for the ($C_n$mim:PF_6) ion pairs are compared in **Figure S7**. The very minor differences in the ESP maps across the ($C_n$mim:PF_6) ion pair series indicate that the intrinsic cation-anion binding interactions in these ion pairs are only weakly influenced by the length of the 1-alkyl chain.

$[2C_n$mim:$PF_6]^+$ Clusters. The B3LYP and M06-2X ground conformers of the $[2C_n$mim:$PF_6]^+$ clusters with plots of the noncovalent interactions superimposed on these

structures are shown in **Figure 5.** Binding in the ground conformers of the $[2C_nmim{:}PF_6]^+$ clusters also occurs via noncovalent interactions between the C1′, C2, and C1″ hydrogen atoms of each of the cations and two of the F atoms of the $[PF_6]^-$ anion, with additional stabilization gained through an anion-π interaction between a third F atom and the π-cloud of each of the imidazolium rings parallel to that observed in the ($C_nmim{:}PF_6$) ion pairs. The 1-alkyl substituents again take on anti-staggered geometries as favored by the $[C_nmim]^+$ cations.

The intrinsic binding interactions of the ground conformers of the $[2C_nmim{:}PF_6]^+$ are also conserved across the $[C_nmim]^+$ cation series and the various levels of theory examined. The $[2C_nmim{:}PF_6]^+$ clusters are denoted by their modes of binding and the 1-alkyl conformations of the cations, as detailed in **Figure S2**. Cations are named based on the dihedral angles that describe the conformations of the 1-alkyl substitutes parallel to the $[C_nmim]^+$ and ($C_nmim{:}PF_6$) designations. The binding site (**BS**) is designated as in the ($C_nmim{:}PF_6$) ion pairs with an additional dihedral angle **b2** that distinguishes the relative orientations of the 1-alkyl substituents of the cations, [a1…an;**b2b1BS1b1BS2**;a1..an]$^+$. The B3LYP ground conformers of the $[2C_nmim{:}PF_6]^+$ clusters are $[g_-;\mathbf{ccFcF};g_-]^+$, $[g_+t_2;\mathbf{ccFcF};g_+t_2]^+$, $[g_-t_4;\mathbf{g_+cFcF};g_+t_4]^+$, and $[g_-t_6;\mathbf{g_-cFcF};g_-t_6]^+$, whereas the M06-2X ground conformers are described as $[g_+;\mathbf{g_+g_+Fg_+F};c]^+$, $[g_-t_2;\mathbf{tg_-Fg_+F};g_-t_2]^+$, $[g_+t_4;\mathbf{g_+g_+Fg_+F};g_+t_4]^+$, and $[g_-t_6;\mathbf{g_-g_+Fg_-F};g_+t_6]^+$ for n = 2, 4, 6, and 8, respectively. Not surprisingly, binding is strongest when each $[C_nmim]^+$ cation binds to three different fluorine atoms of the $[PF_6]^-$ anion. In this case, the octahedral geometry of the $[PF_6]^-$ anion leads to cations binding to opposite faces of the octahedron described by the fluorine atoms, thereby minimizing cation-cation repulsion. No stable structures were found for the $[2C_nmim{:}PF_6]^+$ clusters in which both cations bind to the same F atom. The octahedral geometry of the anion results in stable conformers where the **b2** dihedral angle is cis, trans, and gauche. Geometric parameters of the B3LYP, B3LYP-GD3BJ, and M06-2X geometry-optimized structures of the ground conformers of $[2C_nmim{:}PF_6]^+$ clusters are summarized in **Table S5**. The structures and B3LYP, B3LYP-GD3BJ, and M06-2X relative stabilities of the ground and other stable low-energy conformers of the $[2C_nmim{:}PF_6]^+$ clusters are compared in **Figures S8-S11**.

ESP maps of the B3LYP and M06-2X ground conformers of the $[2C_nmim:PF_6]^+$ clusters are compared in **Figure S12**. The minor differences in the ESP maps across the $[2C_nmim:PF_6]^+$ cluster series indicate that the intrinsic cation-anion binding interactions in these clusters are only weakly influenced by the length of the 1-alkyl chain. The excess positive charge is delocalized along the entire surfaces of the $[C_nmim]^+$ cations and the electrostatic potentials of the imidazolium ring hydrogen atoms exceed those of the alkyl chain hydrogen atoms, with the C2 hydrogen atoms again exhibiting the greatest electrostatic potential. The C1′, C2, and C1″ hydrogen atoms of the imidazolium cation remain the most favorable sites for interaction with the $[PF_6]^-$ anion. The electrostatic potential computed using M06-2X exceeds that determined by B3LYP over the entire cation(s), whereas the electrostatic potential computed using M06-2X is less negative than that computed by B3LYP for all F atoms of the $[PF_6]^-$ anion in all four $[2C_nmim:PF_6]^+$ clusters. The minor changes in the ESP maps across this cluster series suggest that the intrinsic cation-anion binding interactions in the $[2C_nmim:PF_6]^+$ clusters likely should also be minimally affected by the length of the 1-alkyl chain.

Isotropic molecular polarizabilities computed for the $[C_nmim]^+$ cations, $(C_nmim:PF_6)$ ion pairs, and $[2C_nmim:PF_6]^+$ clusters increase linearly with the size of the 1-alkyl substituent as shown in **Figure S13**. The B3LYP/6-311+G(d,p) polarizabilities of the $[C_nmim]^+$ cations are 11.4, 15.2, 18.9, and 22.6 $Å^3$, increase on binding to $[PF_6]^-$ to 15.9, 19.6, 23.3, and 27.0 $Å^3$ for the $(C_nmim:PF_6)$ ion pairs, and further increase on binding of a second $[C_nmim]^+$ cation to 27.4, 34.8, 42.3, and 49.7 $Å^3$ for the $[2C_nmim:PF_6]^+$ clusters, for n = 2, 4, 6 and 8, respectively. Notably, the sum of the polarizabilities of the $[C_nmim]^+$ cations and $(C_nmim:PF_6)$ ion pairs is almost exactly equal to the polarizability computed for the $[2C_nmim:PF_6]^+$ clusters. The computed PBE1PBE/6-311+G(2d,2p) polarizabilities of the $(C_nmim:PF_6)$ ion pairs parallel those determined using B3LYP, but are predicted to be ~3% larger, and are computed as 16.4, 20.3, 24.0, and 27.8$Å^3$, respectively. As the differences in the B3LYP vs. PBE1PBE computed polarizabilities are quite small, and do not alter the CID thresholds determined, the extra

PBE1PBE computations appear unnecessary for accurate threshold determinations, consistent with our findings for the analogous $[2C_nmim:BF_4]^+$ clusters.[43]

Threshold Analysis of CID Cross Sections. The zero-pressure extrapolated cross section for the primary CID reaction of the $[2C_2mim:PF_6]^+$ cluster with Xe (eq 2) is shown in **Figure 6**. The other $[2C_nmim:PF_6]^+$ clusters exhibit parallel behavior and are compared in **Figure S14**. The CID cross sections were modeled using an empirical threshold law with a loose PSL TS model.[69] The PSL TS model has been shown to provide the most accurate correction of kinetic shifts observed for CID reactions of noncovalently bound complexes.[73,77,79-84] As can be seen in the figures, the CID data are well reproduced using the PSL TS model over energy ranges exceeding 4 eV and cross section magnitudes of a factor of at least 100 for all four $[2C_nmim:PF_6]^+$ clusters. Fitting results are summarized in **Table 1**. The threshold analyses were performed with the inclusion of RRKM lifetime analysis to properly account for the lifetime of the dissociating ions and thereby extract accurate threshold energies, denoted as E_0(PSL). Also reported is the entropy of activation, $\Delta S^{\ddagger}$, which is indicative of the looseness of the TS and the size and complexity of the system. Modest variation of $\Delta S^{\ddagger}$ across these systems as a function of size of the cluster are observed and vary from 16 to 25 J mol^{-1} K^{-1}. Threshold analyses were also performed excluding the RRKM lifetime analysis, E_0 and the difference between the threshold values, E_0 - E_0(PSL), are reported as kinetic shifts. The kinetic shifts are significant and increase with the size (or number of vibrational modes) of the cluster from 0.76 eV for the smallest cluster, $[2C_2mim:PF_6]^+$, to 1.69 eV for the largest cluster, $[2C_8mim:PF_6]^+$. The E_0(PSL) values determined via thermochemical analysis correspond to 0 K BDEs of the $[2C_nmim:PF_6]^+$ clusters. Temperature corrections using standard formulas (assuming harmonic oscillator and rigid rotor models) were applied to the 0 K BDEs to convert them to enthalpies and free energies of binding at 298 K. The molecular parameters used in the fitting procedures are provided as supplementary tables, the vibrational frequencies, and the average vibrational energies at 298 K are given in **Table S6**, whereas rotational constants are given in **Table S7**. **Table 2** lists 0 and 298 K enthalpy, free energy, and entropic corrections for the $[2C_nmim:PF_6]^+$ clusters experimentally determined.

Uncertainties in the enthalpic and entropic corrections are estimated by ±10% variation in the computed vibrational frequencies.

DISCUSSION

Influence of the $[C_nmim]^+$ Cation on the Measured BDEs. Energy-dependent CID cross sections for the $[2C_nmim{:}PF_6]^+$ clusters at a Xe pressure of ~0.2 mTorr are compared in **Figure S1**. Although the experiments are performed under nominally single collision conditions, even a small population of the ions undergoing more than one collision can alter the shape of the measured CID cross section, particularly in the threshold region. Pressure effects are eliminated by extrapolation to zero pressure of the Xe reactant. Normalized zero-pressure-extrapolated cross sections for CID of the $[2C_nmim{:}PF_6]^+$ clusters are compared in **Figure S15**. The apparent thresholds of the $[C_nmim]^+$ product cross sections exhibit a small, systematic shift to higher energies with increasing values of n. That is, the $[C_nmim]^+$ product apparent thresholds increase with the size of the cluster/cation and follow the order $[C_2mim]^+ < [C_4mim]^+ < [C_6mim]^+ < [C_8mim]^+$. Based simply on apparent CID cross section thresholds, one would surmise that the strength of cation binding increases with the size of the cluster/cation. However, the measured cross sections and their apparent thresholds are dependent on the strength of binding and the experimental conditions. All experiments are performed under roughly equivalent conditions such that two competing effects influence the observed cross sections, the internal energy of the $[2C_nmim{:}PF_6]^+$ cluster and its rate of unimolecular dissociation to the $[C_nmim]^+$ and $(C_nmim{:}PF_6)$ products. As internal energy increases with the size of the cluster, whereas the rate of unimolecular dissociation decreases with size, is not clear which of the effects should dominate. It would be presumptuous to assume that the apparent thresholds could be relied upon to provide a definitive order of binding without a detailed thermochemical analysis that includes corrections for these effects.

The internal energy distributions of the $[2C_nmim{:}PF_6]^+$ clusters as described by Maxwell-Boltzmann distributions at 300 K are compared in **Figure S16**. The average internal

energy of the $[2C_nmim:PF_6]^+$ clusters increases with size from 0.71 ± 0.05 eV to 0.87 ± 0.06 eV to 1.02 ± 0.07 eV and to 1.17 ± 0.08 eV for n = 2, 4, 6, and 8. Internal energy effects would therefore tend to lower the apparent CID thresholds by the internal energy available, which increases by ~0.15 eV between successive clusters. The RRKM rate constants as a function of energy for unimolecular dissociation of the $[2C_nmim:PF_6]^+$ clusters using a loose PSL TS are also compared in **Figure S16**. The dissociation rate decreases with increasing size of the cluster at all energies; the energy required to achieve a rate > 10^4 s^{-1} (i.e., the inverse of the approximate time available for dissociation) increases with cluster size from 1.96 eV to 2.18 eV to 2.47 eV to 2.90 eV for n = 2, 4, 6, and 8. Lifetime effects would therefore tend to increase the apparent thresholds by similar energies between successive clusters. With the inclusion of internal energy and RRKM effects using a loose PSL TS, the BDEs of the $[2C_nmim:PF_6]^+$ clusters to produce $[C_nmim]^+$ and $(C_nmim:PF_6)$ are determined as 113.0 ± 4.4, 112.3 ± 5.2, 110.6 ± 6.6, and 110.3 ± 5.0 kJ/mol for n = 2, 4, 6, and 8, respectively (**Table 3**). Thus, with proper thermochemical analysis including internal energy and RRKM effects, the strength of binding follows the order of $[C_8mim]^+ \leq [C_6mim]^+ \leq [C_4mim]^+ \leq [C_2mim]^+$, in direct opposition to the trend in the apparent thresholds. These results showcase the necessity for the use of careful thermodynamic modeling. Although accurate BDEs are determined, the precision of those determinations is insufficient to definitely establish the relative order of binding among the $[C_nmim]^+$ cations to $[PF_6]^-$. The variation in the measured BDEs across these systems is quite small, only 2.7 ± 6.6 kJ/mol, roughly half the average experimental uncertainty (AEU) in these determinations, 5.3 ± 0.9 kJ/mol.

Guidance with regard to the relative strength of binding in these systems may be taken from the work of Bini et al.[40] and Fernandes et al.[45,46] Bini et al., examined the competitive CID behavior of mixed clusters of various ILs.[40] Most relevant to the systems examined here are the 1-alkyl-3-methylimidazolium bromide, C_nmim-Br, ILs where the relative order of binding to $[Br]^-$ was determined as $[C_2mim]^+ > [C_4mim]^+ > [C_6mim]^+ > [C_8mim]^+$. Given the similarities and differences in the nature of the binding interactions in the C_nmim-Br vs. C_nmim-PF_6 ILs

however, the same relative ordering cannot be assumed. In particular, the larger size of the $[PF_6]^-$ anion likely enables the binding interactions to be further strengthened by interactions with the 1-alkyl chains in the clusters involving the larger cations such that the relative order of binding may change. Fernandes et al.[45,46] also used the variable-energy CID behavior approach to examine the intrinsic binding of the $[C_nmim]^+$ cations in $[2C_nmim:X]^+$ clusters where $[X]^-$ = $[Cl]^-$, $[BF_4]^-$ and $[Tf_2N]^-$. Based on the relative center-of-mass collision energies at 50% dissociation, the relative order of binding follows the trend: $[C_8mim]^+ < [C_6mim]^+ < [C_4mim]^+ < [C_2mim]^+$ for both $[Cl]^-$ and $[Tf_2N]^-$; the same order excluding the $[C_6mim]^+$ cation, which was not included in that work, was also found for $[BF_4]^-$. Fernandes et al. also reported theoretical $[2C_4mim:X]^+$ BDEs for X = $[Cl]^-$, $[BF_4]^-$, $[PF_6]^-$, $[Tf]^-$, and $[Tf_2N]^-$. The $[2C_4mim:X]^+$ BDEs follow the trend $[Cl]^- > [BF_4]^- > [PF_6]^- > [Tf]^- > [Tf_2N]^-$ exhibiting a high correlation with anionic radius to theoretical interaction energies and $E_{cm,1/2}$ in these clusters.[46] The ionic volumes computed by Kobrak follow the order $[Cl]^-$ (47 Å^3) < $[BF_4]^-$ (73 Å^3) < $[PF_6]^-$ (107 Å^3)< $[Tf]^-$ (129 Å^3) < $[Tf_2N]^-$ (230 Å^3).[85]

To establish a definitive order of binding, a follow-up study of the TCID behavior of mixed $[C_{n-2}mim:PF_6:C_nmim]^+$ clusters is being pursued. Importantly, the results of this follow up study will determine the absolute BDEs of these mixed clusters and the relative order of binding with significantly improved precision. Further, by combining the results of the present study with those from competitive measurements, the BDEs determined for the $[2C_nmim:PF_6]^+$ clusters can be more accurately and precisely determined.

$[2C_nmim:PF_6]^+$ BDES: Theory vs Experiment. The TCID measured BDEs of the $[2C_nmim:PF_6]^+$ clusters are compared to the BDEs predicted for these clusters using B3LYP, B3LYP-GD3BJ, and M06-2X approaches in **Table 3** and **Figure 7**. All three levels of theory explored here perform reasonably well, with B3LYP providing the best predictions of the experimental BDEs. Indeed the mean absolute deviation (MAD) between the B3LYP and TCID measured values is quite small, 1.6 ± 1.5 kJ/mol, less than one third as large as the average experimental uncertainty (AEU) in these values, 5.3 ± 0.9 kJ/mol. In contrast, the MAD for

M06-2X, 6.7 ± 4.3 kJ/mol, is more than four times greater than that for B3LYP and larger than the AEU. The MAD for B3LYP-GD3BJ is larger still at 10.4 ± 6.6 kJ/mol, twice the AEU. Notably as can be seen in **Figure 7**, all of the B3LYP predicted $[2C_nmim:PF_6]^+$ BDEs lie within experimental uncertainty of the measured values. Although the M06-2X predicted BDEs exhibit reasonable agreement with the experimental values, all exceed the measured values suggesting that the high degree of parameterization of M06-2X overestimates the dispersion stabilization in the $[2C_nmim:PF_6]^+$ clusters. The less satisfactory agreement between theory and experiment observed for B3LYP-GD3BJ, with predicted BDEs that all exceed the measured values suggest that the added empirical dispersion overestimates the strength of binding in the $[2C_nmim:PF_6]^+$ clusters, once again likely due to overstabilization of the dispersion interactions in these clusters. Combined, these results suggest that B3LYP provides the most reliable prediction of the $[2C_nmim:PF_6]^+$ BDEs.

Structures of $[PF_6]^-$ vs. $[BF_4]^-$. Only a single conformer was found for $[PF_6]^-$ and $[BF_4]^-$ exhibiting ideal octahedral and tetrahedral geometries, respectively. In addition to the octahedral vs. tetrahedral geometries, the P–F bonds are significantly longer than the B–F bonds by 0.218 to 0.229 Å, see **Table S2**. The B3LYP computed B–F bond lengths in $[BF_4]^-$ are 1.417 Å compared to 1.646 Å in $[PF_6]^-$, corresponding to a cis F–F distance of 2.327 Å and trans F–F distance of 3.291 Å in $[PF_6]^-$. The B–F and P–F bond lengths in the M06-2X structures are slightly shorter than those computed by B3LYP and B3LYP-GD3BJ. The lone pairs of electrons on the fluorine atoms provide favorable sites for donation of electron density to the $[C_nmim]^+$ cations. The predicted size of the anion increases from $[BF_4]^-$ to $[PF_6]^-$ consistent with the computed ionic volumes 73 $Å^3$ vs. 107 $Å^3$ respectively.[85] Hexafluorophosphate presents additional potential binding with six fluorine atoms compared to only four in tetrafluoroborate, such that the geometries in small clusters as well as packing in liquids must differ to some extent.

Structures of ($C_nmim:PF_6$) vs. ($C_nmim:BF_4$) Ion Pairs. The optimized structures predicted for the ($C_nmim:PF_6$) and ($C_nmim:BF_4$) ion pairs[43] are very similar. In all of the ion pairs, front binding of the imidazolium cation to the anion is preferred and binding occurs via

noncovalent interactions between the C1′, C2, and C1″ hydrogen atoms of the $[C_nmim]^+$ cation and two of the F atoms of the anion, while a third F atom interacts with the π-cloud of the imidazolium ring. Elongation of the cation-anion binding distance is observed for the larger $[PF_6]^-$ anion. The C2–B distances in ($C_nmim:BF_4$) ion pairs increase with the size of the cluster from 3.114 to 3.211 Å compared to the C2–P distances that vary from 3.568 to 3.584 Å in the ($C_nmim:PF_6$) ion pairs. However, this large increase in the C2–P vs. C2–B distances is somewhat misleading as the P–F bonds of $[PF_6]^-$ are markedly longer than the B–F bonds of $[BF_4]^-$, 1.646 vs. 1.417 Å, and the binding interactions occur between the C1′, C2, and C1″ hydrogen atoms of the cation and the F atoms of the anion. Although the spatial orientations of the F atoms differ, the average H–F distances between the C1′, C2, and C1″ hydrogen and fluorine atoms minimally increase from 2.261 Å in the ($C_nmim:BF_4$) ion pairs compared to 2.283 Å in ($C_nmim:PF_6$) ion pairs. The structures predicted for the ($C_nmim:BF_4$) and ($C_nmim:PF_6$) ion pairs are consistent with those previously reported for the ($C_nmim:PF_6$)[25,28-31] and ($C_nmim:BF_4$)[17-20,28,29,31,43] ion pairs. Computational work on the ($C_nmim:PF_6$) ion pairs by Kamalakann et al. is most consistent with the present findings having predicted (**g**$_+$**F**;g$_+$), (**g**$_+$**F**;g$_+$t$_2$), (**g**$_+$**F**;g$_+$t$_4$), and (**g**$_+$**F**;g$_+$t$_5$g$_+$) ground structures at the PBE+D3/6-311++G** level of theory.[30] Although quite similar, the ground conformers of the ($C_2mim:PF_6$) and ($C_4mim:PF_6$) ion pairs reported by Talaty et al., (**g**$_+$**F**;g$_+$) and (**g**$_+$**F**;g$_+$tg$_-$), are predicted to be 0.6 and 2.5 kJ/mol less stable that the (**g**$_+$**F**;g$_-$) and (**g**$_+$**F**;g$_-$t$_2$) ground conformers determined here.[25] The B3LYP/6-31+G* ($C_2mim:PF_6$) and ($C_4mim:PF_6$) ground conformers from Dong are (**g**$_+$**F**;g$_+$) and (**g**$_+$**F**;g$_+$t$_2$) are 0.6 and 0.9 kJ/mol less stable than the ground conformers determined using the larger 6-311+G(d,p) basis set.[29] The MP2/6-311G** computed ($C_4mim:PF_6$) ground conformer from Tsuzuki appears to be the (**cF**;g$_+$g$_-$t) conformer, which is 3.9 kJ/mol less stable than the ground conformer reported here.[28] The key binding interactions are conserved in all studies, whereas slight differences in the alkyl chain orientation in the computed ground conformers are likely associated with the use of slightly different basis sets and the floppiness of these systems.

Structures of $[2C_nmim:PF_6]^+$ vs $[2C_nmim:BF_4]^+$ Clusters. As found for the ion pairs, the optimized structures predicted for the $[2C_nmim:BF_4]^+$ and $[2C_nmim:PF_6]^+$ clusters are similar. The $[2C_nmim:BF_4]^+$ and $[2C_nmim:PF_6]^+$ clusters and their respective ion pairs have similar predicted structures with similar NCIs, resulting in similar determined BDEs. Both clusters favor binding to the front of the imidazolium ring and the preference for the 1-alkyl substituent to adopt an elongated conformation resulting in $[g_+t_{n-2}]^+$ and $[g_-t_{n-2}]^+$ conformers(B3LYP). Cation binding in the $[2C_nmim:BF_4]^+$ clusters was predicted to be nearly planar in their front binding interactions with two fluorine atoms of $[BF_4]^-$. In contrast, cation binding in $[2C_nmim:PF_6]^+$ occurs with three fluorine atoms of $[PF_6]^-$, a binding motif consistent with that found in the ($C_nmim:PF_6$) and ($C_nmim:BF_4$) ion pairs. Two fluorines bind to the front of the imidazolium ring and a third fluorine orients itself over the imidazolium ring to achieve additional π-stabilization. Another impact of the larger size of $[PF_6]^-$ and the additional hydrogen-bond acceptors it provides as compared to $[BF_4]^-$ is that the **b1** and **b2** dihedral angles that describe the relative orientations of the cation and anion and those of the 1-alkyl substituents differ markedly even though the H–F binding interactions are preserved. The most favorable relative orientations of the 1-alkyl substituents of the cations in $[2C_nmim:BF_4]^+$ are primarily $\mathbf{g}_+$ and $\mathbf{g}_-$ conformers, whereas the relative orientations of the 1-alkyl substituents of $[2C_nmim:PF_6]^+$ span all possible orientations (**c**, **t**, $\mathbf{g}_+$, and $\mathbf{g}_-$), which are attributed to the change from a tetrahedral geometry of the anion, which allows interactions with only two fluorine atoms to an octahedral geometry, which can accommodate three. As for the ion pairs, the cation-anion binding distance is larger for the $[2C_nmim:PF_6]^+$ clusters than the $[2C_nmim:BF_4]^+$ clusters seen both in the large differences in the C2–P vs. C2–B distances as well as the smaller differences in the more relevant H–F distances. The slight elongation of the cation-anion interaction lengths combined with the larger sizes and diffusivities of the $[2C_nmim:PF_6]^+$ clusters compared to those of the $[2C_nmim:BF_4]^+$ clusters results in only a very slight decrease (by ~6.2%) in the predicted strength of binding in the $[2C_nmim:PF_6]^+$ clusters vs. their $[2C_nmim:BF_4]^+$ cluster analogues.

CID Behavior of $[2C_nmim:PF_6]^+$ vs. $[2C_nmim:BF_4]^+$ Clusters. Energy-dependent CID cross sections for the $[2C_nmim:PF_6]^+$ clusters are compared to those of the analogous $[2C_nmim:BF_4]^+$ clusters in **Figure S17**. As can be seen in the figure, the CID cross sections exhibit a high degree of similarity in both the apparent thresholds and cross section magnitudes. However, the apparent thresholds for the $[2C_nmim:PF_6]^+$ clusters exhibit a very minor shift to lower apparent energies suggesting a slight decrease in cation binding strength for the $[2C_nmim:PF_6]^+$ clusters compared to the $[2C_nmim:BF_4]^+$ clusters. Consistent with the observed CID cross sections, the BDEs determined via thermochemical analysis exhibit only very minor variation across both the cation and anions series. The strength of cation binding in the $[2C_nmim:PF_6]^+$ clusters is on average slightly weaker (by ~6.2%) than that in the $[2C_nmim:BF_4]^+$ clusters.[43,44] The slightly weaker binding of $[C_nmim]^+$ to $(C_nmim:PF_6)$ than $(C_nmim:BF_4)$ is attributed to the larger size of the $[PF_6]^-$ anion, which increases diffusivity. Parallel trends in the relative order of cation binding are observed for both the $[2C_nmim:PF_6]^+$ and $[2C_nmim:BF_4]^+$ clusters, where the strongest binding occurs for the smallest cations. Thus overall, the more charge dense cations and anions produce the strongest binding.

CONCLUSIONS

Understanding the interplay between the intrinsic binding interactions and reactivity of ionic liquids aids in their development for specific applications such as space propellants. While the intrinsic binding interactions in ILs are in principle tunable through variation of the cations and anions of which it is comprised, the effects of the cation and anion selected are still largely understood on an empirical and macroscopic basis. Here TCID and theoretical approaches are synergistically employed to elucidate the nature of the intrinsic binding interactions in C_nmim-PF_6 ILs and specifically to characterize the stable structures and energetics of binding in the $(C_nmim:PF_6)$ ion pairs and $[2C_nmim:PF_6]^+$ clusters for n = 2, 4, 6, and 8. The apparent CID thresholds are observed to increase with increasing values of n, suggesting that the $[2C_8mim:PF_6]^+$ cluster binds the most strongly. However, the apparent CID thresholds may and

in this case do not accurately reflect the relative strength of binding among the $[2C_2mim:PF_6]^+$ clusters due to the opposing effects that the increasing internal energy and decreasing rate of unimolecular dissociation have on the observed CID cross sections with increasing size of the cluster. With the incorporation of internal energy considerations and lifetime effects using RRKM theory, the trend in the thresholds determined is essentially reversed, with the binding inversely correlated with the size of the cation.

Theoretical methods were employed for the $[C_nmim]^+$ cations,[43] ($C_nmim:PF_6$) ion pairs, and $[2C_nmim:PF_6]^+$ clusters. Comparison of theory and experiment suggests that the B3LYP results are the most reliable for the prediction of $[2C_nmim:PF_6]^+$ BDEs with the smallest MADs between experiment and theory. M06-2X performs reasonably well with the predicted $[2C_nmim:PF_6]^+$ BDEs within experimental error of the measured BDES. Poorer agreement between theory and experiment is found for B3LYP-GD3BJ. The theoretical results predict very similar structures with only minor variations as a function of the size of the cation and among the three functionals, leading to similar predicted energetics as a function of the cation. While similar, minor tunability as a function of cation is predicted, where a slight increase in the strength of binding predicted for the $[2C_nmim:PF_6]^+$ clusters involving the smallest cations. Binding in the $[2C_nmim:PF_6]^+$ clusters is predicted to be slightly weaker than that in the analogous $[2C_nmim:BF_4]^+$ clusters. Although accurate $[2C_nmim:PF_6]^+$ BDEs are determined here, the precision of these determinations is insufficient to definitely establish the relative order of binding among the $[C_nmim]^+$ cations to $[PF_6]^-$. To definitively establish a relative order of binding and to improve the precision in the $[2C_nmim:PF_6]^+$ BDEs determined, a follow-up study of the behavior of mixed $[C_{n-2}mim:PF_6:C_nmim]^+$ clusters is being pursued.

ASSOCIATED CONTENT

Supporting Information. Tables of CID fragments of the $[2C_nmim:PF_6]^+$ clusters, geometric parameters, vibrational frequencies, average vibrational energies, and rotational constants of the B3LYP/6-311+G(d,p), B3LYP-GD3BJ/6-311+G(d,p), and M06-2X/6-311+G(d,p)

ground conformers of the $[C_nmim]^+$ and $[PF_6]^-$ ions, $(C_nmim:PF_6)$ ion pairs, and $[2C_nmim:PF_6]^+$ clusters. Figures comparing CID cross sections for the $[2C_nmim:PF_6]^+$ clusters; description of the nomenclature used to differentiate various stable conformations of the $[C_nmim]^+$ cations, $(C_nmim:PF_6)$ ion pairs, and $[2C_nmim:PF_6]^+$ clusters; stable B3LYP/6-311+G(d,p), B3LYP-GD3BJ/6-311+G(d,p), and M06-2X/6-311+G(d,p) conformers of the $(C_nmim:PF_6)$ ion pairs and $[2C_nmim:PF_6]^+$ clusters with superimposed NCI surfaces and relative Gibbs energies at 298K; ESP maps of the B3LYP and M06-2X ground conformers of the $(C_nmim:PF_6)$ ion pairs and $[2C_nmim:PF_6]^+$ clusters; comparison of the computed isotropic molecular polarizabilities of the $[C_nmim]^+$ cations, $(C_nmim:PF_6)$ ion pairs, and $[2C_nmim:PF_6]^+$ cluster as a function of n; comparison of the zero-pressure-extrapolated CID cross sections for the $[2C_nmim:PF_6]^+$ clusters with fits to the data using eq 1 shown individually as well as normalized and overlaid; Maxwell-Boltzmann internal energy distributions and RRKM unimolecular dissociation rate constants as a function of energy for the $[2C_nmim:PF_6]^+$ clusters; comparison of the zero-pressure extrapolated CID cross sections of the $[2C_nmim:PF_6]^+$ vs. $[2C_nmim:BF_4]^+$ clusters.

AUTHOR INFORMATION

Notes. The authors declare no competing financial interest.

ACKNOWLEDGEMENTS

Financial support for this work was provided by the National Science Foundation, CHE-1709789. Computational resources were provided by Wayne State University C&IT. The authors acknowledge support from the Wayne State University Summer Dissertation Fellowship for H.A.R.

ORCID

Harrison A. Roy https://orcid.org/0000-0002-9128-5245
Mary T. Rodgers https://orcid.org/0000-0002-5614-0948

REFERENCES

1. M. Watanabe, M. L. Thomas, S. Zhang, K. Ueno, T. Yasuda and K. Dokko, *Chem. Rev.*, 2017, **117**, 7190-7239.
2. D. R. MacFarlane, N. Tachikawa, M. Forsyth, J. M. Pringle, P. C. Howlett, G. D. Elliott, J. H. Davis, M. Watanabe, P. Simon and C. A. Angell, *Energy Environ. Sci.*, 2014, **7**, 232-250.
3. H. Liu and H. Yu, *J. Mater. Sci. Technol.*, 2018, **35**, 674-686.
4. H. Liu, Y. Liu and J. Li, *Phys. Chem. Chem. Phys.*, 2010, **12**, 1685-1697.
5. D. R. MacFarlane, M. Forsyth, P. C. Howlett, J. M. Pringle, J. Sun, G. Annat, W. Neil and E. I. Izgorodina, *Accts. Chem. Res.*, 2007, **40**, 1165-1173.
6. P. Sun and D. W. Armstrong, *Anal. Chem. Acta*, 2010, **661**, 1-16.
7. L. Brown, M. J. Earle, M. A. Gîlea, N. V. Plechkova and K. R. Seddon, in *Ionic Liquids II*, Springer 2017, pp. 85-125.
8. B. Soares, H. Passos, C. S. Freire, J. A. Coutinho, A. J. Silvestre and M. G. Freire, *Green Chem.*, 2016, **18**, 4582-4604.
9. C. F. Poole and N. Lenca, *J. Chromatogr. A*, 2014, **1357**, 87-109.
10. G. A. Baker, S. N. Baker, S. Pandey and F. V. Bright, *Analyst*, 2005, **130**, 800-808.
11. B. Prince, B. Fritz and Y. Chiu, *Ionic Liquids: Science and Applications*, 2012, **1117**, 27-49.
12. B. R. Donius and J. L. Rovey, *J. Spacecr. Rockets*, 2011, **48**, 110-123.
13. S. P. Berg and J. L. Rovey, *J. Propul. Power*, 2013, **29**, 339-351.
14. M. Yamashita and J. B. Fenn, *J. Phys. Chem.*, 1984, **88**, 4451-4459.
15. N. Demmons, V. Hruby, D. Spence, T. Roy, E. Ehrbar, J. Zwahlen, R. Martin, J. Ziemer and T. Randolph, ST7-DRS Mission Colloid Thruster Development, 2008.
16. G. Anderson, J. Anderson, M. Anderson, G. Aveni, D. Bame, P. Barela, K. Blackman, A. Carmain, L. Chen and M. Cherng, *Phys. Rev. D*, 2018, **98**, 102005.
17. C. J. Johnson, J. A. Fournier, C. T. Wolke and M. A. Johnson, *J. Chem. Phys.*, 2013, **139**, 224305.
18. J. A. Fournier, C. T. Wolke, C. J. Johnson, A. B. McCoy and M. A. Johnson, *J. Chem. Phys.*, 2015, **142**, 064306.
19. N. E. Heimer, R. E. Del Sesto, Z. Meng, J. S. Wilkes and W. R. Carper, *J. Mol. Liq.*, 2006, **124**, 84-95.
20. R. Holomb, A. Martinelli, I. Albinsson, J.-C. Lassegues, P. Johansson and P. Jacobsson, *J. Raman Spectrosc.*, 2008, **39**, 793-805.
21. T. Yamada, Y. Tominari, S. Tanaka and M. Mizuno, *J. Phys. Chem. B*, 2015, **119**, 15696-15705.
22. R. Cooper, A. M. Zolot, J. A. Boatz, D. P. Sporleder and J. A. Stearns, *J. Phys. Chem. A*, 2013, **117**, 12419-12428.
23. R. S. Booth, C. J. Annesley, J. W. Young, K. M. Vogelhuber, J. A. Boatz and J. A. Stearns, *Phys. Chem. Chem. Phys.*, 2016, **18**, 17037-17043.
24. J. M. Voss, B. M. Marsh, J. Zhou and E. Garand, *Phys. Chem. Chem. Phys.*, 2016, **18**, 18905-18913.
25. E. R. Talaty, S. Raja, V. J. Storhaug, A. Dölle and W. R. Carper, *J. Phys. Chem. B*, 2004, **108**, 13177-13184.
26. S. A. Katsyuba, E. E. Zvereva, A. Vidiš and P. J. Dyson, *J. Phys. Chem. A*, 2007, **111**, 352-370.
27. Y. Umebayashi, T. Fujimori, T. Sukizaki, M. Asada, K. Fujii, R. Kanzaki and S.-i. Ishiguro, *J. Phys. Chem. A*, 2005, **109**, 8976-8982.
28. S. Tsuzuki, H. Tokuda and M. Mikami, *Phys. Chem. Chem. Phys.*, 2007, **9**, 4780-4784.
29. K. Dong, S. Zhang, D. Wang and X. Yao, *J. Phys. Chem. A*, 2006, **110**, 9775-9782.

30. S. Kamalakannan, M. Prakash, M. M. Al-Mogren, G. Chambaud and M. Hochlaf, *J. Phys. Chem. C*, 2019, **123**, 15087-15098.
31. A. Thomas, K. R. Maiyelvaganan, S. Kamalakannan and M. Prakash, *ACS Omega*, 2019, **4**, 22655-22666.
32. P. A. Hunt, C. R. Ashworth and R. P. Matthews, *Chem. Soc. Rev.*, 2015, **44**, 1257-1288.
33. J. Fuller, R. T. Carlin, H. C. De Long and D. Haworth, *J. Chem. Soc., Chem. Commun.*, 1994, 299-300.
34. T. Endo, H. Masu, K. Fujii, T. Morita, H. Seki, S. Sen and K. Nishikawa, *Cryst. Growth Des.*, 2013, **13**, 5383-5390.
35. A. R. Choudhury, N. Winterton, A. Steiner, A. I. Cooper and K. A. Johnson, *J. Am. Chem. Soc.*, 2005, **127**, 16792-16793.
36. S. M. Dibrov and J. K. Kochi, *Acta Crystallogr. C*, 2006, **62**, o19-o21.
37. A. L. Patrick, K. M. Vogelhuber, B. D. Prince and C. J. Annesley, *J. Phys. Chem. A*, 2018, **122**, 1960-1966.
38. M. De Silva, A. C. Brown and A. L. Patrick, *J. Mass Spectrom.*, 2020, **55**, e4518.
39. A. L. Patrick, *Rapid Commun. Mass Spectrom.*, 2020, **34**, e8587.
40. R. Bini, O. Bortolini, C. Chiappe, D. Pieraccini and T. Siciliano, *J. Phys. Chem. B*, 2007, **111**, 598-604.
41. F. C. Gozzo, L. S. Santos, R. Augusti, C. S. Consorti, J. Dupont and M. N. Eberlin, *Chem. Eur. J.*, 2004, **10**, 6187-6193.
42. J. Vitorino, J. P. Leal and M. E. Minas da Piedade, *ChemPhysChem*, 2015, **16**, 1969-1977.
43. H. A. Roy, L. A. Hamlow and M. T. Rodgers, *J. Phys. Chem. A*, 2020, **124**, 10181-10198.
44. H. A. Roy and M. T. Rodgers, *J. Phys. Chem. A*, 2020, **124**, 10199-10215.
45. A. M. Fernandes, J. A. Coutinho and I. M. Marrucho, *J. Mass Spectrom.*, 2009, **44**, 144-150.
46. A. M. Fernandes, M. A. Rocha, M. G. Freire, I. M. Marrucho, J. A. Coutinho and L. M. Santos, *J. Phys. Chem. B*, 2011, **115**, 4033-4041.
47. C. J. Hogan and J. Fernández de la Mora, *J. Am. Soc. Mass Spectrom.*, 2010, **21**, 1382-1386.
48. C. J. Hogan Jr. and J. Fernández de la Mora, *Phys. Chem. Chem. Phys.*, 2009, **11**, 8079-8090.
49. B. K. Ku and J. Fernández de la Mora, *J. Phys. Chem. B*, 2004, **108**, 14915-14923.
50. A. D. Becke, *J. Chem. Phys.*, 1993, **98**, 5648-5652.
51. C. Lee, W. Yang and R. G. Parr, *Phys. Rev. B*, 1988, **37**, 785-789.
52. S. Grimme, S. Ehrlich and L. Goerigk, *J. Comput. Chem.*, 2011, **32**, 1456-1465.
53. Y. Zhao and D. G. Truhlar, *Theor. Chem. Acc.*, 2008, **120**, 215-241.
54. M. T. Rodgers, *J. Phys. Chem. A*, 2001, **105**, 2374-2383.
55. L. A. Hamlow, Wayne State University Dissertations, 2019, 2322.
56. Y. Chen and M. T. Rodgers, *J. Am. Chem. Soc.*, 2012, **134**, 2313-2324.
57. D. Bertsimas and J. Tsitsiklis, *Stat. Sci.*, 1993, **8**, 10-15.
58. K. Wolinski, J. Hinton, D. Wishart, B. Sykes, F. Richards, A. Pastone, V. Saudek, P. Ellis, G. Maciel and J. McIver, Hypercube, Inc., Gainsville, FL, 2004.
59. M. J. Frisch, G. W. Trucks, H. B. Schlegel, G. E. Scuseria, M. A. Robb, J. R. Cheeseman, G. Scalmani, V. Barone, B. Mennucci and G. A. Petersson, et al., Gaussian, Inc., Wallingford, CT, revision C.01 edn., 2009.
60. J. P. Merrick, D. Moran and L. Radom, *J. Phys. Chem. A*, 2007, **111**, 11683–11700.
61. S. Simon, M. Duran and J. Dannenberg, *J. Chem. Phys.*, 1996, **105**, 11024-11031.
62. S. F. Boys and R. Bernardi, *Mol. Phys.*, 1970, **19**, 553-566.
63. S. M. Smith, A. N. Markevitch, D. A. Romanov, X. Li, R. J. Levis and H. B. Schlegel, *J. Phys. Chem. A*, 2000, **108**, 11063-11072.
64. J. Contreras-García, E. R. Johnson, S. Keinan, R. Chaudret, J.-P. Piquemal, D. N. Beratan and W. Yang, *J. Chem. Theory Comput.*, 2011, **7**, 625-632.

65. E. R. Johnson, S. Keinan, P. Mori-Sánchez, J. Contreras-García, A. J. Cohen and W. Yang, *J. Am. Chem. Soc.*, 2010, **132**, 6498-6506.
66. W. Humphrey, A. Dalke and K. Schulten, *J. Mol. Graph.*, 1996, **14**, 33-38.
67. K. M. Ervin and P. B. Armentrout, *J. Chem. Phys.*, 1985, **83**, 166-189.
68. N. F. Dalleska, K. Honma and P. B. Armentrout, *J. Am. Chem. Soc.*, 1993, **115**, 12125-12131.
69. M. T. Rodgers, K. M. Ervin and P. B. Armentrout, *J. Chem. Phys.*, 1997, **106**, 4499-4508.
70. M. T. Rodgers and P. B. Armentrout, *J. Chem. Phys.*, 1998, **109**, 1787-1800.
71. F. Muntean and P. B. Armentrout, *J. Chem. Phys.*, 2001, **115**, 1213-1228.
72. T. S. Beyer and D. F. Swinehart, *Commun. ACM*, 1973, **16**, 379.
73. N. S. Rannulu, R. Amunugama, Z. Yang and M. T. Rodgers, *J. Phys. Chem. A*, 2004, **108**, 6385-6396.
74. N. Rannulu and M. Rodgers, *J. Phys. Chem. A*, 2009, **113**, 4534-4548.
75. P. B. Armentrout, Y. Chen and M. T. Rodgers, *J. Phys. Chem. A*, 2012, **116**, 3989-3999.
76. P. B. Armentrout, B. Yang and M. T. Rodgers, *J. Phys. Chem. A*, 2013, **117**, 3771-3781.
77. C. Ruan, Z. Yang and M. Rodgers, *Phys. Chem. Chem. Phys.*, 2007, **9**, 5902-5918.
78. R. Amunugama and M. Rodgers, *Int. J. Mass Spectrom.*, 2003, **227**, 1-20.
79. N. S. Rannulu and M. T. Rodgers, *J. Phys. Chem. A*, 2007, **111**, 3465-3479.
80. N. Hallowita, D. R. Carl, P. B. Armentrout and M. T. Rodgers, *J. Phys. Chem. A*, 2008, **112**, 7996–8008.
81. C. Ruan and M. T. Rodgers, *J. Am. Chem. Soc.*, 2004, **126**, 14600-14610.
82. H. Huang and M. T. Rodgers, *J. Phys. Chem. A*, 2002, **106**, 4277-4289.
83. M. T. Rodgers and P. B. Armentrout, *Int. J. Mass Spectrom.*, 1999, **185/186/187**, 359-380.
84. C. Ruan, Z. Yang, N. Hallowita and M. T. Rodgers, *J. Phys. Chem. A*, 2005, **109**, 11539-11550.
85. M. N. Kobrak, *Green Chem.*, 2008, **10**, 80-86.

Table 1. Threshold Dissociation Energy at 0 K, Entropies of Activation at 1000 K, Fitting Parameters of Eq. 2 and Kinetic Shifts of $[2C_nmim{:}PF_6]^+$ Clusters.

System	E_0(PSL)[b] (eV)	$\Delta S^{\ddagger}$ (PSL)[b] (J mol^{-1} K^{-1})	σ[b]	n[b]	E_0[c] (eV)	Kinetic Shift (eV)
$[C_2mim]^+$	1.17 (0.05)	18 (4)	61.1 (2.6)	1.0 (0.1)	1.93 (0.06)	0.76
$[C_4mim]^+$	1.16 (0.05)	28 (4)	64.0 (1.3)	1.2 (0.1)	2.18 (0.07)	1.02
$[C_6mim]^+$	1.15 (0.07)	16 (4)	143.1 (1.6)	1.0 (0.1)	2.58 (0.08)	1.43
$[C_8mim]^+$	1.14 (0.05)	25 (4)	116.9 (13.8)	1.3 (0.1)	2.83 (0.12)	1.69

[a] Present results, uncertainties are listed in parentheses. [b] Average values for loose PSL TS. [c] No RRKM analysis.

Table 2. Enthalpies and Free Energies of Binding of $[2C_nmim{:}PF_6]^+$ Clusters at 0 and 298 K in kJ/mol.[a]

System	ΔH_0	ΔH_0[b]	$\Delta H_{298} - \Delta H_0$[b]	ΔH_{298}	ΔH_{298}[b]	$T\Delta S_{298}$[b]	ΔG_{298}	ΔG_{298}[b]
$[C_2mim]^+$	113.0 (4.4)	113.3	-3.6 (0.1)	109.4 (4.4)	109.7	32.9 (1.5)	76.5 (4.6)	76.9
$[C_4mim]^+$	112.3 (5.1)	112.6	-3.7 (0.1)	108.6 (5.2)	108.8	35.2 (1.5)	73.4 (5.4)	73.8
$[C_6mim]^+$	110.6 (6.6)	107.6	-3.7 (0.1)	106.9 (6.6)	103.9	32.1 (1.5)	74.8 (6.8)	72.0
$[C_8mim]^+$	110.3 (5.0)	107.6	-4.0 (0.1)	106.3 (5.0)	103.6	34.8 (1.5)	71.5 (5.2)	69.1

[a] Values are given in kJ/mol. Uncertainties are listed in parentheses. [b] Density functional theory calculations at the B3LYP/6-311+G(2d,2p)/B3LYP/6-311+G(d,p) level of theory including BSSE corrections and with frequencies scaled by 0.9887.

Table 3. Bond Dissociation Energies for $[2C_nmim{:}PF_6]^+$ Clusters at 0 K in kJ/mol.

System	TCID	B3LYP[b]		GD3BJ[c]		M06-2X[d]	
		D_0	$D_{0,\,BSSE}$[e]	D_0	$D_{0,\,BSSE}$[e]	D_0	$D_{0,\,BSSE}$[e]
$[C_2mim]^+$	113.0 (4.4)	119.2	113.3	134.1	126.4	134.5	124.4
$[C_4mim]^+$	112.3 (5.2)	119.0	112.6	130.8	122.5	126.4	116.8
$[C_6mim]^+$	110.6 (6.6)	113.3	107.6	120.0	111.9	130.9	119.6
$[C_8mim]^+$	110.3 (5.0)	113.3	107.6	138.3	127.0	121.9	112.1
AEU/MAD[f]	5.3 (0.9)[f]	4.7 (2.1)	1.6 (1.5)	19.3 (7.7)	10.4 (6.6)	16.9 (4.8)	6.7 (4.3)

[a]Present results. Uncertainties are listed in parentheses. [b]Calculated at the B3LYP/6-311+G(2d,2p) level of theory including ZPE corrections. [c]Calculated at the B3LYP-GD3BJ/6-311+G(2d,2p) level of theory. [d]Calculated at the M06-2X level of theory including ZPE corrections. [e]Also includes BSSE corrections. [f]Average experimental uncertainty (AEU) and mean absolute deviation (MAD) between the measured and calculated values.

Figure Captions

Figure 1. Chemical structures of 1-alkyl-3-methylimidazolium cations, $[C_nmim]^+$ for n = 2, 4, 6, and 8, and the $[PF_6]^-$ anion. The atom numbering of the cations is indicated.

Figure 2. Energy-dependent cross sections for the collision-induced dissociation of the $[2C_2mim{:}PF_6]^+$ cluster with Xe at a pressure of ~0.2 mTorr. Cross sections are reported as a function of the center-of-mass (lower *x*-axis) and laboratory frame (upper *x*-axis) collision energies.

Figure 3. B3LYP/6-311+G(d,p) and M06-2X/6-311+G(d,p) optimized geometries of the ground conformers of the $[C_nmim]^+$ cations, n = 2, 4, 6, and 8, and the $[PF_6]^-$ anion. Noncovalent interaction maps are superimposed on the optimized structures at an isosurface of 0.20 a.u. of the reduced electron density gradients determined using the 6-311+G(2d,2p) basis set.

Figure 4. B3LYP/6-311+G(d,p) and M06-2X/6-311+G(d,p) optimized geometries of the ground conformers of the ($C_nmim{:}PF_6$) ion pairs, for n = 2, 4, 6, and 8. Noncovalent interactions maps are superimposed on the optimized structures at an isosurface of 0.20 a.u. of the reduced electron density gradients determined using the 6-311+G(2d,2p) basis set.

Figure 5. B3LYP/6-311+G(d,p) and M06-2X/6-311+G(d,p) optimized geometries of the ground conformers of the $[2C_nmim{:}PF_6]^+$ clusters, for n = 2, 4, 6, and 8. Noncovalent interaction maps are superimposed on the optimized structures at an isosurface of 0.20 a.u. of the reduced electron density gradients determined using the 6-311+G(2d,2p) basis set.

Figure 6. Energy-dependent zero-pressure-extrapolated cross sections for the collision-induced dissociation of the $[2C_2mim{:}PF_6]^+$ cluster with Xe. The cross section is reported as a function of the center-of-mass (lower *x*-axis) and laboratory frame (upper *x*-axis) collision energies. The solid line represents the best fit to the experimental data convoluted with the neutral and ion kinetic energy distributions. The dashed line represents the model cross section in the absence of experimental kinetic energy broadening for reactants with a 0 K internal energy.

Figure 7. Comparison of B3LYP, B3LYP-GD3BJ, and M06-2X computed 0 K BDEs vs. measured threshold dissociation energies of the $[2C_nmim{:}PF_6]^+$ IL clusters for n = 2, 4, 6, and 8. The diagonal line indicates perfect agreement between the calculated and measured values. The mean absolute deviation (MAD) between the computed and measured values is given for each level of theory.

Figure 8. Comparison of the measured BDEs of the $[2C_nmim{:}PF_6]^+$ clusters to those of the $[2C_nmim{:}BF_4]^+$ clusters, for n = 2, 4, 6, and 8. The $[2C_nmim{:}PF_6]^+$ BDEs measured here are compared to evaluated $[2C_nmim{:}BF_4]^+$ BDEs based on combined direct and competitive CID experiments in part a, and to $[2C_nmim{:}BF_4]^+$ BDEs directly measured in part b. The B3LYP predicted BDEs are compared in part c. The solid lines indicate equal BDES for the $[2C_nmim{:}PF_6]^+$ and $[2C_nmim{:}BF_4]^+$ clusters. The dashed lines show linear regression fits to the data. Data for the $[2C_nmim{:}BF_4]^+$ clusters is taken from references 43 and 44.

Figure 1.

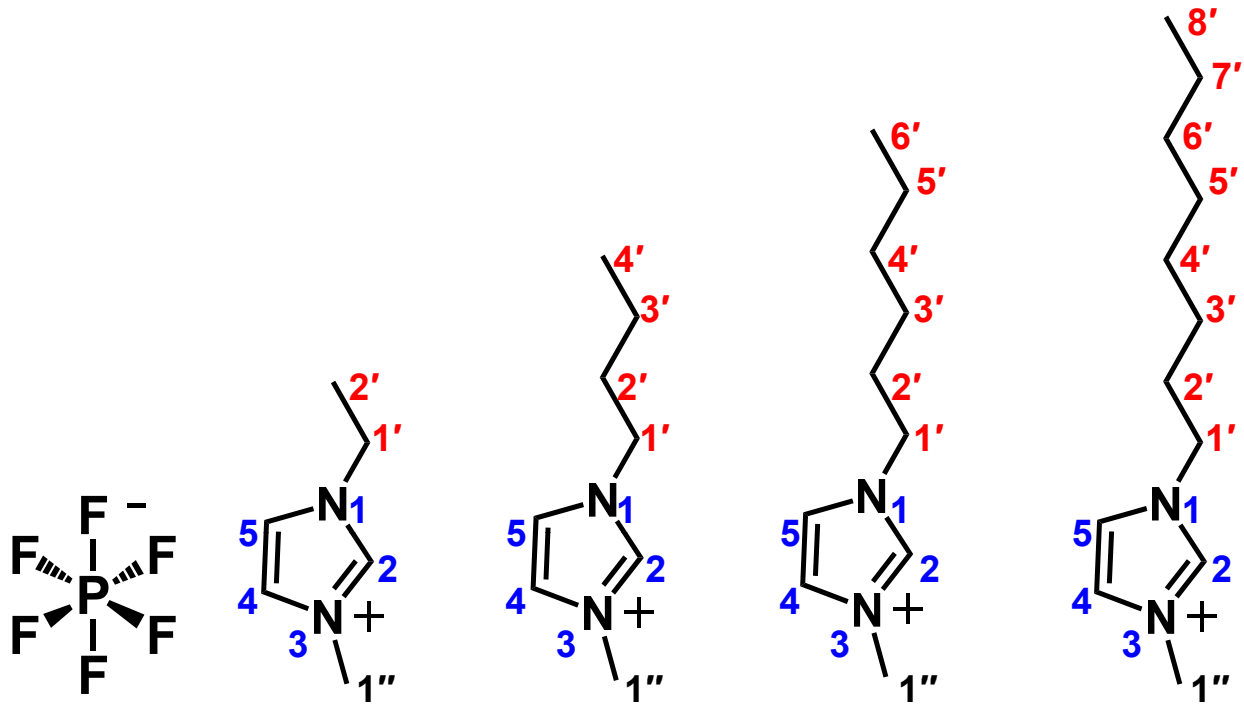

1-column figure, please reproduce at 50% of the current magnification

Figure 2.

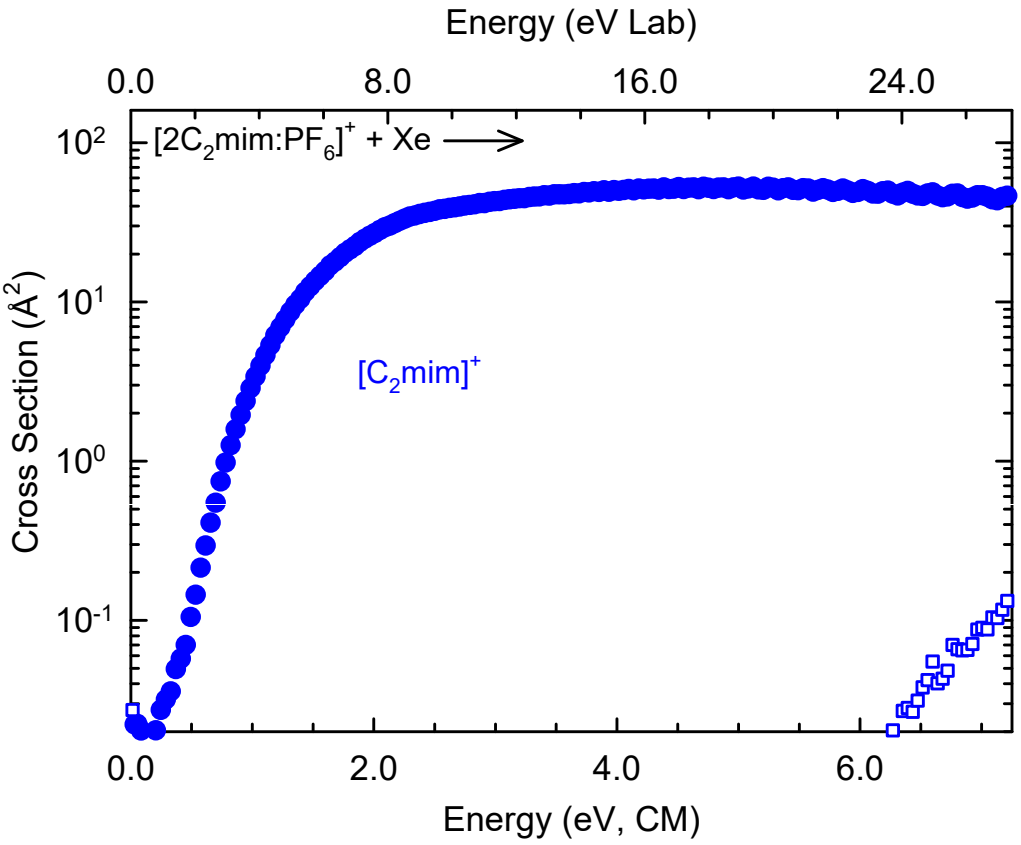

1-column figure, please reproduce at 50% of the current magnification

Figure 3.

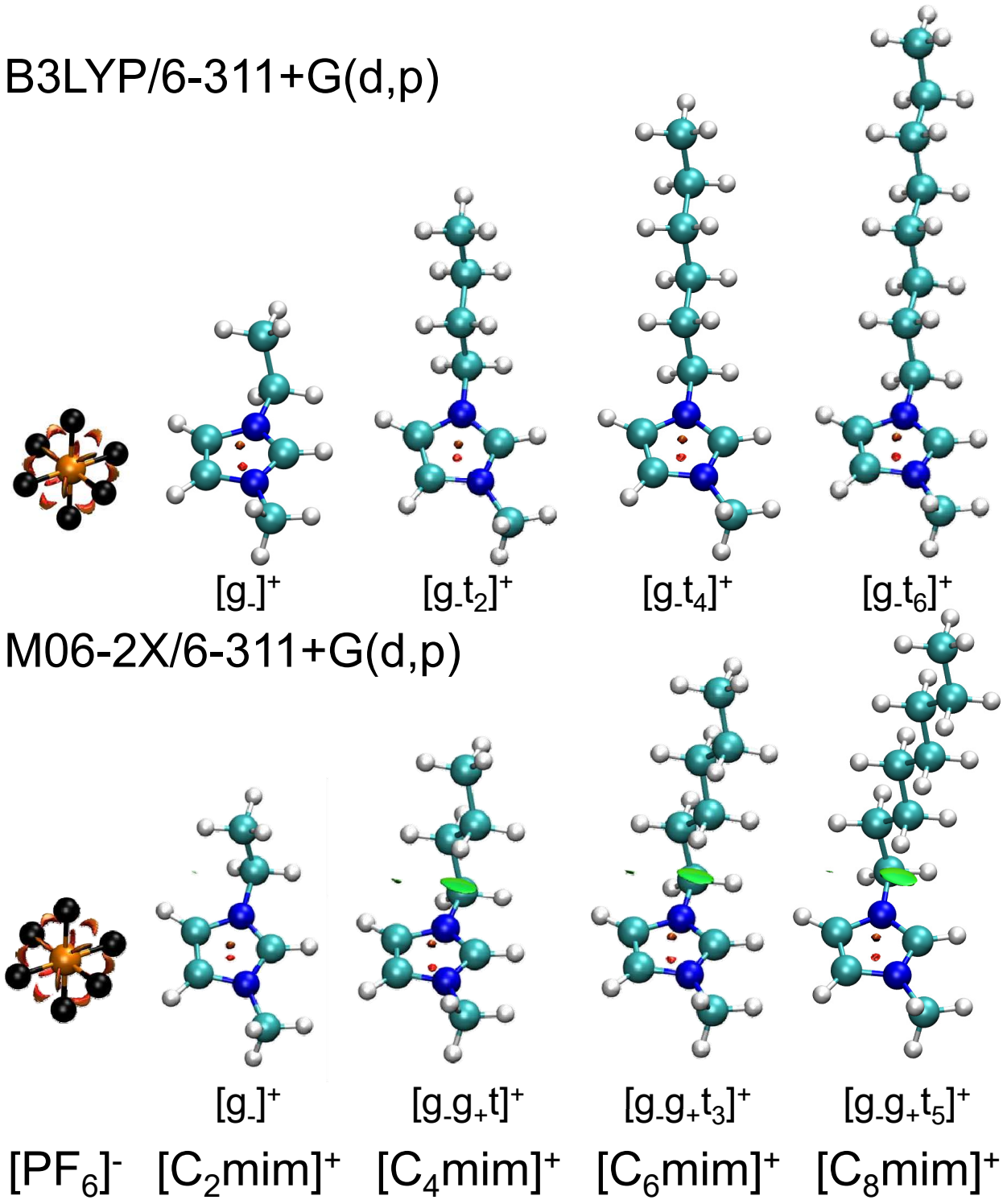

1-column figure, please reproduce at 50% of the current magnification

Figure 4.

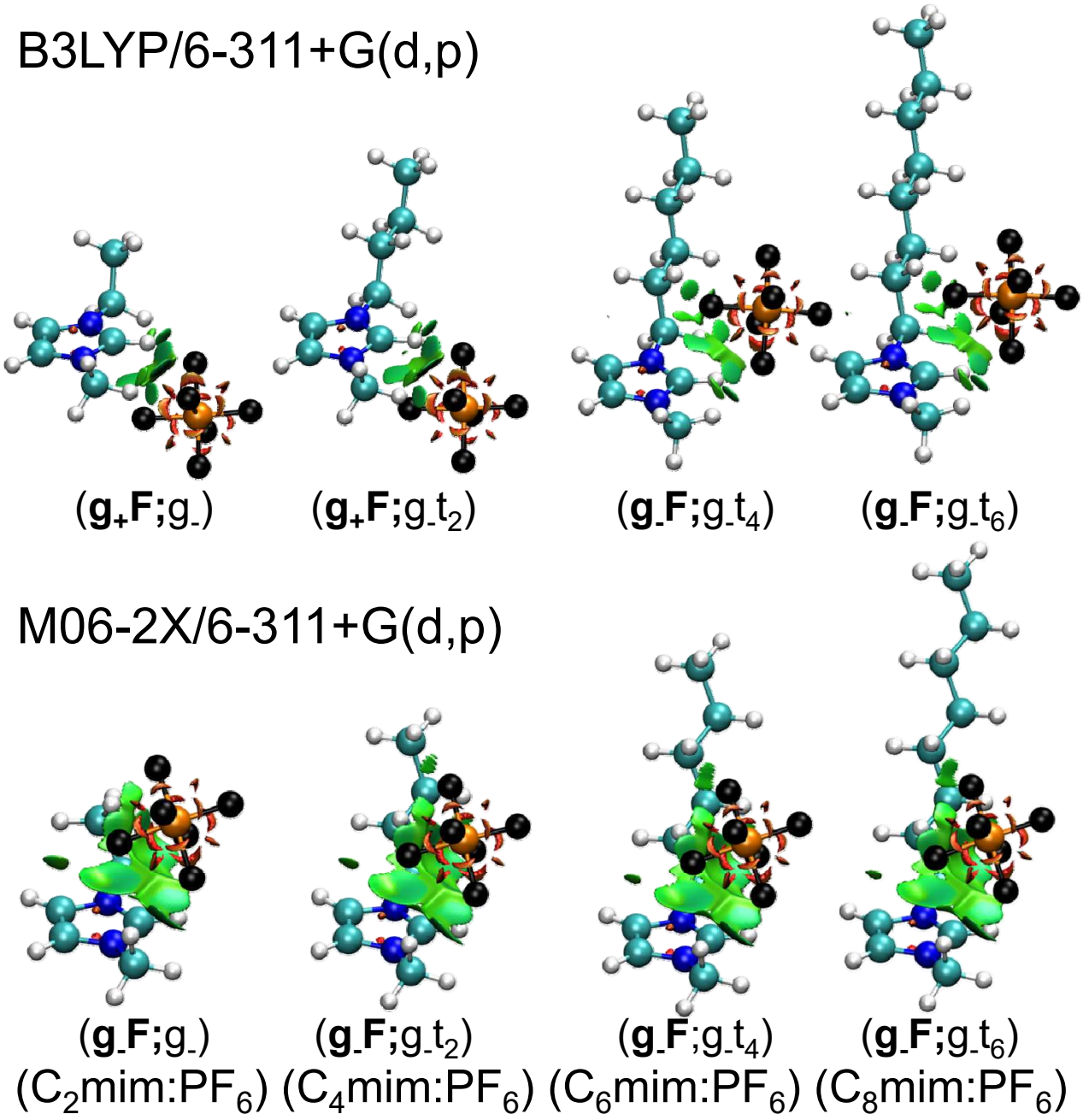

1-column figure, please reproduce at 50% of the current magnification

Figure 5.

B3LYP/6-311+G(d,p)

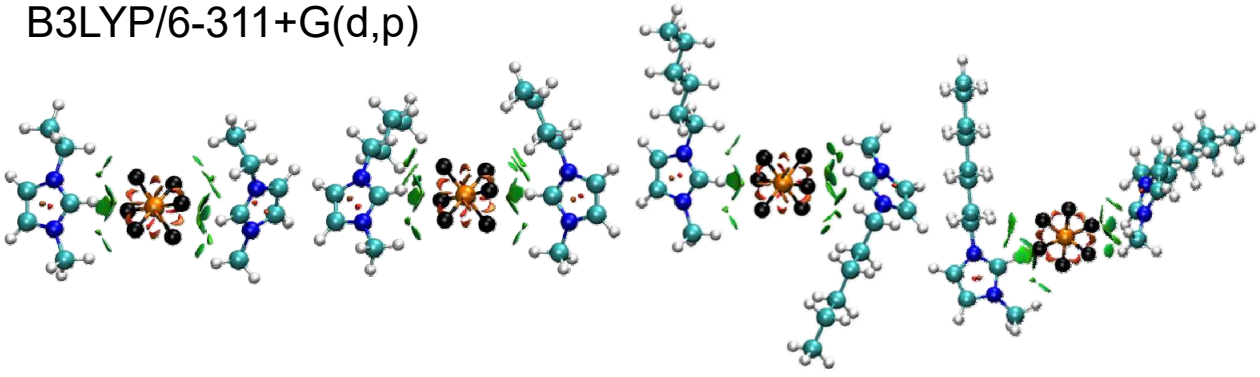

$[g_-;\mathbf{ccFcF};g_-]^+$ $[g_+t_2;\mathbf{ccFcF};g_+t_2]^+$ $[g_-t_4;\mathbf{g_+cFcF};g_+t_4]^+$ $[g_-t_6;\mathbf{g_-cFcF};g_-t_6]^+$

$[2C_2mim{:}PF_6]^+$ $[2C_4mim{:}PF_6]^+$ $[2C_6mim{:}PF_6]^+$ $[2C_8mim{:}PF_6]^+$

$[g_+;\mathbf{g_+g_+Fg_+F};c]^+$ $[g_-t_2;\mathbf{tg_-Fg_+F};g_-t_2]^+$ $[g_+t_4;\mathbf{g_+g_+Fg_+F};g_+t_4]^+$ $[g_-t_6;\mathbf{g_-g_+Fg_-F};g_+t_6]^+$

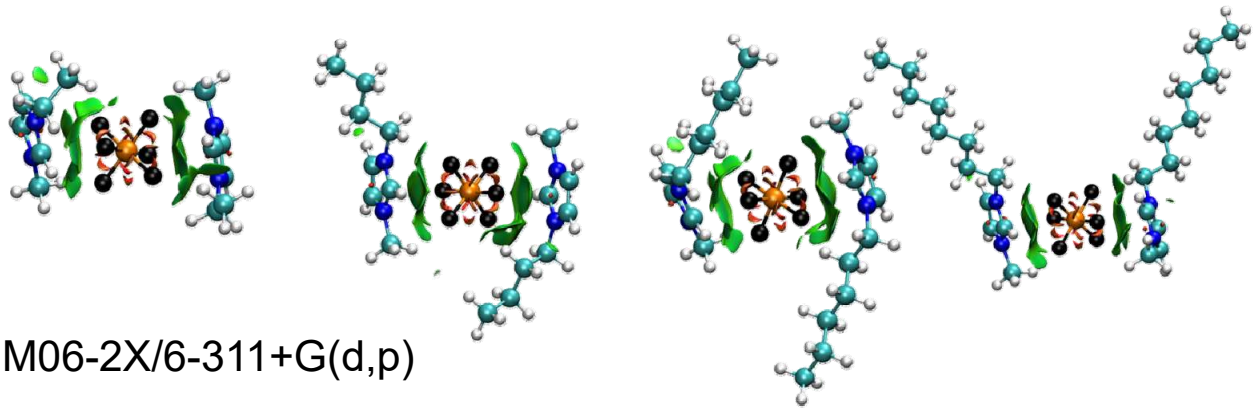

M06-2X/6-311+G(d,p)

2-column figure, please reproduce at current magnification

Figure 6.

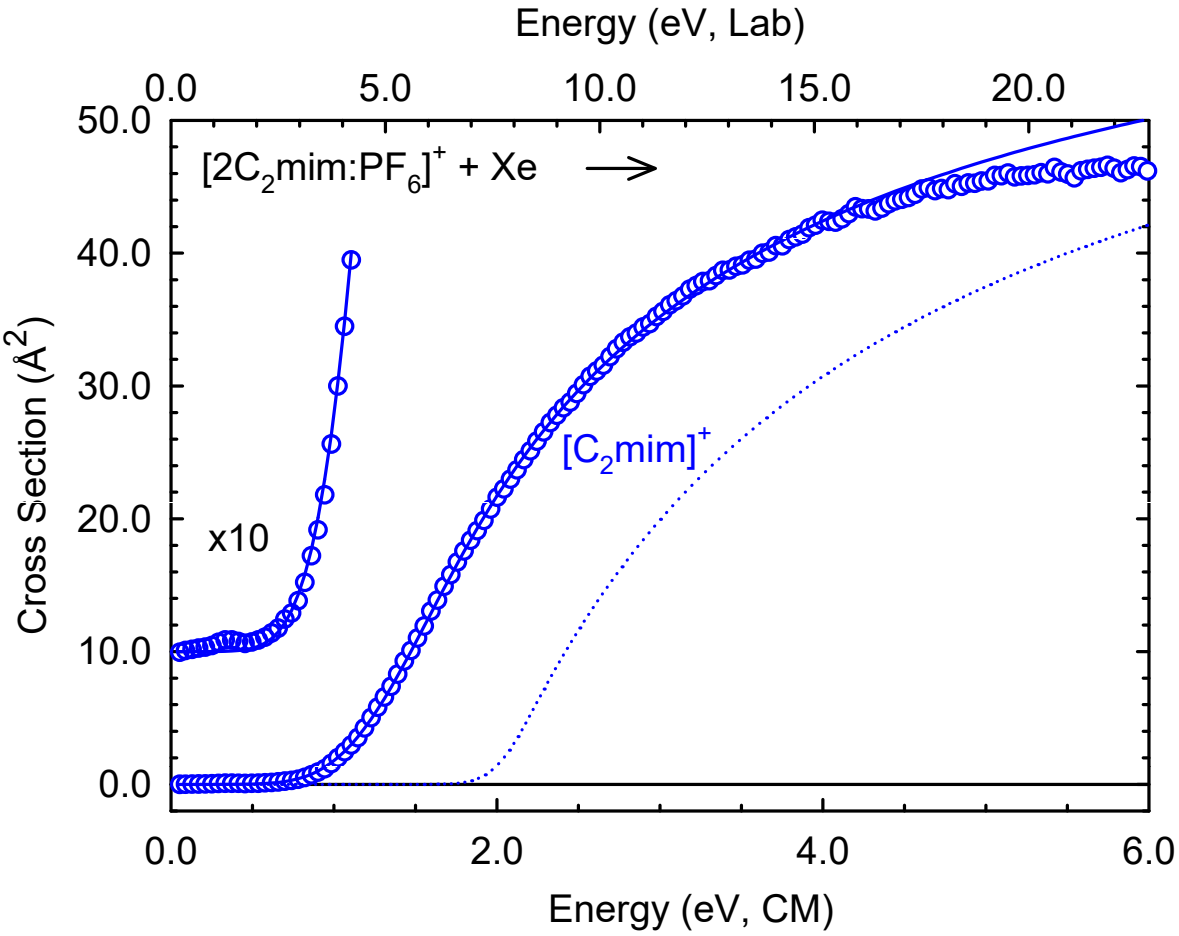

1-column figure, please reproduce at 50% of the current magnification

Figure 7.

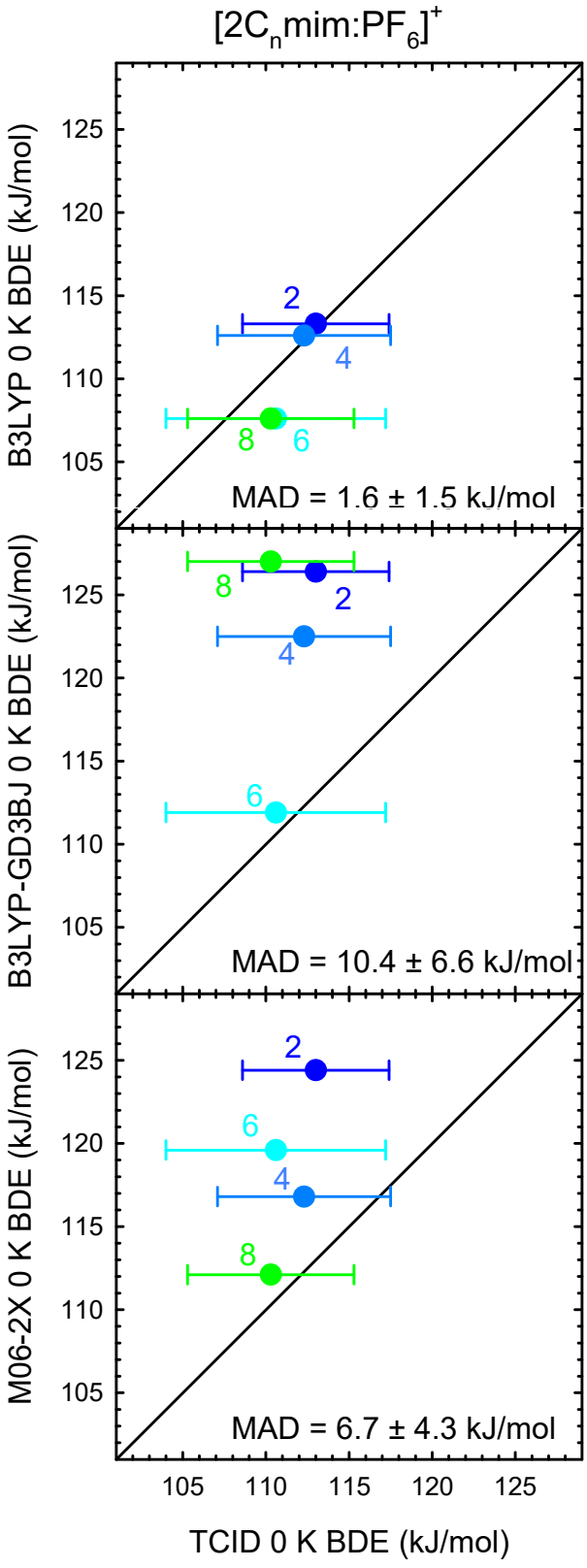

1-column figure, please reproduce at 70% of the current magnification

Figure 8.

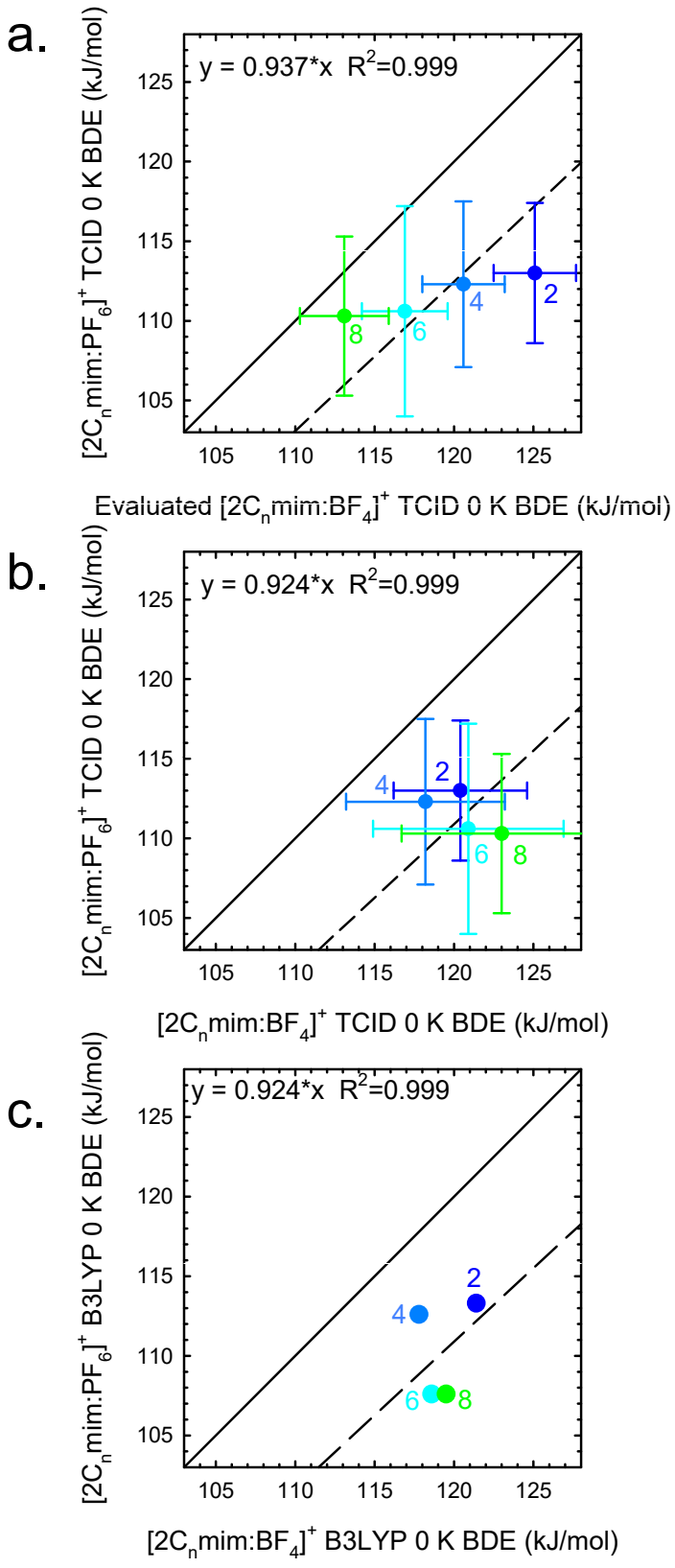

1-column figure, please reproduce at 70% of the current magnification

Supporting Information for…

Nature and the Strength of Intrinsic Cation-Anion Interactions of 1-Alkyl-3-Methylimidazolium Hexafluorophosphate Clusters

H. A. Roy and M. T. Rodgers*
Department of Chemistry, Wayne State University, Detroit, MI, 48202, USA

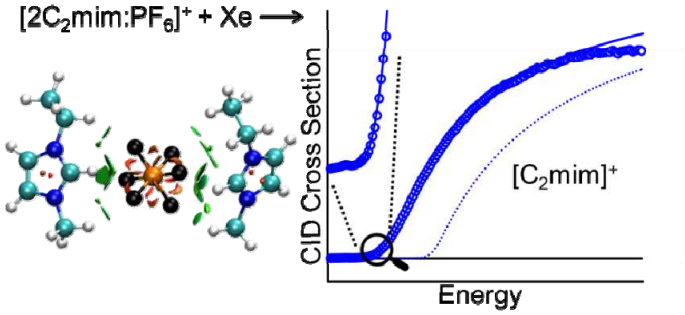

Table of Contents

Table S1. CID Fragments of the $[2C_nmim{:}PF_6]^+$ Cluster Ions

precursor ion	m/z (Da/*e*)	Symbol	1° fragment ion	2° fragment ions	neutral loss(es)
$[2C_2mim{:}PF_6]^+$	367				
	111	●	$[C_2mim]^+$		$(C_2mim{:}PF_6)$
	83	□		$[C_4H_7N_2]^+$	C_2H_4
$[2C_4mim{:}PF_6]^+$	423				
	139	●	$[C_4mim]^+$		$(C_4mim{:}PF_6)$
	83	□		$[C_4H_7N_2]^+$	C_4H_8
	57	△		$[C_4H_9]^+$	$C_4H_6N_2$
	43	○		$[C_3H_7]^+$	$C_5H_8N_2$
$[2C_6mim{:}PF_6]^+$	479				
	167	●	$[C_6mim]^+$		$(C_6mim{:}PF_6)$
	83	□		$[C_4H_7N_2]^+$	C_6H_{12}
	57	△		$[C_4H_9]^+$	$C_6H_{10}N_2$
	43	○		$[C_3H_7]^+$	$C_7H_{12}N_2$
$[2C_8mim{:}PF_6]^+$	535				
	195	●	$[C_8mim]^+$		$(C_8mim{:}PF_6)$
	83	□		$[C_4H_7N_2]^+$	C_8H_{16}
	71	▽		$[C_5H_{11}]^+$	$C_7H_{12}N_2$
	57	△		$[C_4H_9]^+$	$C_8H_{14}N_2$
	43	○		$[C_3H_7]^+$	$C_9H_{12}N_2$

[a] The elemental compositions of the $[C_nmim]^+$ cations are: $[C_2mim]^+ = [C_6H_{11}N_2]^+$, $[C_4mim]^+ = [C_8H_{15}N_2]^+$, $[C_6mim]^+ = [C_{10}H_{19}N_2]^+$, and $[C_8mim]^+ = [C_{12}H_{23}N_2]^+$.

Table S2. Geometric Parameters of B3LYP, B3LYP-GD3BJ, and M06-2X Optimized Geometries of the $[BF_4]^-$ and $[PF_6]^-$ Anions[a]

theory	$[BF_4]^-$			$[PF_6]^-$			
	B-F (Å)	∠FBF (°)	F-F (Å)	P-F (Å)	∠FPF (°)	cis F-F (Å)	trans F-F (Å)
B3LYP	1.417	109.5	2.314	1.646	90.0	2.327	3.291
B3LYP-GD3BJ	1.417	109.5	2.314	1.645	90.0	2.327	3.291
M06-2X	1.410	109.5	2.302	1.628	90.0	2.303	3.257

[a] The optimized structures were determined using the density functional indicated with a 6-311+G(d,p) basis set. Ideal tetrahedral geometry observed for $[BF_4]^-$ and ideal octahedral geometry observed for $[PF_6]^-$ resulting in identical bond lengths and bond angles in the respective anion.

Table S3. Geometric Parameters of the B3LYP, B3LYP-GD3BJ, and M06-2X Ground Conformers of the $[C_nmim]^+$ Cations[a]

cation	theory	a1	a2	a3	a4	a5	a6	a7
$[C_2mim]^+$	B3LYP	-104.6						
	B3LYP-GD3BJ	-104.6						
	M06-2X	-108.0						
$[C_4mim]^+$	B3LYP	-100.1	-179.7	-179.6				
	B3LYP-GD3BJ	-103.5	61.9	177.3				
	M06-2X	-106.2	59.1	175.5				
$[C_6mim]^+$	B3LYP	-102.1	180.0	180.0	180.0	180.0		
	B3LYP-GD3BJ	-104.5	60.9	176.4	179.5	179.7		
	M06-2X	-106.4	58.9	174.0	179.2	179.4		
$[C_8mim]^+$	B3LYP	-103.0	179.3	179.8	179.5	180.0	179.7	180.0
	B3LYP-GD3BJ	-103.4	60.5	176.1	179.5	179.6	180.0	179.9
	M06-2X	-104.9	59.2	174.7	180.0	179.8	179.6	180.0

[a]The torsion angles are given in degrees (°) and describe the following dihedral angles: a1 = ∠C2N1C1′C2′, a2 = ∠N1C1′C2′C3′, a3 = ∠C1′C2′C3′C4′, a4 = ∠C2′C3′C4′C5′, a5 = C3′C4′C5′C6′, a6 = C4′C5′C6′C7′, and a7 = ∠C5′C6′C7′C8′. The optimized structures were optimized using the density functional indicated with a 6-311+G(d,p) basis set.

Table S4. Geometric Parameters of the B3LYP, B3LYP-GD3BJ, and M06-2X Ground Conformers of the ($C_n$mim:PF_6) Ion Pairs[a]

ion pair	theory	∠C2N3C1″H	a1[b]	∠C2HP	b[c]	b1[d]
(C_2mim:PF_6)	B3LYP	-4.8	-93.9	119.7	-3.9	46.6
	GD3BJ	28.4	113.0	102.5	-1.2	58.6
	M06-2X	-22.8	-116.8	92.6	-1.3	-65.6
(C_4mim:PF_6)	B3LYP	-16.7	-94.1	120.8	0.5	49.4
	GD3BJ	14.7	-103.3	110.9	-0.2	-56.2
	M06-2X	-24.6	-112.9	93.8	-1.3	-64.0
(C_6mim:PF_6)	B3LYP	16.2	-103.5	121.3	0.1	-49.7
	GD3BJ	1.8	-122.8	116.0	-5.9	-47.3
	M06-2X	-25.1	-111.8	94.0	-1.1	-63.9
(C_8mim:PF_6)	B3LYP	15.4	-103.9	120.4	-0.0	-50.1
	GD3BJ	16.1	-78.3	114.4	-7.7	-52.2
	M06-2X	-24.9	-111.4	93.9	-1.2	-63.9
ion pair	theory	C1′H-F	C2H-F	C1″H-F	C2-F	C2-P
(C_2mim:PF_6)	B3LYP	2.264	2.273, 2.103	2.321	2.766	3.568
	GD3BJ	2.445	2.272, 2.311	2.673	2.691	3.462
	M06-2X	2.389	2.319, 2.372	2.590	2.683	3.382
(C_4mim:PF_6)	B3LYP	2.275	2.169, 2.202	2.255	2.758	3.575
	GD3BJ	2.418	2.221, 2.252	2.265	2.672	3.500
	M06-2X	2.354	2.322, 2.362	2.613	2.678	3.393
(C_6mim:PF_6)	B3LYP	2.498	2.154, 2.222	2.273	2.798	3.591
	GD3BJ	2.447	2.190, 2.208	2.230	2.702	3.524
	M06-2X	2.349	2.313, 2.378	2.633	2.677	3.397
(C_8mim:PF_6)	B3LYP	2.493	2.175, 2.216	2.281	2.779	3.584
	GD3BJ	3.405	2.075, 2.603	2.114	2.667	3.594
	M06-2X	2.356	2.311, 2.384	2.627	2.678	3.398

[a] Bond and dihedral angles are given in degrees (°), bond distances are given in Angstroms (Å). Optimized structures were determined using the density functional indicated with a 6-311+G(d,p) basis set. See Figure S2 for additional details regarding the definitions of the dihedral angles. [b]First 1-alkyl dihedral angle a1 ≡ ∠C2N1C1′C2′. [c]Binding site dihedral angle defined as **b** ≡ ∠(C2,©,©+CP,P) where © denotes the centroid of the imidazolium ring. [d]Binding orientation dihedral angle defined as **b1** ≡ ∠C1″N3C2P.

Table S5. Geometric Parameters of the B3LYP, B3LYP-GD3BJ, and M06-2X Ground Conformers of the $[2C_nmim:PF_6]^+$ Clusters[a]

system	theory	∠C2N3C1″H	a1[b]	∠C2HP	**b**[c]	**b1**[d]	**b2**[e]
$[2C_2mim:PF_6]^+$	B3LYP	-11.4	-100.9	132.0	-0.7	41.5	41.3
		14.6	-104.2	133.9	1.7	-41.8	
	B3LYP-GD3BJ	-12.9	110.7	106.8	-1.6	60.7	83.8
		-12.9	110.7	106.8	-1.6	60.7	
	M06-2X	15.7	120.6	89.9	-1.0	70.6	81.2
		18.8	-25.7	87.0	-3.9	71.3	
$[2C_4mim:PF_6]^+$	B3LYP	-14.8	103.7	137.3	1.9	39.1	29.9
		-14.5	103.6	137.4	2.1	39.0	
	B3LYP-GD3BJ	-15.1	106.9	109.2	-0.2	59.8	89.3
		-15.1	106.9	109.2	-0.2	59.8	
	M06-2X	-18.1	-118.0	90.9	-0.4	-69.8	168.3
		21.2	-114.7	87.8	-4.0	69.7	
$[2C_6mim:PF_6]^+$	B3LYP	-9.3	-101.5	134.0	-2.4	38.5	106.5
		-12.8	102.8	135.6	1.2	40.0	
	B3LYP-GD3BJ	-18.4	104.1	111.1	0.3	58.8	94.9
		-18.4	104.1	111.1	0.3	58.8	
	M06-2X	19.0	118.5	91.2	-0.9	69.2	86.0
		19.0	118.5	91.2	-0.9	69.2	
$[2C_8mim:PF_6]^+$	B3LYP	-12.0	-103.0	136.9	-0.5	37.8	-66.4
		14.8	-102.2	131.8	0.0	-42.8	
	B3LYP-GD3BJ	-17.5	97.2	115.6	0.2	55.4	67.1
		19.1	-102.8	110.4	1.1	-59.8	
	M06-2X	22.0	-112.7	88.6	-5.0	68.2	-62.7
		-20.6	113.4	88.1	-4.3	-69.3	

system	theory	C1′H–F	C2H–F	C1″H–F	C2–F	C2–P
$[2C_2mim:PF_6]^+$	B3LYP	2.441	2.251, 2.230	2.405	3.146	3.764
		2.666	2.146, 2.321	2.420	3.203	3.782
	B3LYP-GD3BJ	2.598	2.353, 2.366	2.376	2.842	3.557
		2.598	2.353, 2.366	2.376	2.843	3.557
	M06-2X	2.497	2.419, 2.495	2.661	2.810	3.423
		2.494	2.560, 2.470	2.710	2.838	3.435
$[2C_4mim:PF_6]^+$	B3LYP	2.686	2.145, 2.311	2.428	3.242	3.805
		2.662	2.156, 2.295	2.437	3.244	3.805
	B3LYP-GD3BJ	2.549	2.330, 2.364	2.406	2.845	3.573
		2.549	2.330, 2.364	2.406	2.845	3.573
	M06-2X	2.458	2.431, 2.484	2.713	2.787	3.431
		2.524	2.567, 2.442	2.718	2.821	3.432
$[2C_6mim:PF_6]^+$	B3LYP	2.475	2.221, 2.254	2.396	3.160	3.777
		2.589	2.214, 2.235	2.443	3.236	3.796
	B3LYP-GD3BJ	2.557	2.302, 2.372	2.389	2.865	3.588
		2.557	2.302, 2.372	2.389	2.865	3.588
	M06-2X	2.466	2.431, 2.471	2.707	2.797	3.430
		2.466	2.431, 2.471	2.707	2.797	3.430
$[2C_8mim:PF_6]^+$	B3LYP	2.478	2.184, 2.256	2.384	3.256	3.806
		2.680	2.216, 2.283	2.391	3.135	3.765
	B3LYP-GD3BJ	2.596	2.235, 2.401	2.424	2.915	3.631
		2.531	2.303, 2.473	2.476	2.808	3.603
	M06-2X	2.506	2.557, 2.415	2.700	2.836	3.432
		2.507	2.568, 2.413	2.689	2.835	3.429

[a] Bond and dihedral angles are given in degrees (°), bond distances are given in Angstroms (Å). Optimized structures were determined using the indicated density functional with a 6-311+G(d,p) basis set. See Figure S2 for dihedral definitions. [b]First 1-alkyl dihedral angle a1 ≡ ∠C2N1C1C2′. [c]Binding site dihedral angle defined as **b** ≡ ∠(C2,©,©+CP,P) where © denotes the centroid of the imidazolium ring. [d]Binding orientation dihedral angle defined as **b1** ≡ ∠C1″N3C2P. [e]Relative cation binding orientation dihedral angle defined as **b2** ≡ ∠C1′N1N1C1′.

Table S6. Vibrational Frequencies and Average Vibrational Energies of the $[2C_nmim:PF_6]^+$ Clusters, ($C_nmim:PF_6$) Ion Pairs, and $[C_nmim]^+$ Cations[a]

System	E_{int}, eV[b]	Frequencies (Degeneracies)
$[2C_2mim:PF_6]^+$	0.71 (0.05)	4, 12, 15, 17, 29, 36, 37, 46, 57, 59, 66, 74, 83, 98, 107, 112, 144, 149, 206, 213, 234(2), 281, 295, 297(2), 299, 383(2), 425, 429, 438, 441, 446, 524, 525, 528, 534, 541, 595, 596, 636(2), 665, 666, 685, 701(2), 747, 748, 806, 809, 810, 826, 834, 867, 869, 903, 908, 963(2), 1037, 1038, 1045(2), 1103, 1104, 1108, 1109, 1122(2), 1138, 1143, 1155(2), 1177, 1179, 1272, 1275, 1313(2), 1347, 1349, 1385, 1391, 1413, 1414, 1426(2), 1447, 1449, 1464(2), 1493, 1494, 1495, 1497(2), 1499, 1511(2), 1513, 1514, 1596(2), 1605(2), 3042, 3043, 3065, 3066, 3075, 3079, 3107, 3108, 3117, 3125, 3139, 3140, 3143(2), 3169, 3170, 3276(2), 3283, 3288, 3294(2)
$[2C_4mim:PF_6]^+$	0.87 (0.06)	7, 9, 12, 15, 19, 25, 31, 34, 39, 41, 49, 68, 71, 76, 82, 83, 98, 105, 107, 112, 121(2), 201, 202, 239, 240, 247(2), 277(2), 280, 294, 300, 321(2), 405(2), 436, 441(2), 442, 446, 523, 524, 527, 531, 545, 629(2), 636(2), 668(2), 686, 736(2), 746(2), 748, 749, 805, 806, 808, 813, 844, 868(2), 900, 904, 917(2), 952(2), 1012(2), 1037(2), 1045(2), 1058(2), 1107(2), 1122(2), 1129(2) 1153(2), 1158(2), 1178, 1180, 1240(2), 1299(2), 1305(2), 1323(2), 1342(2), 1349(2), 1383(2), 1402(2), 1415(2), 1420(2), 1445(2), 1463(2), 1492, 1493(2), 1494, 1496, 1497, 1501(2), 1503, 1504, 1510, 1511, 1515(2), 1596, 1597, 1604(2), 3012(2), 3023(2), 3028(2), 3043(2), 3065(2), 3065(2), 3079, 3080, 3091(2), 3099(2), 3127(2), 3142(2), 3168(2), 3276(2), 3284, 3285, 3295(2)
$[2C_6mim:PF_6]^+$	1.02 (0.07)	2, 9, 11, 13, 16, 21, 27, 34, 37, 42, 48, 50, 53, 59, 64, 66, 78, 82, 88, 104, 117, 123, 126, 131, 137, 141, 142, 150, 217, 218, 238, 240, 243, 246, 281, 283, 286, 295(2), 297, 299, 408, 410, 436, 438, 439, 441, 446, 450, 455, 524(2), 528, 533, 542, 628, 630, 636, 637, 669, 671, 686, 735, 738, 739, 742, 747(2), 752, 754, 802, 803, 807, 829, 833, 866, 867, 896, 897, 899, 900, 901, 904, 1003(2), 1008(2), 1036, 1038(3), 1043, 1044, 1051(2), 1065, 1066, 1107(2), 1122(2), 1136(2), 1154, 1156, 1157, 1160, 1174, 1177, 1221, 1222, 1263, 1264, 1274(2), 1302, 1303, 1322, 1323, 1328(2), 1337(2), 1340, 1341, 1350(2), 1380, 1382, 1399(2), 1404(2), 1416, 1418(2), 1419, 1445, 1447, 1463, 1464, 1487, 1488, 1489, 1490, 1494(2), 1497(2), 1499, 1501(2), 1502, 1509, 1511(2), 1512, 1516, 1518, 1596(2), 1604, 1605, 2998, 2999, 3003, 3004, 3012(2), 3018, 3019, 3022(2), 3023, 3024, 3032, 3035, 3048, 3051, 3063, 3064, 3065, 3066, 3073, 3078, 3082, 3084, 3091, 3093, 3128, 3130, 3142(2), 3167, 3169, 3276(2), 3288, 3289, 3295(2)
$[2C_8mim:PF_6]^+$	1.17 (0.08)	5, 6, 9, 12, 16, 19, 26, 30, 33, 35, 38, 42, 43, 44, 55, 57, 62, 64, 77, 87, 92, 94, 96, 101, 105, 106, 110, 121, 145, 149, 154, 160, 176, 177, 196, 201, 238, 243(2), 246, 281, 283, 285, 296, 298, 312, 313, 375, 377, 419(2), 438, 441, 446, 449(2), 493, 494, 524(2), 527, 534, 541, 628, 630, 638(2), 670, 671, 685, 733, 734, 738, 739(2), 742, 748(2), 758, 759, 802, 804, 810, 827, 832, 866, 868, 872, 875, 898, 899, 901, 907, 956, 958, 995(2), 1006(2), 1034(2), 1037, 1038, 1040, 1041, 1047, 1048, 1061, 1063, 1065, 1066, 1073, 1074, 1107(2), 1122(2), 1139(2), 1155(2), 1158, 1160, 1176, 1177, 1212, 1213, 1246, 1247, 1253, 1254, 1289(2), 1295, 1296, 1308(2), 1327, 1328, 1331(2), 1339, 1340, 1343(2), 1344(2), 1351(2), 1379, 1381, 1396, 1397, 1403, 1404(2), 1406, 1415, 1416, 1417, 1418, 1445, 1447, 1463(2), 1486(2), 1487(2), 1491(2), 1493(2), 1496, 1497, 1498, 1499, 1500, 1501, 1505, 1507, 1511(2), 1513, 1514, 1517, 1518, 1595, 1596, 1604(2), 2994, 2995, 2997, 2998, 3001, 3002, 3007, 3008, 3012(3), 3013, 3020(3), 3021, 3022, 3024, 3031, 3032, 3042, 3044, 3053, 3056, 3064, 3065(2), 3066, 3073, 3080(2), 3082, 3088, 3089, 3128(2), 3142(2), 3168, 3169, 3276, 3277, 3286, 3289, 3294, 3295
($C_2mim:PF_6$)	0.42 (0.03)	3, 32, 36, 57, 69, 81, 99, 117, 166, 214, 238, 285, 293, 297, 303, 386, 426, 438, 442, 444, 511, 522, 526, 528(2), 596, 635, 669, 671, 705, 737, 806, 828, 832, 846, 857, 928, 965, 1039, 1047, 1104, 1109, 1120, 1138, 1157, 1179, 1272, 1313, 1352, 1393, 1413, 1424, 1455, 1464, 1493, 1497, 1501, 1510, 1514, 1596, 1605, 3037, 3060, 3079, 3102, 3113, 3139(2), 3165, 3277, 3279, 3295

Table S6. Vibrational Frequencies and Average Vibrational Energies of the $[2C_nmim:PF_6]^+$ Clusters, ($C_nmim:PF_6$) Ion Pairs, and $[C_nmim]^+$ Cations[a]

System	E_{int}, eV[b]	Frequencies (Degeneracies)
($C_4mim:PF_6$)	0.49 (0.04)	11, 16, 34, 53, 60, 64, 76, 87, 112, 118, 139, 213, 241, 251, 284, 288, 293, 297, 318, 418, 431, 438, 441, 445, 513, 521, 527(2), 528, 628, 639, 670, 672, 735, 742, 747, 803, 828, 832, 844, 854, 912, 926, 949, 1015, 1039, 1046, 1062, 1109, 1120, 1131, 1153, 1158, 1178, 1238, 1294, 1301, 1320, 1336, 1355, 1389, 1402, 1415, 1421, 1455, 1465, 1491, 1494, 1501, 1503, 1506, 1511, 1517, 1596, 1604, 3010, 3017, 3024, 3039, 3058, 3060, 3074, 3086, 3095, 3130, 3139, 3166, 3277, 3280, 3295
($C_6mim:PF_6$)	0.57 (0.04)	18, 19, 33, 40, 48, 56, 67, 74, 91, 99, 119, 129, 146, 150, 226, 244, 246, 284, 286, 293, 296, 299, 410, 438, 439, 441, 443, 457, 514, 521, 527(2), 528, 629, 642, 671, 674, 735, 738, 741, 752, 802, 824, 832, 843, 858, 897, 900, 924, 1003, 1008, 1036, 1039, 1044, 1051, 1065, 1108, 1121, 1136, 1156, 1161, 1177, 1222, 1264, 1274, 1303, 1324, 1327, 1337, 1342, 1352, 1377, 1398, 1404, 1415, 1416, 1450, 1463, 1487, 1489, 1494, 1499, 1500, 1501, 1509, 1510, 1515, 1596, 1604, 2994, 2997, 3005, 3014, 3019, 3028, 3037, 3055, 3060, 3060, 3081, 3086, 3093, 3132, 3138, 3165, 3277, 3282, 3296
($C_8mim:PF_6$)	0.64 (0.05)	12, 14, 30, 33, 40, 47, 59, 63, 75, 91, 98, 106, 113, 128, 148, 155, 179, 212, 245, 247, 285, 287, 293, 295, 315, 379, 420, 438, 441, 443, 450, 496, 515, 521, 526, 527, 528, 629, 641, 671, 673, 732, 737, 738, 741, 758, 803, 824, 832, 844, 858, 874, 898, 917, 958, 995, 1006, 1034, 1038, 1041, 1048, 1062, 1066, 1073, 1108, 1121, 1139, 1156, 1163, 1175, 1214, 1247, 1254, 1288, 1297, 1307, 1328, 1332, 1339, 1343, 1345, 1354, 1378, 1397, 1403, 1407, 1415, 1417, 1450, 1463, 1485, 1486, 1490, 1493, 1497, 1500, 1501, 1504, 1509, 1511, 1516, 1595, 1604, 2992, 2994, 2996, 3001, 3006, 3014, 3015, 3018, 3025, 3035, 3045, 3058, 3059, 3060, 3079, 3083, 3095, 3132, 3138, 3165, 3278, 3281, 3296
$[C_2mim]^+$	0.19 (0.02)	46, 69, 135, 209, 233, 292, 378, 425, 592, 633, 660, 698, 753, 803, 834, 881, 962, 1036, 1043, 1099, 1102, 1125, 1136, 1150, 1175, 1270, 1311, 1343, 1385, 1411, 1428, 1437, 1461, 1484, 1491, 1494, 1509, 1510, 1595, 1604, 3046, 3070, 3079, 3110, 3122, 3134, 3150, 3165, 3274, 3278, 3292
$[C_4mim]^+$	0.27 (0.03)	28, 65, 69, 83, 112, 199, 237, 247, 273, 318, 407, 434, 626, 632, 664, 733, 741, 752, 801, 834, 879, 916, 946, 1010, 1037, 1042, 1054, 1100, 1125, 1128, 1147, 1150, 1175, 1234, 1295, 1299, 1318, 1336, 1345, 1381, 1395, 1412, 1424, 1436, 1460, 1484, 1489, 1492, 1502, 1502, 1510, 1515, 1594, 1603, 3015, 3025, 3032, 3041, 3065, 3069, 3072, 3094, 3108, 3121, 3149, 3165, 3274, 3279, 3292
$[C_6mim]^+$	0.34 (0.03)	28, 49, 52, 63, 76, 124, 131, 147, 214, 238, 245, 278, 294, 408, 437, 449, 626, 631, 666, 736, 737, 750, 754, 802, 833, 881, 897, 901, 1001, 1007, 1035, 1037, 1041, 1046, 1062, 1099, 1125, 1135, 1149, 1154, 1174, 1219, 1262, 1272, 1303, 1320, 1326, 1336, 1340, 1344, 1378, 1394, 1401, 1412, 1420, 1436, 1460, 1484, 1488, 1489, 1493, 1500, 1502, 1510(2), 1517, 1595, 1603, 3001, 3006, 3015, 3022, 3024, 3026, 3035, 3051, 3067, 3068, 3072, 3086, 3098, 3122, 3148, 3164, 3274, 3277, 3291
$[C_8mim]^+$	0.42 (0.03)	20, 38, 40, 53, 69, 93, 96, 107, 149, 156, 175, 193, 242(2), 279, 311, 374, 416, 448, 492, 626, 631, 666, 734, 736, 738, 752, 757, 801, 833, 872, 880, 900, 955, 994, 1003, 1032, 1036, 1038, 1044, 1059, 1064, 1072, 1100, 1125, 1138, 1148, 1155, 1172, 1211, 1245, 1251, 1286, 1294, 1306, 1322, 1329, 1338, 1340, 1342, 1345, 1378, 1392, 1402, 1403, 1412, 1419, 1435, 1461, 1484, 1486, 1487, 1491(2), 1497, 1501, 1505, 1511, 1512, 1517, 1594, 1603, 2996, 2999, 3004, 3009, 3014(2), 3022(2), 3025, 3032, 3044, 3055, 3068(2), 3072, 3083, 3092, 3121, 3148, 3164, 3275, 3277, 3292

[a] Determined at the B3LYP/6-311+G(d,p) level of theory and with frequencies scaled by 0.9887. [b] Uncertainties are listed in parentheses.

Table S7. Rotational Constants of $[2C_nmim:PF_6]^+$ Clusters and the Corresponding PSL TS

system	energized molecule		transition state		
	1-D[a]	2-D[b]	1-D[c]	2-D[c]	2-D[d]
$[2C_2mim:PF_6]^+$	0.016048	0.003288	0.178019, 0.027336	0.039347, 0.010593	0.0011
$[2C_4mim:PF_6]^+$	0.007645	0.002697	0.132015, 0.016472	0.016727, 0.007476	0.0006
$[2C_6mim:PF_6]^+$	0.004448	0.001658	0.110309, 0.012087	0.008309, 0.006038	0.0006
$[2C_8mim:PF_6]^+$	0.002676	0.001880	0.096457, 0.011816	0.004695, 0.003613	0.0005

[a] Active external. [b] Inactive external. [c] Rotational constants of the transition state treated as free internal rotors. [d] Two-dimensional rotational constants of the transition state at threshold, treated variationally and statistically.

Figure Captions

Figure S1. Cross sections for collision-induced dissociation of the $[2C_nmim:PF_6]^+$ clusters with Xe as a function of collision energy in the center-of-mass frame (lower *x*-axis) and laboratory frame (upper *x*-axis); data for n = 2, 4, 6 and 8 are shown in parts a-d, respectively. The data shown were acquired at a Xe pressure of 0.2 mTorr. Refer to **Table S1** for CID product legends.

Figure S2. Nomenclature employed in this work to describe the stable conformations predicted for the $[C_nmim]^+$ cations, ($C_nmim:PF_6$) ion pairs, and $[2C_nmim:PF_6]^+$ clusters.

Figure S3. Noncovalent interaction maps superimposed on the B3LYP/6-311+G(d,p) optimized geometries of the ground and stable low-energy conformers of the ($C_2mim:PF_6$) ion pair. For the ($\mathbf{g}_+\mathbf{F};g_{+}$)2 conformer the NCI map is superimposed on the B3LYP-GD3BJ/6-311+G(d,p) optimized geometry. Conformer designations along with the B3LYP/6-311+G(2d,2p), B3LYP-GD3BJ/6-311+G(2d,2p) and M06-2X/6-311+G(2d,2p) relative Gibbs energies at 298 K (in kJ/mol) are also given.

Figure S4. Noncovalent interaction maps superimposed on the B3LYP/6-311+G(d,p) optimized geometries of the ground and stable low-energy conformers of the ($C_4mim:PF_6$) ion pair. Conformer designations along with the B3LYP/6-311+G(2d,2p), B3LYP-GD3BJ/6-311+G(2d,2p) and M06-2X/6-311+G(2d,2p) relative Gibbs energies at 298 K (in kJ/mol) are also given.

Figure S5. Noncovalent interaction maps superimposed on the B3LYP/6-311+G(d,p) optimized geometries of the ground and stable low-energy conformers of the ($C_6mim:PF_6$) ion pair. Conformer designations along with the B3LYP/6-311+G(2d,2p), B3LYP-GD3BJ/6-311+G(2d,2p) and M06-2X/6-311+G(2d,2p) relative Gibbs energies at 298 K (in kJ/mol) are also given.

Figure S6. Noncovalent interaction maps superimposed on the B3LYP/6-311+G(d,p) optimized geometries of the ground and stable low-energy conformers of the ($C_8mim:PF_6$) ion pair. For the ($\mathbf{g\_F};g_{-2}t_2g_{+2}t$) conformer, the NCI map is superimposed on the B3LYP-GD3BJ/6-311+G(d,p) optimized structure. Conformer designations along with the B3LYP/6-311+G(2d,2p), B3LYP-GD3BJ/6-311+G(2d,2p) and M06-2X/6-311+G(2d,2p) relative Gibbs energies at 298 K (in kJ/mol) are also given.

Figure S7. Electrostatic potential maps of the B3LYP/6-311+G(d,p) and M06-2X/6-311+G(d,p) ground conformers of the ($C_nmim:PF_6$) ion pairs at an isosurface of 0.01 a.u. of the total SCF electron density calculated using the 6-311+G(2d,2p) basis set. The Mülliken charges on the hydrogen atoms of the cation and fluorine atoms of the anion are labeled. The most electropositive regions are color-coded in blue and occur at the hydrogen atoms of the 3-methylimidizolium moiety, with the C2H atom displaying the greatest Mülliken charge. The most electronegative regions are color-coded in red, and occur at the fluorine atoms of the anion. Regions of intermediate ESP are shown in green and become more prevalent as the size of the 1-alkyl substituent increases.

Figure S8. B3LYP/6-311+G(d,p) optimized geometries of the ground and stable low-energy conformers of the $[2C_2mim:PF_6]^+$ cluster. For the $[g_+;\mathbf{g_+g_+Fg_+F};g_+]^+$ and $[g_+;\mathbf{g_+g_+Fg_+F};c]^+$ conformers, the NCI maps are superimposed on the B3LYP-GD3BJ/6-311+G(d,p) and M06-2X/6-311+G(d,p) optimized structures, respectively. Conformer designations along with the B3LYP/6-311+G(2d,2p), B3LYP-GD3BJ/6-311+G(2d,2p) and M06-2X/6-311+G(2d,2p) relative Gibbs energies at 298 K (in kJ/mol) are also given.

Figure S9. B3LYP/6-311+G(d,p) optimized geometries of the ground and stable low-energy conformers of the $[2C_4mim:PF_6]^+$ cluster. For the $[g_+t_2;\mathbf{g_+g_+Fg_+F};g_+t_2]^+$ and $[g_-t_2;\mathbf{tg_-Fg_+F};g_-t_2]^+$ conformers, the NCI maps are superimposed on the B3LYP-GD3BJ/6-311+G(d,p) and M06-2X/6-311+G(d,p) optimized structures respectively. Conformer designations along with the B3LYP/6-311+G(2d,2p), B3LYP-GD3BJ/6-311+G(2d,2p) and M06-2X/6-311+G(2d,2p) relative Gibbs energies at 298 K (in kJ/mol) are also given.

Figure S10. B3LYP/6-311+G(d,p) optimized geometries of the ground and stable low-energy conformers of the $[2C_6mim:PF_6]^+$ cluster. For the $[g_+t_4;\mathbf{g_+g_+Fg_+F};g_+t_4]^+$ conformer, the NCI map is superimposed on the M06-2X/6-311+G(d,p) optimized structure. Conformer designations along with the B3LYP/6-311+G(2d,2p), B3LYP-GD3BJ/6-311+G(2d,2p) and M06-2X/6-311+G(2d,2p) relative Gibbs energies at 298 K (in kJ/mol) are also given.

Figure S11. B3LYP/6-311+G(d,p) optimized geometries of the ground and stable low-energy conformers of the $[2C_8mim:PF_6]^+$ cluster. For the $[g_+t_6;\mathbf{g_+g_+Fg_-F};g_-t_6]^+$ and $[g_-t_6;\mathbf{g_-g_+Fg_-F};g_+t_6]^+$ conformers, the NCI maps are superimposed on the B3LYP-GD3BJ/6-311+G(d,p) and M06-2X/6-311+G(d,p) optimized structures, respectively. Conformer designations along with the B3LYP/6-311+G(2d,2p), B3LYP-GD3BJ/6-311+G(2d,2p) and M06-2X/6-311+G(2d,2p) relative Gibbs energies at 298 K (in kJ/mol) are also given.

Figure S12. Electrostatic potential maps of the B3LYP/6-311+G(d,p) and M06-2X/6-311+G(d,p) ground conformers of the $[2C_nmim:PF_6]^+$ clusters at an isosurface of 0.01 a.u. of the total SCF electron density calculated using the 6-311+G(2d,2p) basis set. The Mülliken charges on the hydrogen atoms of the cations and fluorine atoms of the anion are labeled. The most electropositive regions are color-coded in blue and occur at the hydrogen atoms of the 3-methylimidizolium moiety, with the C2H atom displaying the greatest Mülliken charge. The most electronegative regions are color-coded in red, and occur at the fluorine atoms of the anion. Regions of intermediate ESP are shown in green and become more prevalent as the size of the 1-alkyl substituent increases.

Figure S13. B3LYP/6-311+G(d,p) isotropic molecular polarizabilities of the $[C_nmim]^+$ cations, ($C_nmim:PF_6$) ion pairs and $[2C_nmim:PF_6]^+$ clusters (solid lines), and PBE1PBE/6-311+G(2d,p) isotropic molecular polarizabilities of the ($C_nmim:PF_6$) ion pairs (dashed lines) as a function of n. All values are based on the B3LYP/6-311+G(d,p) optimized geometries for the ground conformers. The lines are linear regression fits to the data for each series.

Figure S14. Zero-pressure-extrapolated cross sections for collision-induced dissociation of the $[2C_nmim:PF_6]^+$ clusters with Xe as a function of the collision energy in the center-of-mass frame (lower *x*-axis) and laboratory frame (upper *x*-axis); data for n = 2, 4, 6 and 8 are shown in parts a-d, respectively. The solid lines show the best fits to the data convoluted over the neutral and ion kinetic and internal energy distributions. The dashed lines show the model cross sections in the absence of experimental kinetic energy broadening for reactants with an internal energy corresponding to 0 K.

Figure S15. Comparison of normalized zero-pressure-extrapolated cross sections for collision-induced dissociation of the $[2C_nmim:PF_6]^+$ clusters for n = 2, 4, 6, and 8.

Figure S16. Comparisons of the Maxwell-Boltzmann internal energy distribution used, part a. Comparisons of the computed Rice-Ramsperger-Kassel-Marcus unimolecular dissociation rate constants for the respective $[2C_nmim:PF_6]^+$ clusters, for n = 2, 4, 6, and 8, part b.

Figure S17. Comparisons of the zero-pressure-extrapolated cross sections for the CID of the $[2C_nmim:PF_6]^+$ and $[2C_nmim:BF_4]^+$ clusters for n = 2, 4, 6, and 8, parts a-d, respectively. Data for the $[2C_nmim:BF_4]^+$ clusters is taken from reference 41.

Figure S1.

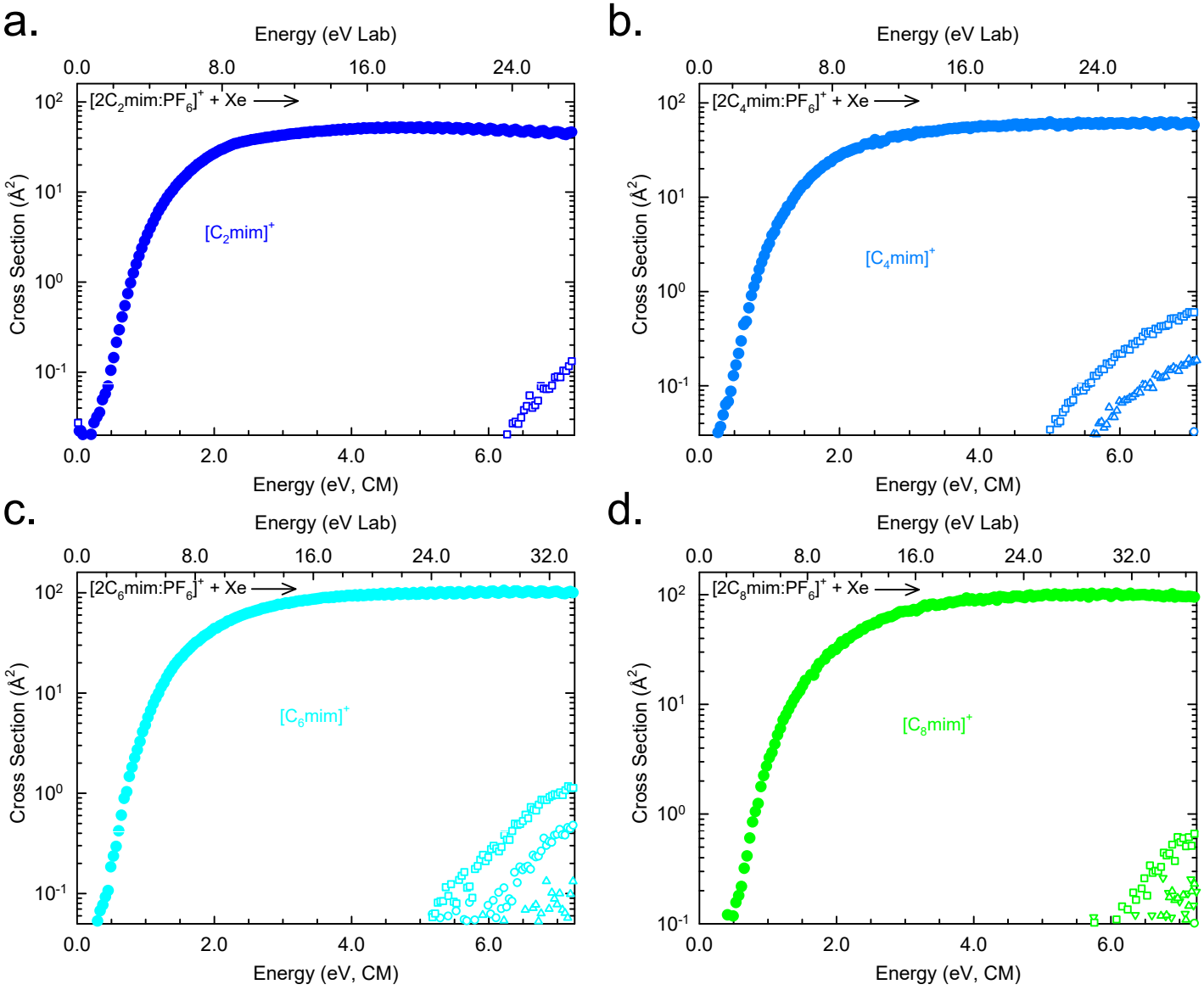
a.
Energy (eV Lab)
0.0
8.0
16.0
24.0
[2C2mim:PF6]+ + Xe
Cross Section (Å2)
[C2mim]+
0.0
2.0
4.0
6.0
Energy (eV, CM)
b.
Energy (eV Lab)
[2C4mim:PF6]+ + Xe
[C4mim]+
c.
Energy (eV Lab)
0.0
8.0
16.0
24.0
32.0
[2C6mim:PF6]+ + Xe
[C6mim]+
d.
Energy (eV Lab)
[2C8mim:PF6]+ + Xe
[C8mim]+

Figure S2.

$[C_n mim]^+$ Nomenclature

$[a1a2\ldots an\text{-}1]^+$

$[C_2mim]^+ = [a1]^+$

$[C_4mim]^+ = [a1a2a3]^+$

$[C_6mim]^+ = [a1a2a3a4a5]^+$

$[C_8mim]^+ = [a1a2a3a4a5a6a7]^+$

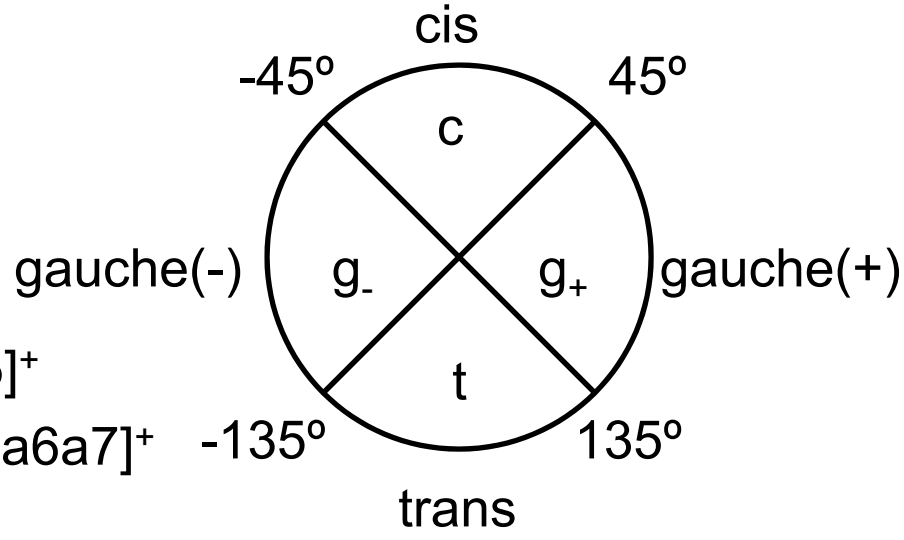

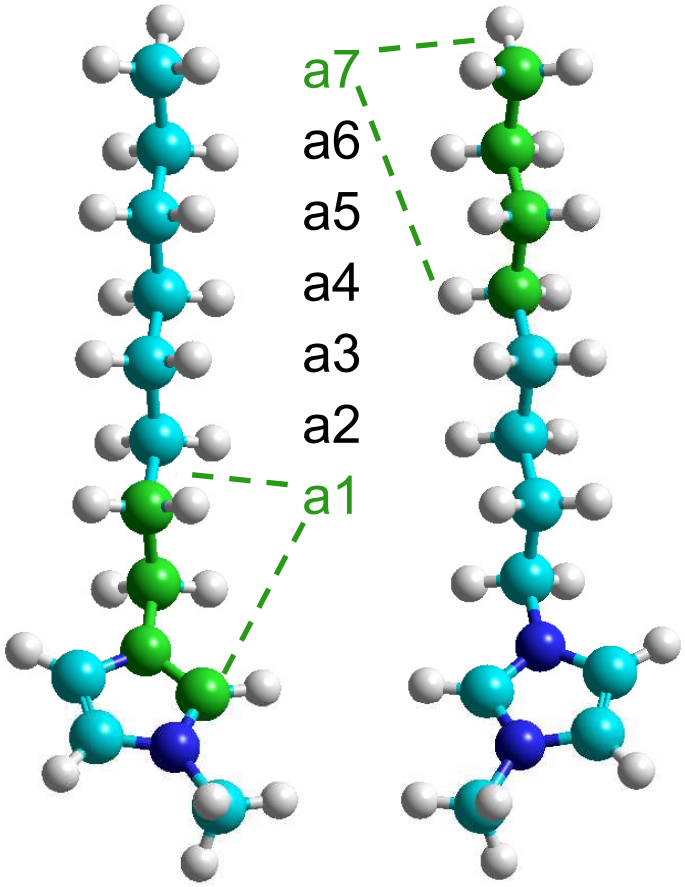

$[g_-ttttt]^+$ $[g_-t_6]^+$

$[g_+ttttt]^+$ $[g_+t_6]^+$

$[C_8mim]^+$

Dihedral Angle Classification

1-Alkyl Dihedral Angles

a1 = ∠C2N1C1′C2′
a2 = ∠N1C1′C2′C3′
a3 = ∠C1′C2′C3′C4′
a4 = ∠C2′C3′C4′C5′
a5 = ∠C3′C4′C5′C6′
a6 = ∠C4′C5′C6′C7′
a7 = ∠C5′C6′C7′C8′

Figure S2.

Binding Site (BS) Nomenclature

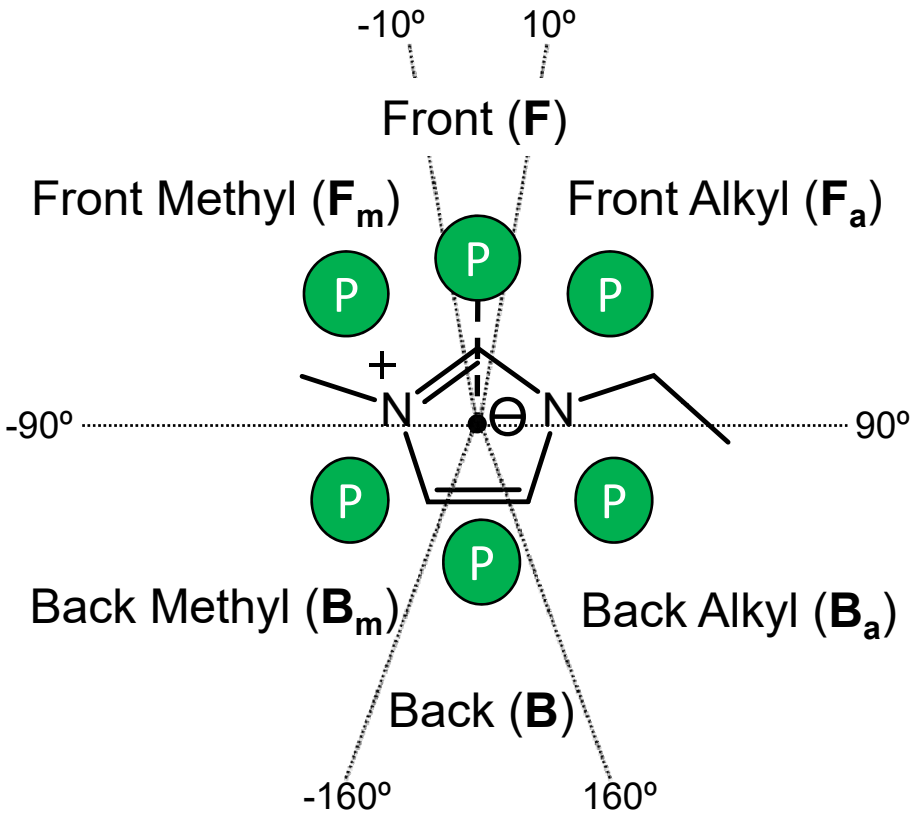

The **binding site** (**BS**) designation is readily described by the dihedral angle **b** = ∠(C2,©,©+CP,P), where © denotes the centroid of the imidazolium ring (N1C2N3C4C5) and CP denotes the cross product of the vectors that describe the C2-N1 and C2-N3 bonds, i.e., CP = $\overrightarrow{(C2\text{-}N1)}x\overrightarrow{(C2\text{-}N3)}$. The range of angles that define BS designations are shown in the figure above and the bar below.

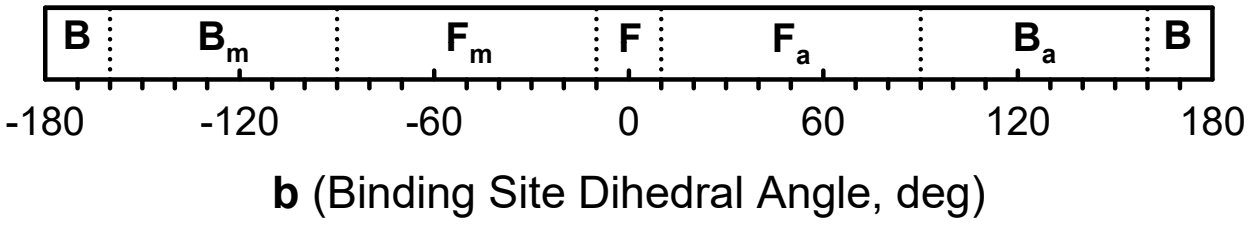

Figure S2.

Binding Site (BS) Nomenclature

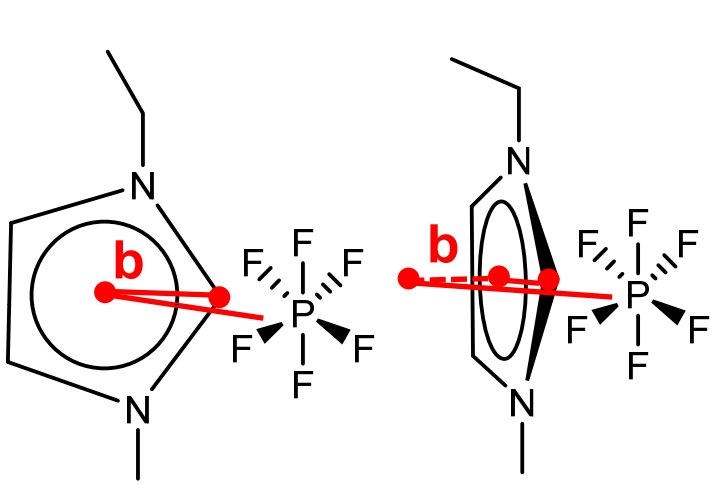

Front Binding (**F**)

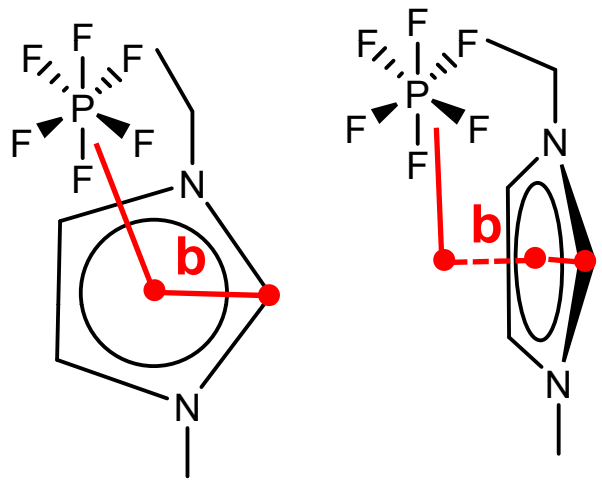

Back Alkyl Binding ($\mathbf{B_a}$)

The **binding site** (**BS**) designation is readily described by the dihedral angle **b** = ∠(C2,©,©+CP,P), where © denotes the centroid of the imidazolium ring (N1C2N3C4C5) and CP denotes the cross product of the vectors that describe the C2-N1 and C2-N3 bonds, i.e., CP = $\overrightarrow{(C2\text{-}N1)}x\overrightarrow{(C2\text{-}N3)}$. The range of angles that define BS designations are shown in the figure above and the bar below.

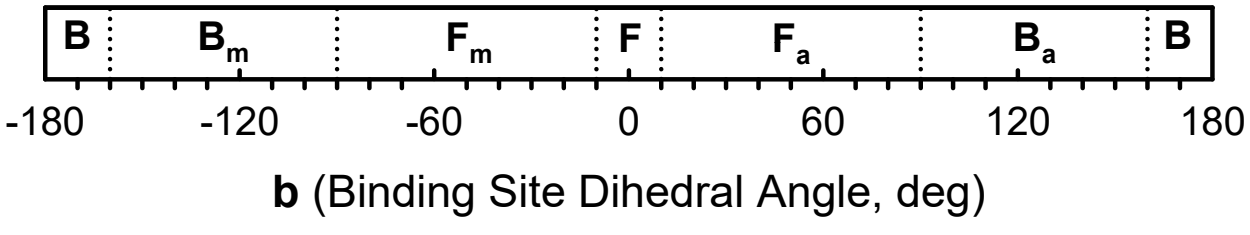

Figure S2.

($C_n$mim:PF_6) Nomenclature

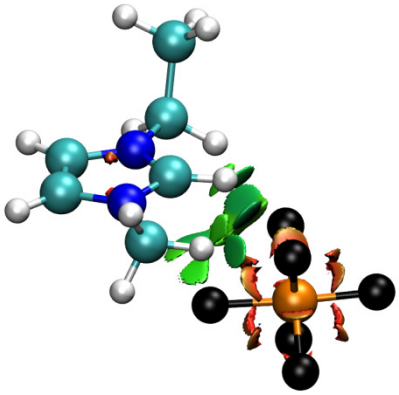

(C_2mim:PF_6)
(**g_+F;**g_-)

(**Binding Site**;Alkyl)

(**b1BS**;a1…an)

b1 = ∠C1″N3C2P

$[2C_n$mim:$PF_6]^+$ Nomenclature

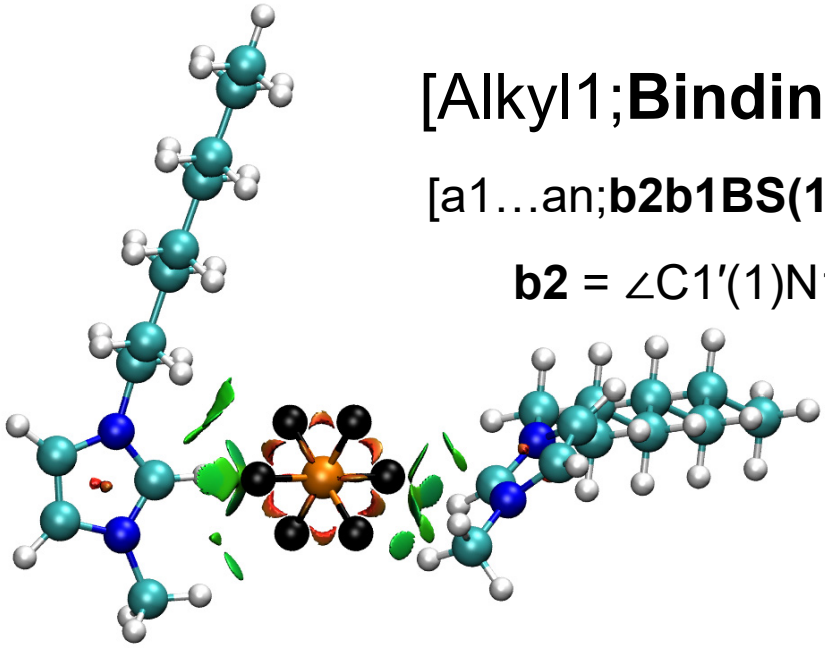

$[2C_8$mim:$PF_6]^+$
$[g\text{-}t_6$;**g-cFcF;**$g\text{-}t_6]^+$

[Alkyl1;**BindingSites**;Alkyl2]$^+$

[a1…an;**b2b1BS(1)b1BS(2)**; a1…an]$^+$

b2 = ∠C1′(1)N1(1)N1(2)C1′(2)

Figure S3.

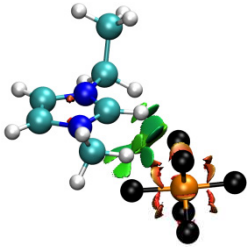

($\mathbf{g_+F}$;g_-)
0.0, – , –

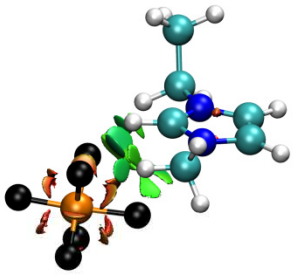

($\mathbf{g_-F}$;g_+)
0.0, –, 4.1

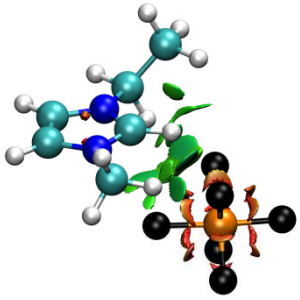

($\mathbf{g_+F}$;g_-)2
0.2, –, –

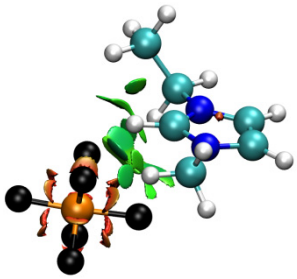

($\mathbf{g_-F}$;g_+)2
0.2, –, –

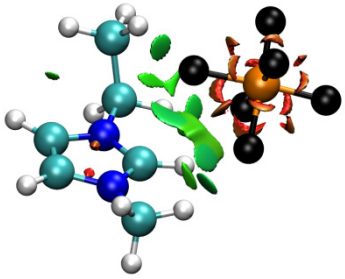

($\mathbf{g_-F}$;g_-)
0.6, 1.2, 0.0

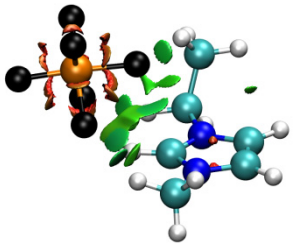

($\mathbf{g_+F}$;g_+)
0.6, 1.2, 0.0

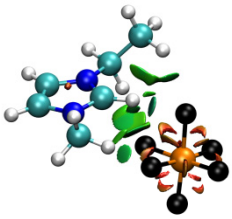

($\mathbf{g_+F}$;g_-)3
3.4, –, –

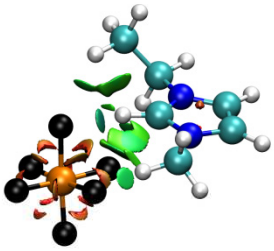

($\mathbf{g_-F}$;g_+)3
3.4, –, –

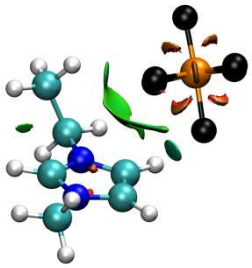

($\mathbf{tB_a}$;g_-)
27.4, –, –

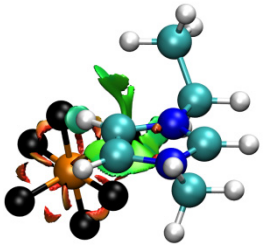

($\mathbf{tB_a}$;g_+)
27.7, –, –

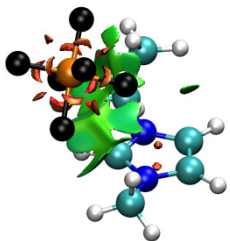

($\mathbf{g_+F}$;g_+)2
–, 0.0, –

(C_2mim:PF_6)

Figure S4.

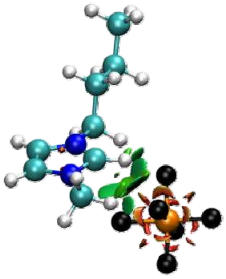

(**g**$_+$**F**;g$_-$t$_2$)
0.0, 8.9, –

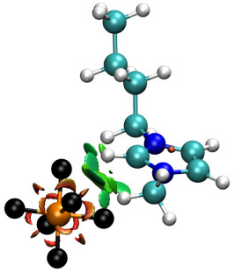

(**g**$_-$**F**;g$_+$t$_2$)
0.0, 8.9, –

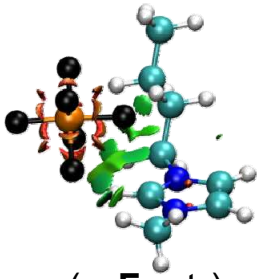

(**g**$_+$**F**;g$_+$t$_2$)
0.9, 0.0, 0.0

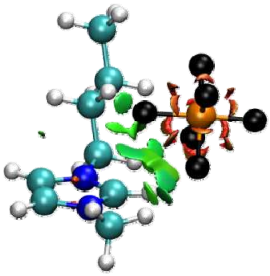

(**g**$_-$**F**;g$_-$t$_2$)
0.9, 0.9, 0.0

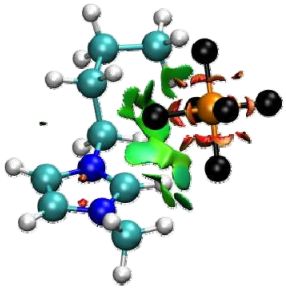

(**g**$_-$**F**;g$_-$tg$_-$)
1.3, 4.6, 2.3

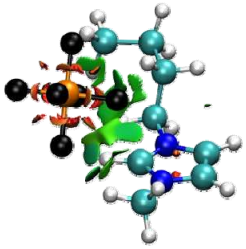

(**g**$_+$**F**;g$_+$tg$_+$)
1.3, 4.6, 2.3

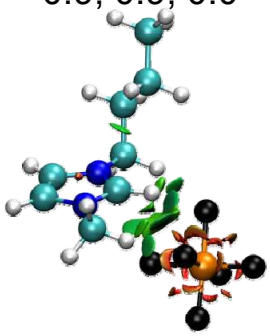

(**g**$_+$**F**;g$_-$g$_+$t)
1.9, 8.2, 6.2

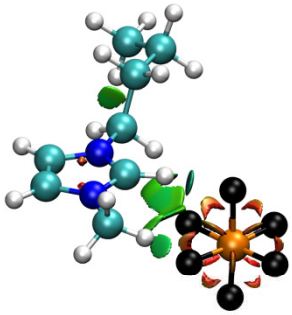

(**cF**;g$_-$tg$_+$)
2.1, –, –

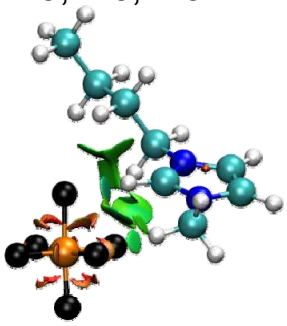

(**g**$_-$**F**;g$_+$t$_2$)
2.1, 8.9, –

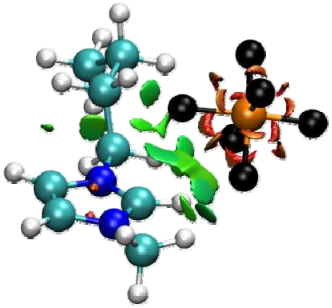

(**g**$_-$**F**;g$_-$tg$_+$)
2.5, 5.0, 4.1

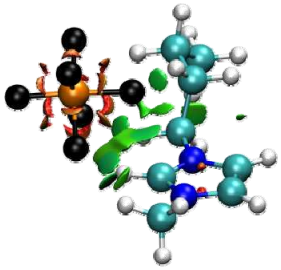

(**g**$_+$**F**;g$_+$tg$_-$)
2.5, 4.9, 4.1

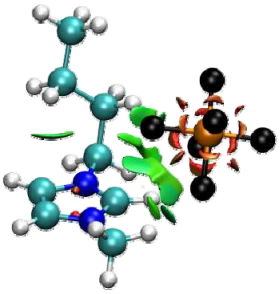

(**cF**;g$_{-2}$t)
3.1, –, –

(C$_4$mim:PF$_6$)

Figure S5.

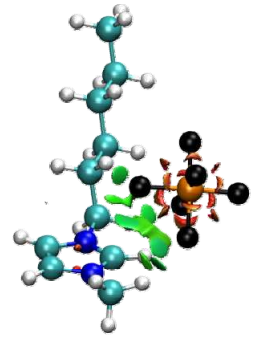

(**g**$_{-}$**F**;g$_{-}$t$_4$)
0.0, 0.0, 0.0

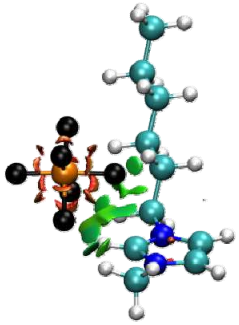

(**g**$_{+}$**F**;g$_{+}$t$_4$)
0.0, 0.0, 0.0

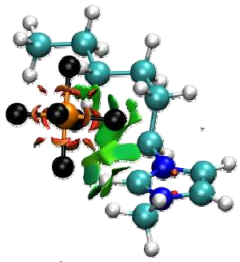

(**g**$_{+}$**F**;g$_{+}$tg$_{+}$t$_2$)
2.0, 3.6, 2.5

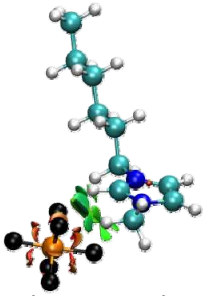

(**g**$_{-}$**F**;g$_{+}$t$_4$)
2.5, –, –

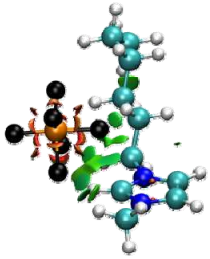

(**g**$_{+}$**F**;g$_{+}$t$_3$g$_{-}$)
2.6, 3.0, 0.1

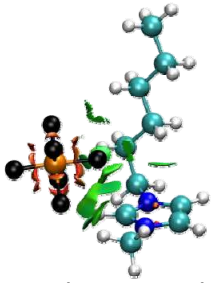

(**cF**;g$_{+2}$t$_3$)
2.7, –, –

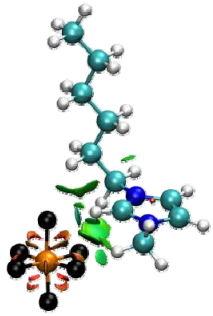

(**cF**;g$_{+2}$t$_3$)
3.7, –, –

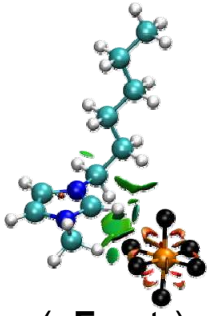

(**cF**;g$_{-2}$t$_3$)
3.7, –, –

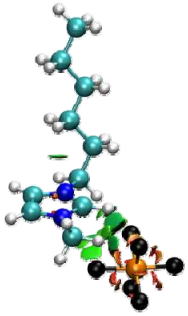

(**g**$_{+}$**F**;g$_{-2}$t$_3$)
4.3, 5.6, –

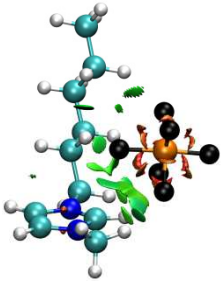

(**g**$_{-}$**F**;g$_{-}$t$_2$g$_{+}$t)
4.7, 2.4, 0.6

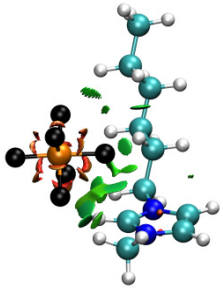

(**g**$_{+}$**F**;g$_{+}$t$_2$g$_{-}$t)
4.8, 2.4, 0.6

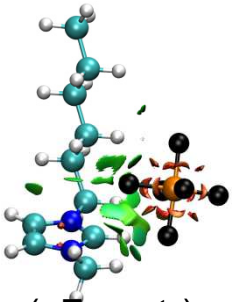

(**cF**;g$_{-}$g$_{+}$t$_3$)
4.9, –, –

(C$_6$mim:PF$_6$)

Figure S6.

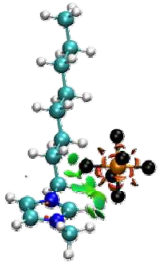

(**g**$_{-}$**F**;g$_{-}$t$_{6}$)
0.0, 7.9, 0.0

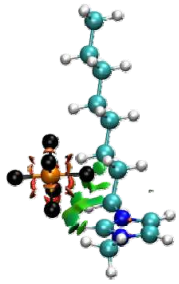

(**g**$_{+}$**F**;g$_{+}$t$_{6}$)
0.0, 7.9, 0.0

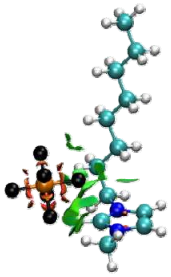

(**cF**;g$_{+2}$t$_{5}$)
6.4, –, –

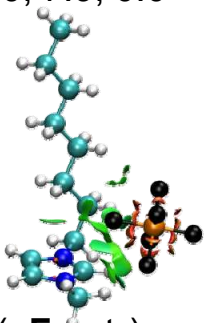

(**cF**;g$_{-2}$t$_{5}$)
6.4, –, –

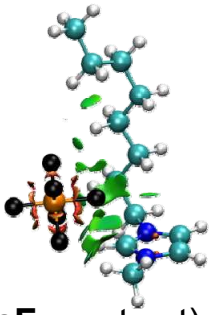

(**cF**$_{m}$;g$_{+2}$t$_{3}$g$_{+}$t)
6.6, –, –

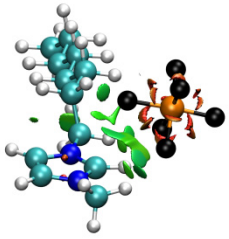

(**g**$_{-}$**F**;g$_{-}$tg$_{+}$t$_{4}$)
6.9, 9.7, 3.8

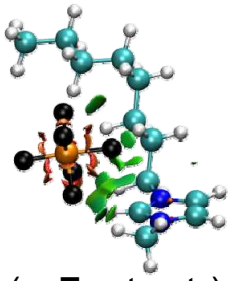

(**g**$_{+}$**F**;g$_{+}$t$_{3}$g$_{+}$t$_{2}$)
6.9, 7.2, 4.5

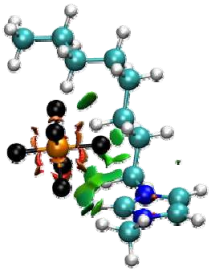

(**g**$_{+}$**F**;g$_{+}$t$_{3}$g$_{+}$t$_{2}$)
7.1, 7.2, 4.5

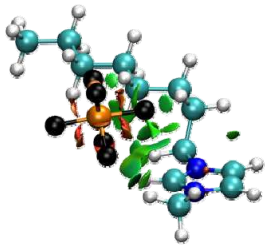

(**g**$_{+}$**F**;g$_{+}$tg$_{+}$t$_{4}$)
7.7, 9.7, 3.6

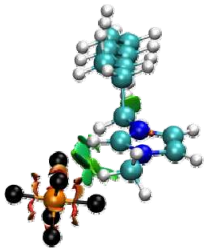

(**g**$_{-}$**F**;g$_{+}$tg$_{-}$t$_{4}$)
8.8, 17.5, –

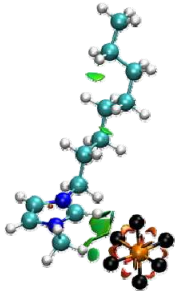

(**cF**;g$_{-}$t$_{2}$g$_{+}$tg$_{+}$t)
9.0, –, –

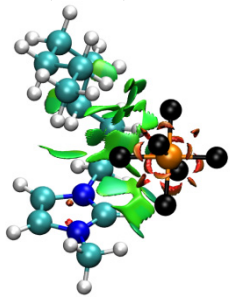

(**g**$_{-}$**F**;g$_{-2}$t$_{2}$g$_{+2}$t)
–, 0.0, 4.6

(C_8mim:PF_6)

Figure S7.

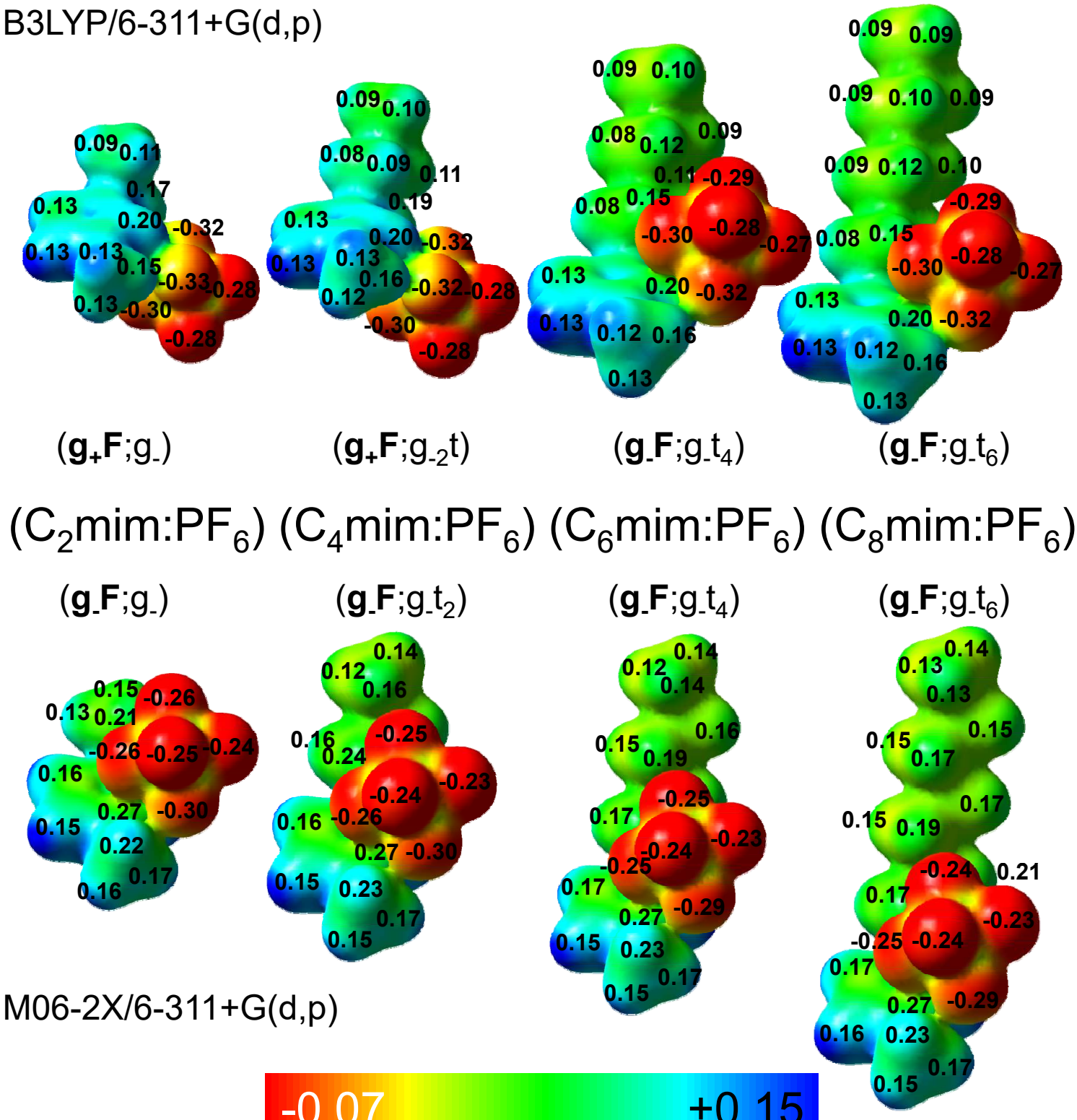
B3LYP/6-311+G(d,p)
(g+F;g-)
(g+F;g-2t)
(g-F;g-t4)
(g-F;g-t6)
(C2mim:PF6)
(C4mim:PF6)
(C6mim:PF6)
(C8mim:PF6)
(g-F;g-)
(g-F;g-t2)
(g-F;g-t4)
(g-F;g-t6)
M06-2X/6-311+G(d,p)
-0.07
+0.15

Figure S8.

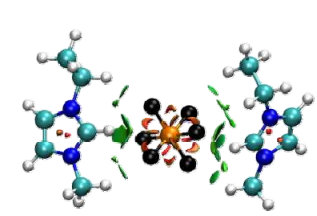

[g$_-$;**ccFcF**;g$_-$]$^+$
0.0, –, –

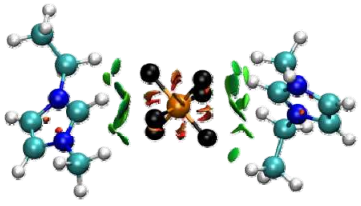

[g$_-$;**g$_-$cFcF**;g$_-$]$^+$
0.1, –, –

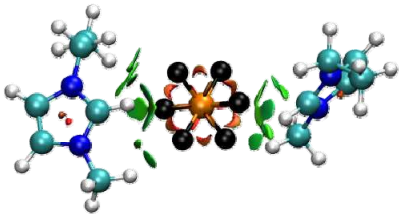

[g$_+$;**g$_+$cFcF**;g$_+$]$^+$
0.2, –, –

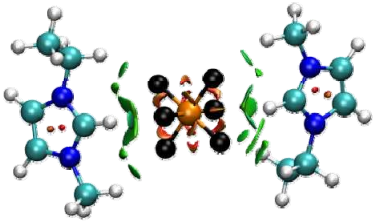

[g$_-$;**tcFcF**;g$_+$]$^+$
0.3, –, –

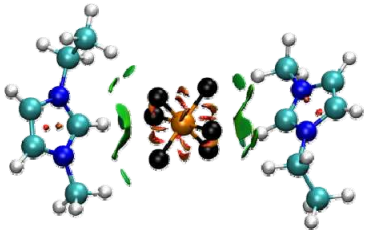

[g$_-$;**tcFcF;**g$_+$]$^+$
1.3, –, –

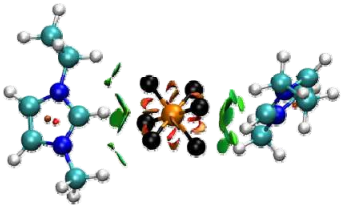

[g$_-$;**g$_+$cFcF**;g$_+$]$^+$
1.4, –, –

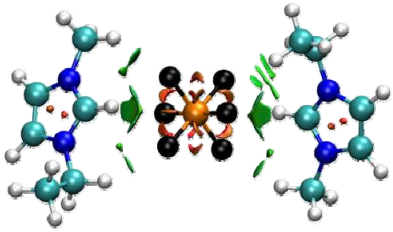

[g$_+$;**tcFcF**;g$_+$]$^+$
1.6, –, –

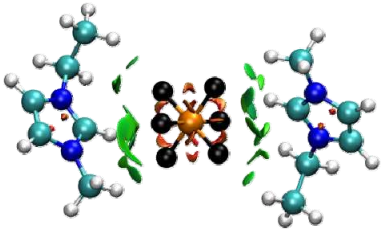

[g$_-$;**g$_-$cFcF**;g$_-$]$^+$
1.6, –, –

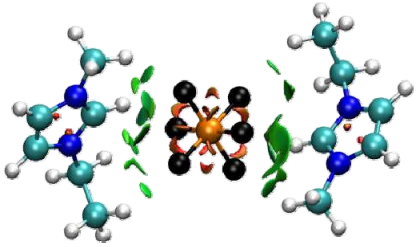

[g$_+$;**g$_+$cFcF**;g$_+$]$^+$
1.6, –, –

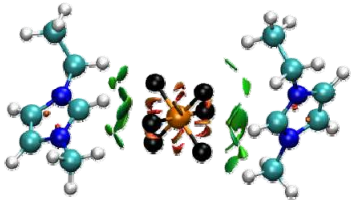

[g$_-$;**g$_+$cFcF**;g$_-$]$^+$
1.7, –, –

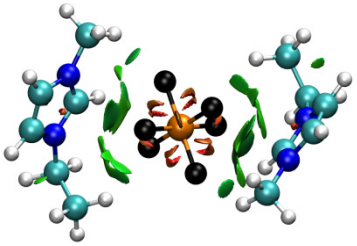

[g$_+$;**g$_+$g$_+$Fg$_+$F**;g$_+$]$^+$
–, 0.0, 2.9

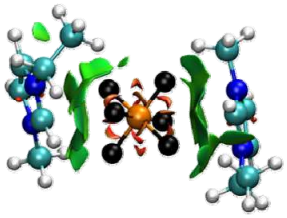

[g$_+$;**g$_+$g$_+$Fg$_+$F**;c]$^+$
–, –, 0.0

[2C$_2$mim:PF$_6$]$^+$

Figure S9.

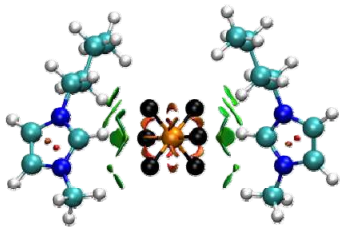

$[g_+t_2;\mathbf{ccFcF};g_+t_2]^+$
0.0, –, –

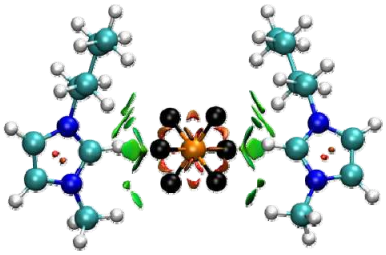

$[g_-t_2;\mathbf{ccFcF};g_-t_2]^+$
0.0, –, –

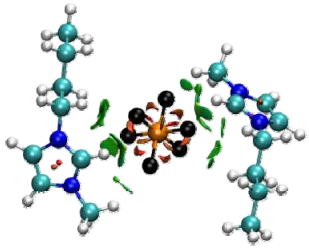

$[g_+t_2;\mathbf{g_+}cFcF;g_+t_2]^+$
0.9, –, –

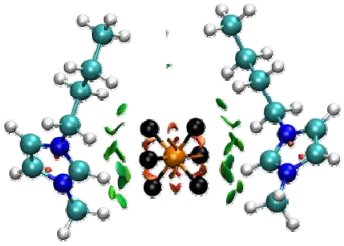

$[g_+t_2;\mathbf{g_-}cFcF;g_+t_2]^+$
1.7, –, –

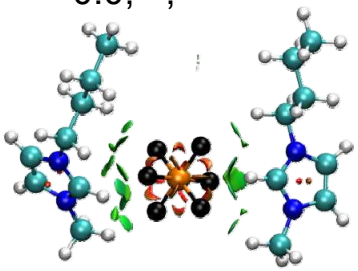

$[g_+t_2;\mathbf{g_-}cFcF;g_+t_2]^+$
2.7, –, –

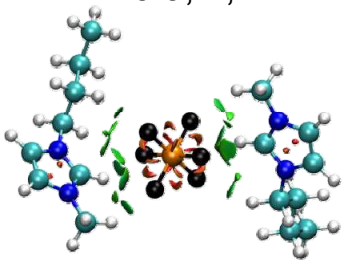

$[g_-t_2;\mathbf{g_-}cFcF;g_+t_2]^+$
3.7, –, –

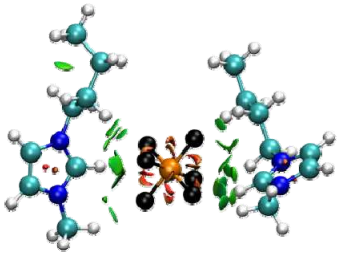

$[g_+t_2;\mathbf{g_-}cFcF;g_-tg_+]^+$
3.8, –, –

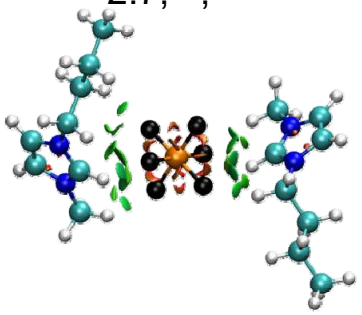

$[g_+t_2;\mathbf{g_+}cFcF;g_+t_2]^+$
4.1, –, –

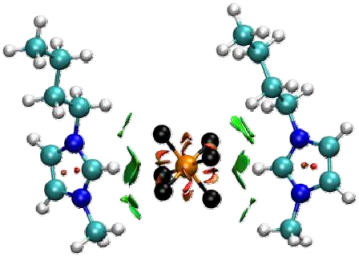

$[g_-t_2;\mathbf{cc}FcF;g_+t_2]^+$
4.8, –, –

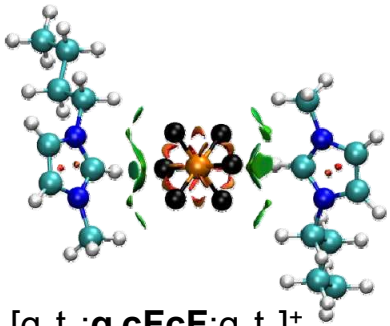

$[g_+t_2;\mathbf{g_-}cFcF;g_+t_2]^+$
5.4, –, –

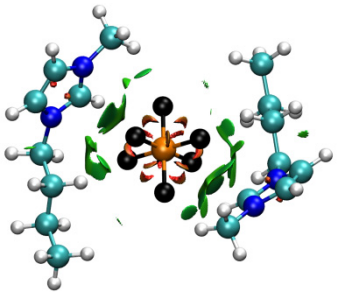

$[g_+t_2;\mathbf{g_+g_+}F\mathbf{g_+}F;g_+t_2]^+$
–, 0.0, 1.7

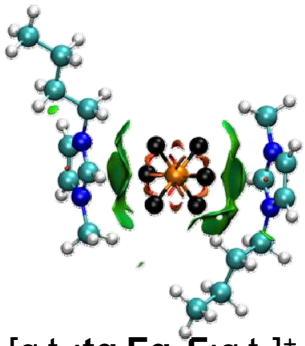

$[g_-t_2;\mathbf{tg_-}F\mathbf{g_+}F;g_-t_2]^+$
–, –, 0.0

$[2C_4mim{:}PF_6]^+$

Figure S10.

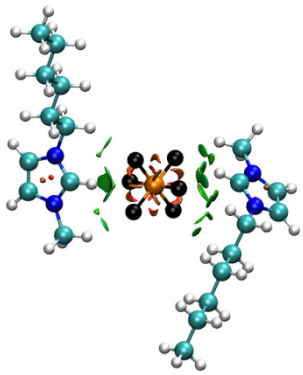

$[g_-t_4;\mathbf{g_+cFcF};g_+t_4]^+$
0.0, –, –

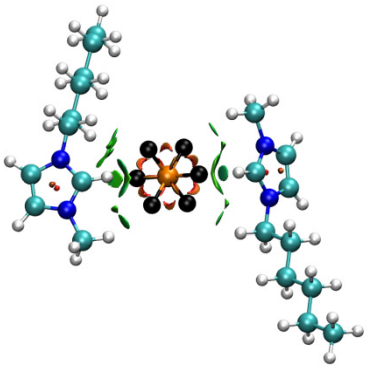

$[g_+t_4;\mathbf{tcFcF};g_-t_4]^+$
0.5, –, –

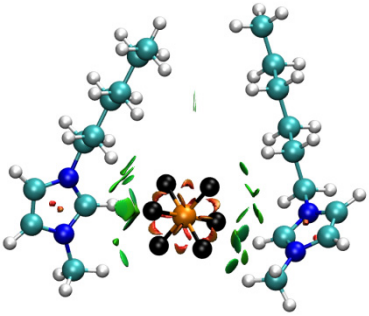

$[g_+t_4;\mathbf{g_-cFcF};g_-t_4]^+$
0.7, –, –

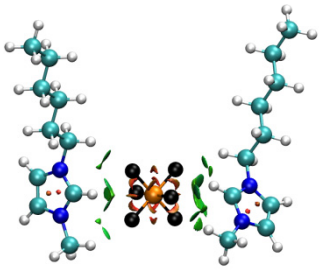

$[g_-t_4;\mathbf{ccFcF};g_+t_4]^+$
0.8, –, –

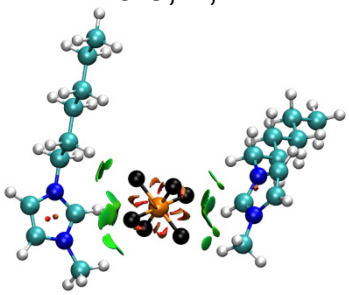

$[g_-t_4;\mathbf{tg_+FcF};g_-t_4]^+$
2.1, –, –

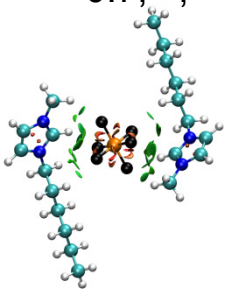

$[g_+t_4;\mathbf{g_+cFcF};g_+t_4]^+$
2.6, –, –

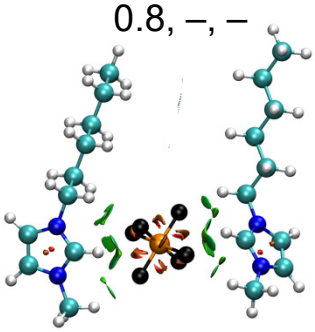

$[g_+t_4;\mathbf{ccFcF};g_+t_4]^+$
2.9, –, –

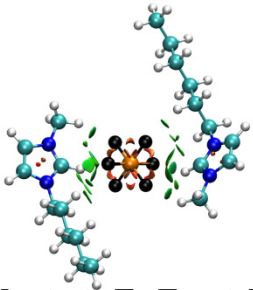

$[g_+t_4;\mathbf{tcFcF};g_+t_4]^+$
4.5, –, –

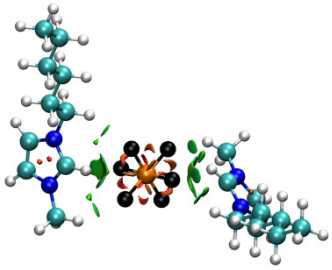

$[g_-t_4;\mathbf{g_+cFcF};g_-t_4]^+$
4.9, –, –

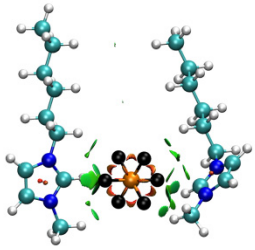

$[g_+t_4;\mathbf{g_-cFg_-F};g_+t_4]^+$
5.3, –, –

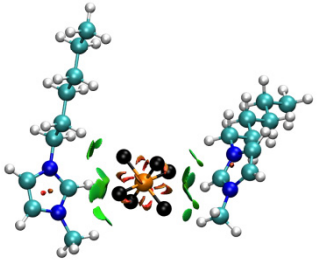

$[g_-t_4;\mathbf{ccFcF};g_-t_4]^+$
7.4, –, –

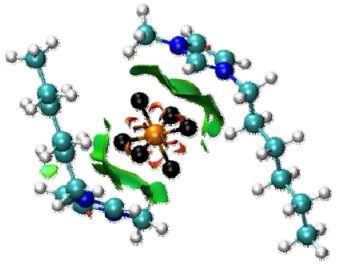

$[g_+t_4;\mathbf{g_+g_+Fg_+F};g_+t_4]^+$
–, 0.0, 0.0

$[2C_6mim{:}PF_6]^+$

Figure S11.

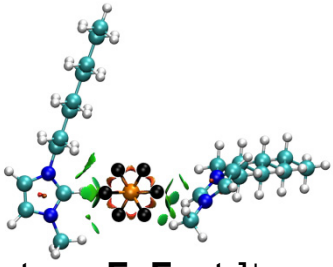

$[g_{-}t_6;\mathbf{g_{-}cFcF};g_{-}t_6]^+$
0.0, –, –

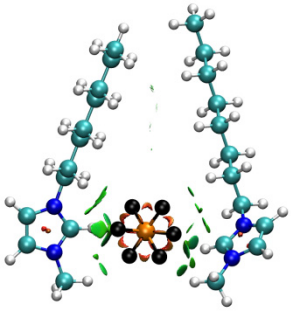

$[g_{+}t_6;\mathbf{g_{-}cFcF};g_{-}t_6]^+$
0.5, –, –

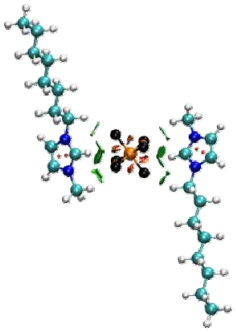

$[g_{-}t_6;\mathbf{tcFcF};g_{+}t_6]^+$
0.8, –, –

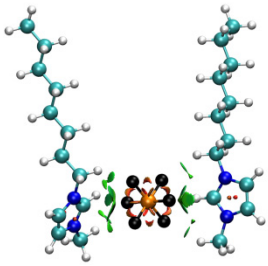

$[g_{-}t_6;\mathbf{ccFcF};g_{+}t_6]^+$
0.8, –, –

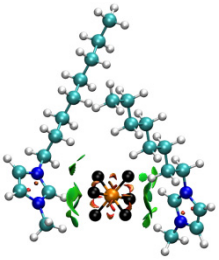

$[g_{+}t_6;\mathbf{g_{+}cFcF};g_{-}t_6]^+$
0.9, –, –

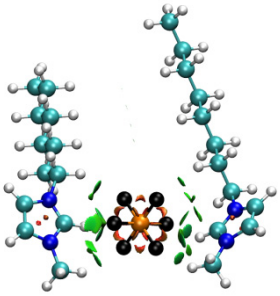

$[g_{+}t_6;\mathbf{ccFcF};g_{+}t_6]^+$
2.5, –, –

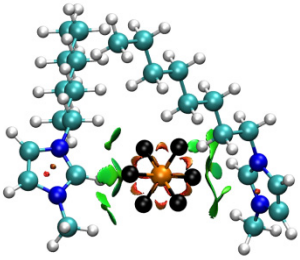

$[g_{+}t_6;\mathbf{g_{+}cFcF};g_{+}t_6]^+$
3.0, –, –

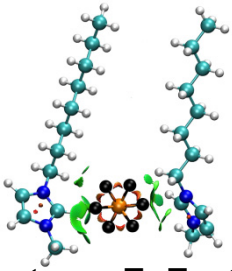

$[g_{-}t_6;\mathbf{g_{+}cFcF};g_{-}t_6]^+$
3.3, –, –

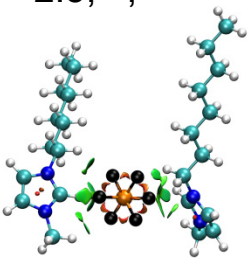

$[g_{-}t_6;\mathbf{g_{+}cFcF};g_{+}t_6]^+$
4.7, –, –

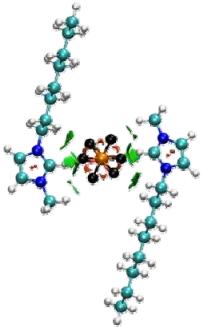

$[g_{+}t_6;\mathbf{tcFcF};g_{-}t_6]^+$
6.3, –, –

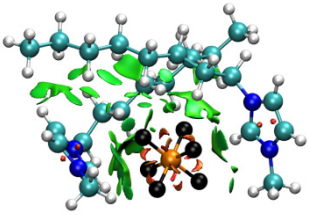

$[g_{+}t_6;\mathbf{g_{+}g_{+}Fg_{-}F};g_{-}t_6]^+$
–, 0.0, 5.1

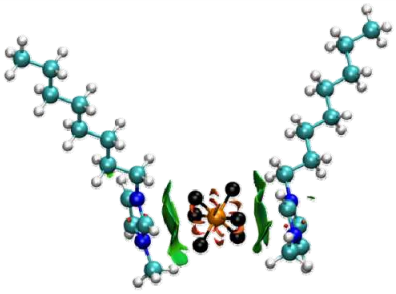

$[g_{-}t_6;\mathbf{g_{-}g_{+}Fg_{-}F};g_{+}t_6]^+$
–, 8.1, 0.0

$[2C_8mim{:}PF_6]^+$

Figure S12.

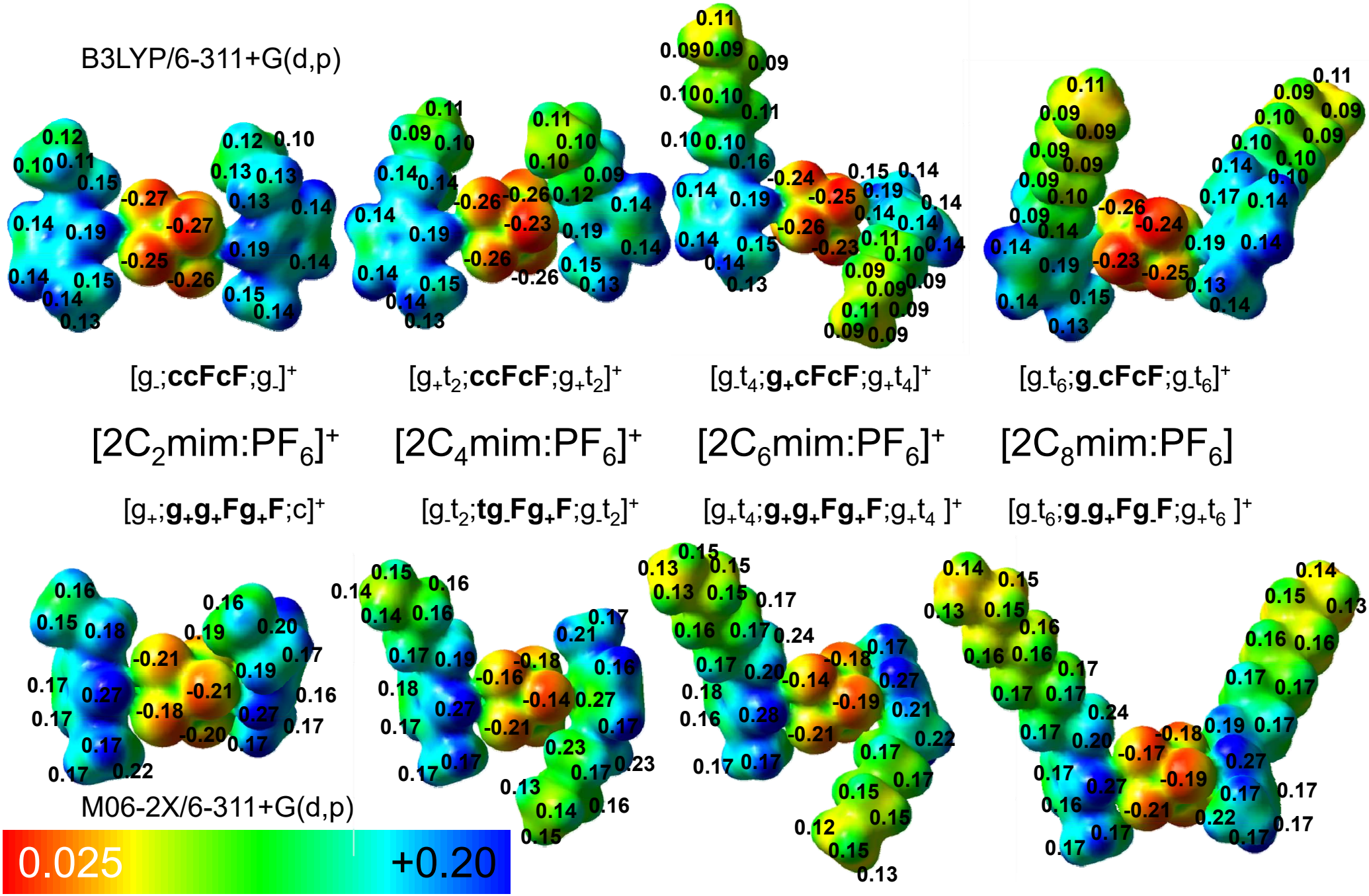
B3LYP/6-311+G(d,p)
[g-;ccFcF;g-]+
[g+t2;ccFcF;g+t2]+
[g-t4;g+cFcF;g+t4]+
[g-t6;g-cFcF;g-t6]+
[2C2mim:PF6]+
[2C4mim:PF6]+
[2C6mim:PF6]+
[2C8mim:PF6]
[g+;g+g+Fg+F;c]+
[g-t2;tg-Fg+F;g-t2]+
[g+t4;g+g+Fg+F;g+t4]+
[g-t6;g-g+Fg-F;g+t6]+
M06-2X/6-311+G(d,p)
0.025
+0.20

Figure S13.

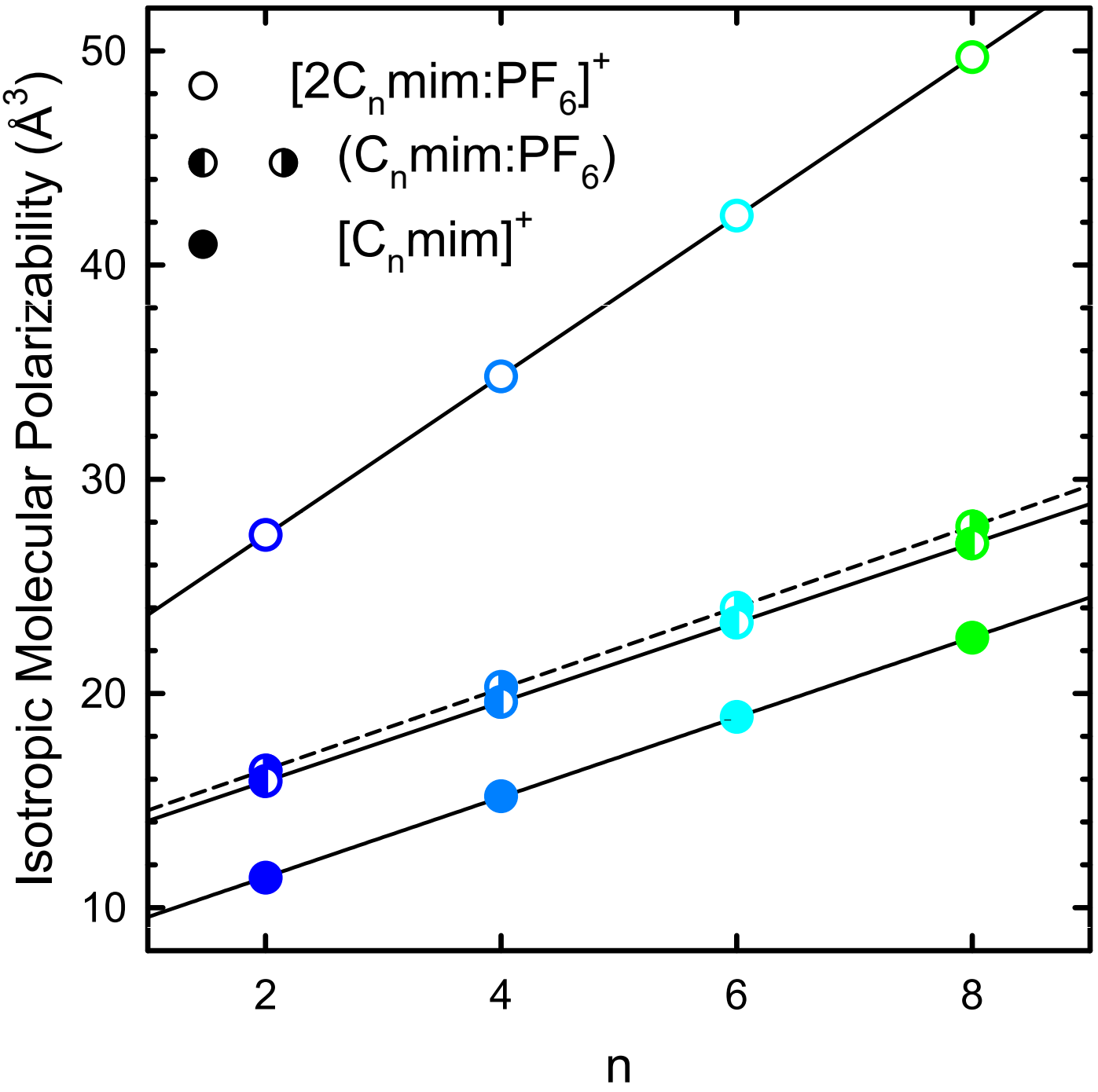
Isotropic Molecular Polarizability (Å^3)
n
[2C$_n$mim:PF$_6$]$^+$
(C$_n$mim:PF$_6$)
[C$_n$mim]$^+$
10
20
30
40
50
2
4
6
8

Figure S14.

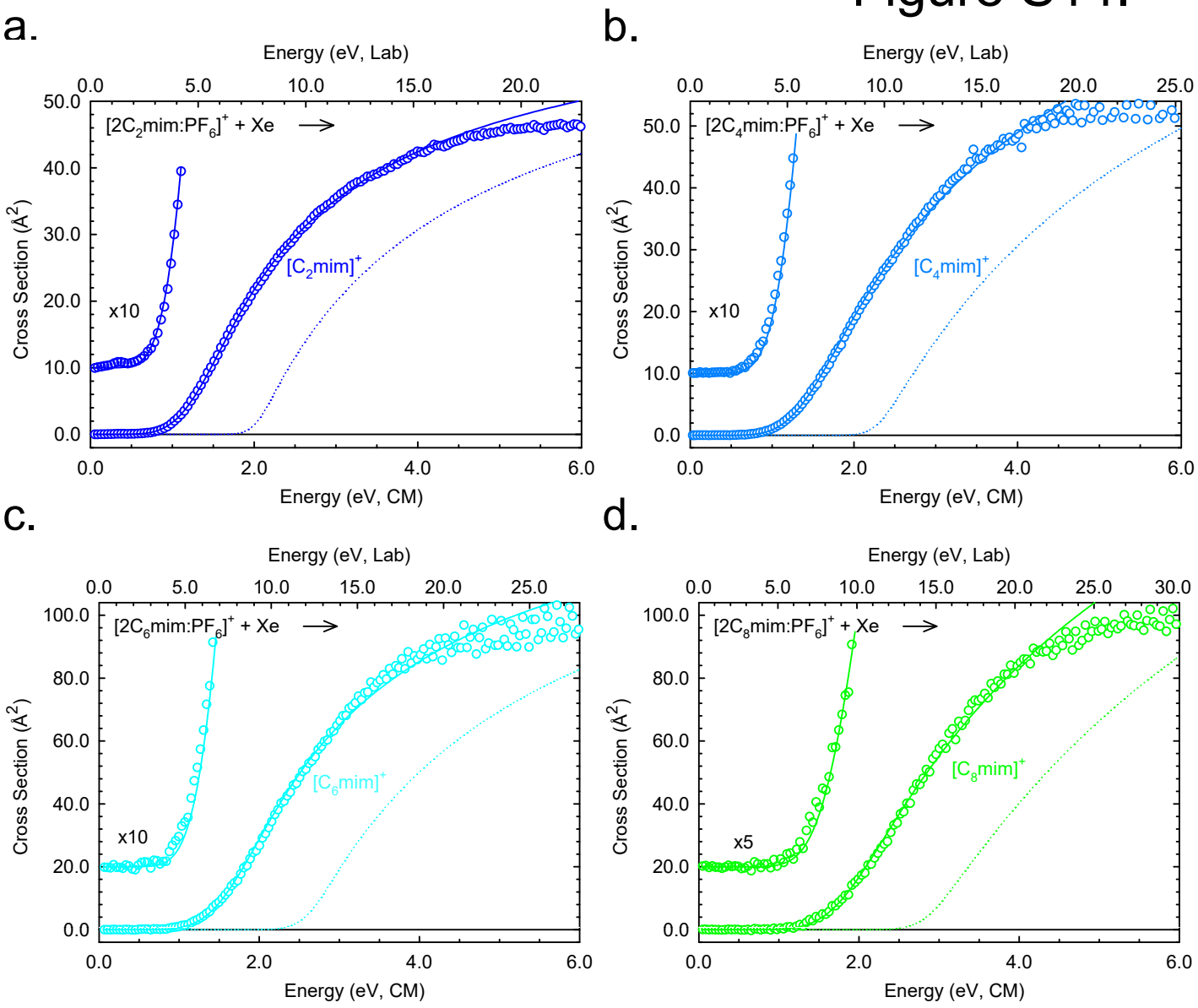
a.
Energy (eV, Lab)
[2C2mim:PF6]+ + Xe
[C2mim]+
x10
Cross Section (Å2)
Energy (eV, CM)
b.
Energy (eV, Lab)
[2C4mim:PF6]+ + Xe
[C4mim]+
x10
Cross Section (Å2)
Energy (eV, CM)
c.
Energy (eV, Lab)
[2C6mim:PF6]+ + Xe
[C6mim]+
x10
Cross Section (Å2)
Energy (eV, CM)
d.
Energy (eV, Lab)
[2C8mim:PF6]+ + Xe
[C8mim]+
x5
Cross Section (Å2)
Energy (eV, CM)

Figure S15.

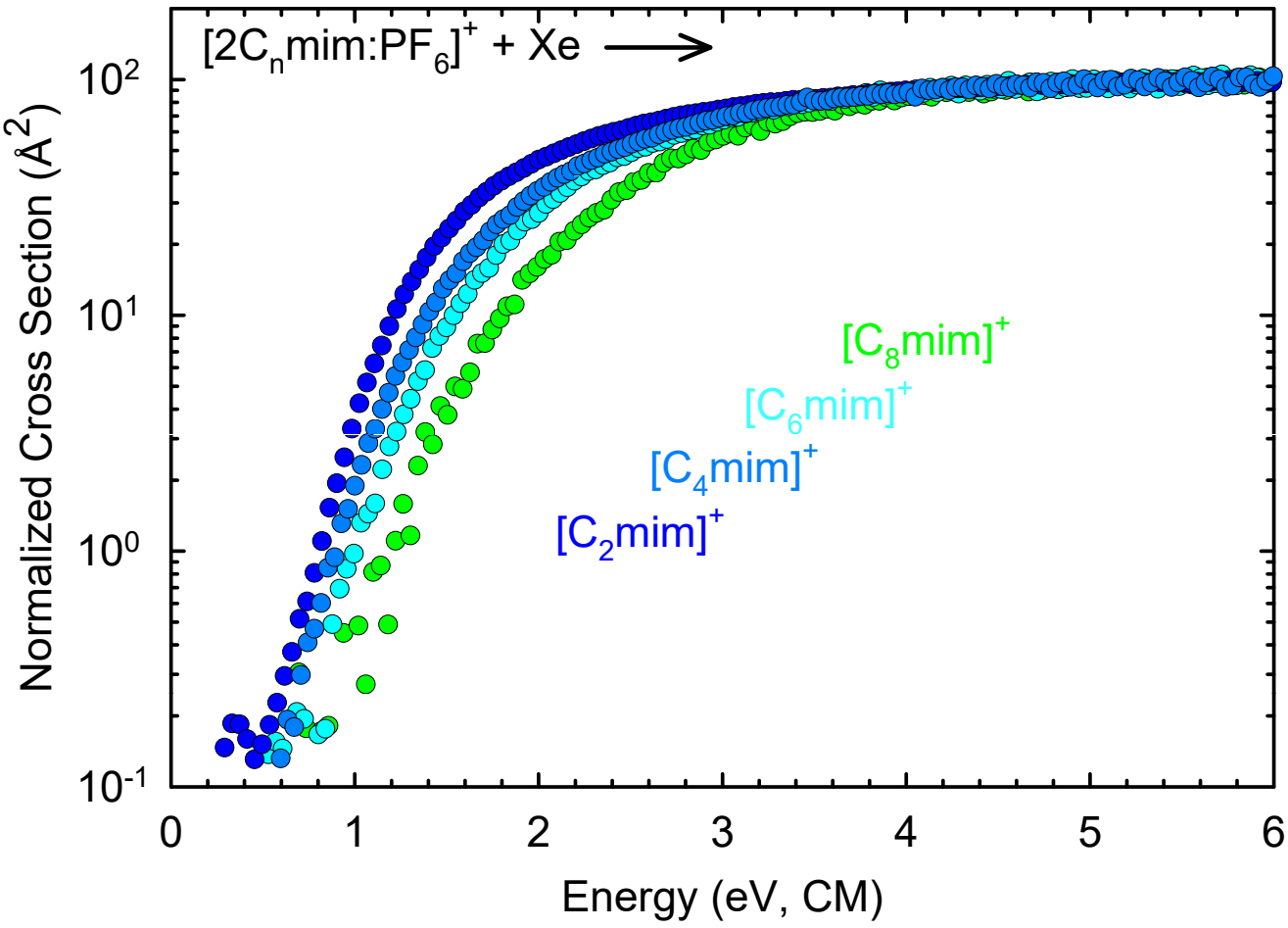
[2C$_n$mim:PF$_6$]$^+$ + Xe
[C$_8$mim]$^+$
[C$_6$mim]$^+$
[C$_4$mim]$^+$
[C$_2$mim]$^+$
Normalized Cross Section (Å^2)
Energy (eV, CM)
10^2
10^1
10^0
10^{-1}
0
1
2
3
4
5
6

Figure S16.

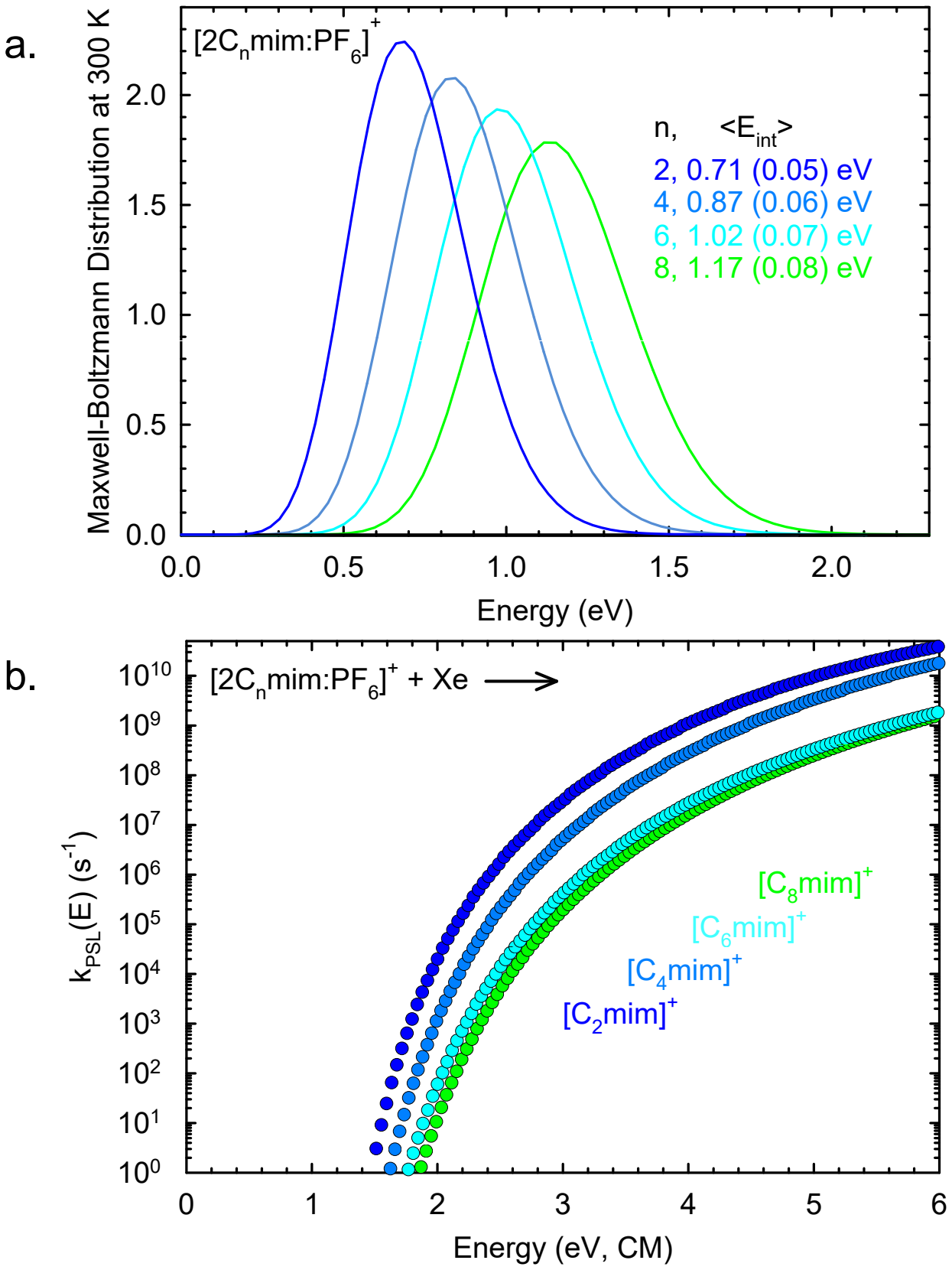
a.
[2C$_n$mim:PF$_6$]$^+$
Maxwell-Boltzmann Distribution at 300 K
Energy (eV)
n, <E$_{int}$>
2, 0.71 (0.05) eV
4, 0.87 (0.06) eV
6, 1.02 (0.07) eV
8, 1.17 (0.08) eV
b.
[2C$_n$mim:PF$_6$]$^+$ + Xe ⟶
k$_{PSL}$(E) (s^{-1})
Energy (eV, CM)
[C$_8$mim]$^+$
[C$_6$mim]$^+$
[C$_4$mim]$^+$
[C$_2$mim]$^+$

Figure S17.

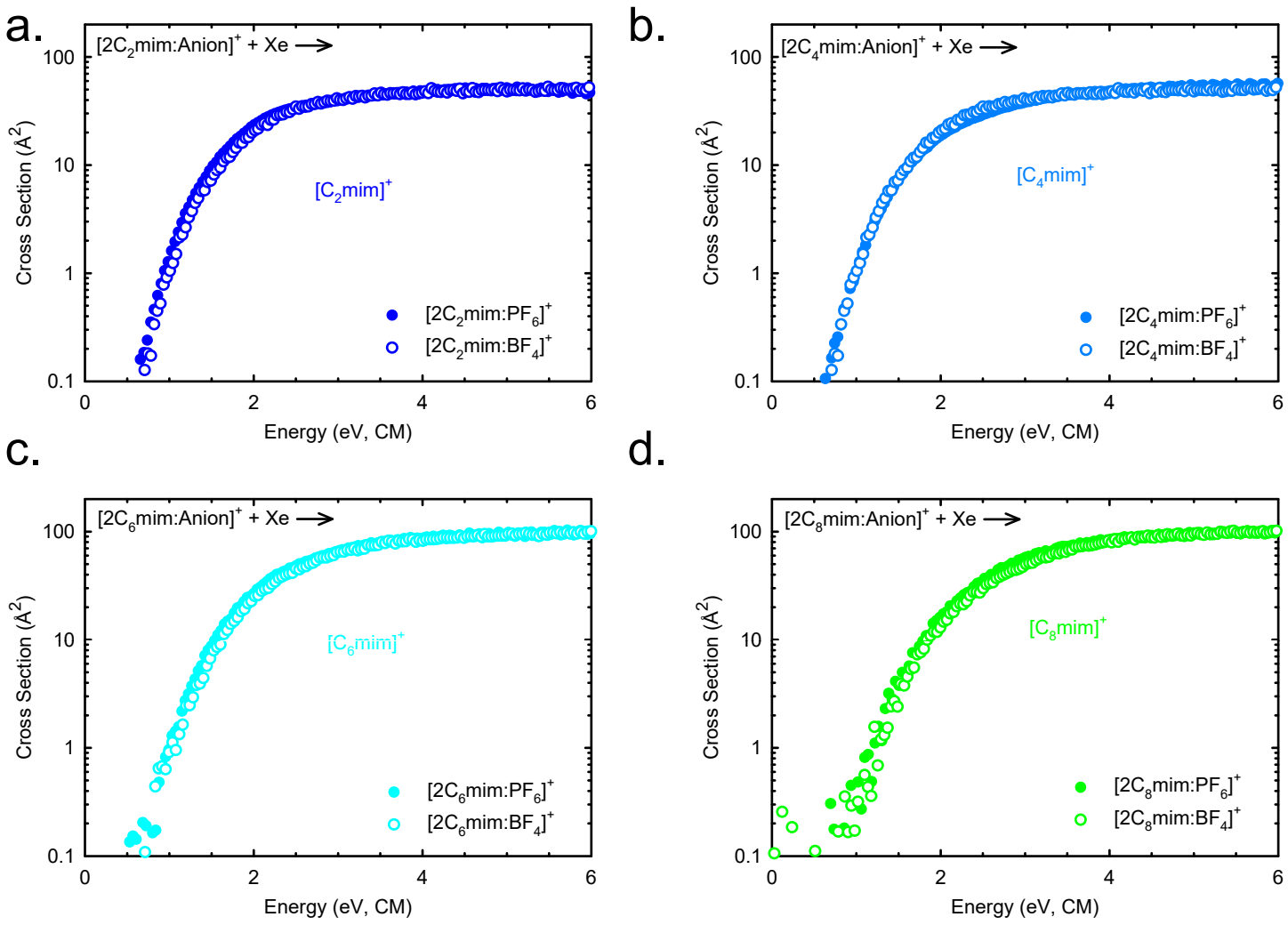
a.
[2C2mim:Anion]+ + Xe ⟶
[C2mim]+
[2C2mim:PF6]+
[2C2mim:BF4]+
b.
[2C4mim:Anion]+ + Xe ⟶
[C4mim]+
[2C4mim:PF6]+
[2C4mim:BF4]+
c.
[2C6mim:Anion]+ + Xe ⟶
[C6mim]+
[2C6mim:PF6]+
[2C6mim:BF4]+
d.
[2C8mim:Anion]+ + Xe ⟶
[C8mim]+
[2C8mim:PF6]+
[2C8mim:BF4]+
Cross Section (Å2)
Energy (eV, CM)
0.1
1
10
100
0
2
4
6